

Magnetic Field Inhomogeneities and Their Influence on Transmission and Background at the KATRIN Main Spectrometer

Zur Erlangung des akademischen Grades eines
DOKTORS DER NATURWISSENSCHAFTEN
von der Fakultät für Physik
des Karlsruher Instituts für Technologie
genehmigte
DISSERTATION
von

Diplom-Physiker Jan Christoph Reich
aus Landau in der Pfalz

Referent: Prof. Dr. G. Drexlin
Institut für Experimentelle Kernphysik, KIT
Korreferent: Prof. Dr. Th. Müller
Institut für Experimentelle Kernphysik, KIT

Tag der mündlichen Prüfung: 11. Januar 2013

Erklärung

Hiermit versichere ich, diese Arbeit selbstständig und nur unter Verwendung der angegebenen Hilfsmittel und Quellen verfasst zu haben.

Jan Reich, Karlsruhe, Dezember 2012

Contents

1	Introduction	1
1.1	Advent of Neutrino Physics	1
1.2	Neutrinos in Particle Physics and Cosmology	2
1.2.1	Neutrinos in the Standard Model	2
1.2.2	Neutrino Influence on Cosmology	3
1.3	Physics of Massive Neutrinos	7
1.3.1	Neutrino Oscillation Experiments	7
1.3.2	Direct Neutrino Mass Experiments	15
2	The KATRIN Experiment	21
2.1	Tritium-Beta-Decay	21
2.2	The KATRIN Measurement Principle	22
2.2.1	MAC-E Filter	22
2.3	An Overview of the KATRIN Experiment	28
2.3.1	Windowless Gaseous Tritium Source	28
2.3.2	Transport Section	30
2.3.3	Electrostatic Spectrometers	31
2.3.4	Focal Plane Detector	35
2.4	Demands on the Magnetic Field in the Main Spectrometer	35
2.4.1	Transmission Properties	36
2.4.2	Background Reduction	36

3	The Air Coil Systems at the KATRIN Main Spectrometer	37
3.1	Motivation of the Air Coil Systems	37
3.2	Electromagnetic Design	39
3.2.1	Low Field Coil System	39
3.2.2	Earth Magnetic Field Compensation System	40
3.3	Technical Realisation	43
3.3.1	Electrical Layout	43
3.3.2	Support Structure	43
3.3.3	Mechanical Layout	44
3.4	Commissioning of the Air Coil Systems	46
3.4.1	Measurements Inside the Main Spectrometer	46
3.4.2	Field Linearity Studies	56
4	Magnetic Field Models for the KATRIN Main Spectrometer	59
4.1	The KASSIOPEIA Simulation Software	59
4.1.1	Aims of KASSIOPEIA	59
4.1.2	Organisation of Monte Carlo Simulations	60
4.1.3	Particle Creation and Tracking	61
4.2	Magnetic Field Calculation Methods	62
4.2.1	Elliptic Integrals	62
4.2.2	Zonal Harmonic Expansion	63
4.2.3	Biot-Savart's Law	67
4.2.4	Magnetic Dipoles	68
4.2.5	3D Hermite Interpolation	70
5	Magnetic Materials in Measurement and Simulation	73
5.1	Experimental Observation	73
5.1.1	Field Survey in the KATRIN Hall	73
5.1.2	Measurements Inside the Main Spectrometer	77
5.1.3	Time Dependency of the Magnetic Material's Field	80
5.2	Representation in Simulations	81
5.2.1	Dipole Distribution Method	82
5.2.2	Fit to Measured Data	83
5.2.3	Results	85
5.3	Summary	91

6	Simulations of Transmission Properties and Background with Realistic Magnetic Fields	93
6.1	Transmission Studies	93
6.1.1	Magnetic Field in the Analyzing Plane	94
6.1.2	Monte-Carlo Particle Tracking Simulations	96
6.2	Background Studies	98
6.2.1	Electron Drift Forces	98
6.2.2	Extent of Electron Drifts in the Simulated Setup	100
6.3	Summary	104
7	Precision Magnetic Monitoring System	107
7.1	Principles of Magnetic Monitoring at the KATRIN Main Spectrometer .	107
7.1.1	MobS System	107
7.1.2	Continuous Monitoring System	109
7.2	Technical Design of the Continuous Monitoring Stations	110
7.2.1	Sensor Station Design	110
7.2.2	Inclinometer Test	110
7.2.3	Orientation and Positioning with a Laser System	111
8	Conclusions	115
A	Components of the Continuous Magnetic Monitoring System	117
A.1	Magnetometer	117
A.2	Inclinometer	119
	Bibliography	121

List of Figures

1.1	Effect of neutrino mass on structure formation	6
1.2	Neutrinos as hot dark matter	7
1.3	Solar neutrino spectrum	9
1.4	Detection of neutrinos via charged and neutral currents	10
1.5	ν B Neutrinos from the sun in SNO	10
1.6	Neutrino mass hierarchy scenarios	15
1.7	Double- β -decay energy states	16
1.8	Neutrinoless double- β -decay	17
1.9	Signature of neutrinoless double- β -decay	17
2.1	Energy spectrum of tritium decay	22
2.2	MAC-E Filter Schematic	23
2.3	Energy analysis by retarding potential	24
2.4	Sensitivity of the KATRIN experiment	28
2.5	Overview of the KATRIN experiment	29
2.6	Windowless Gaseous Tritium Source	29
2.7	Schematic of the DPS2-F	31
2.8	KATRIN pre-spectrometer	32
2.9	The KATRIN main spectrometer	34
2.10	Layout of the KATRIN focal plane detector	35
2.11	Design field strengths in the analysing plane	36
3.1	Magnetic flux tube in the KATRIN spectrometers	38
3.2	Magnetic field configuration with one global minimum	40

3.3	Magnetic field configuration with two local minima	41
3.4	Radial homogeneity of the magnetic field at $z = 0$	41
3.6	Influence of the end parameter on field homogeneity	42
3.5	Schematic of a cosine coil design	42
3.7	Azimuthal field fluctuations of a cosine coil system	43
3.8	Overview of the KATRIN Main spectrometer and the LFCS air coils . .	44
3.9	Comparison of magnetic field inhomogeneities	45
3.10	Holding structure of the magnetometer	47
3.11	Positions of magnetic field measurements in the main spectrometer . . .	47
3.12	Comparison of measured and simulated magnetic LFCS fields in the main spectrometer	50
3.13	Comparison of measured and simulated magnetic EMCS fields in the main spectrometer	51
3.14	Histogram of absolute LFCS field deviations	52
3.15	Histogram of absolute EMCS field deviations	53
3.16	Histogram of angular LFCS field deviations	54
3.17	Histogram of angular EMCS field deviations	55
3.18	LFCS magnetic fields with precise currents	57
3.19	Linearity of the LFCS	58
4.1	Magnetic field created by an electric current loop	62
4.2	Convergence radius of the Central Zonal Harmonic Expansion	64
4.3	Convergence radius of the Remote Zonal Harmonic Expansion	65
4.4	Convergence radii for multiple coils	66
4.5	Convergence radii for multiple coils with additional source points	66
4.6	Source points of coils with different symmetry axes	67
4.7	Integrated Biot-Savart field calculation	68
4.8	Magnetic dipole field calculation model	69
4.9	Cuboid of an interpolation grid	70
5.1	First evidence for a magnetic materials field	74
5.2	Magnetic field survey regions	75

5.3	Holding structure and measurement grid during field surveys	75
5.4	Exemplary regions from the magnetic field survey near the spectrometer hall walls	76
5.5	Field of the magnetic materials in the main spectrometer	78
5.6	Mounting used to measure the magnetic fields around the main spec- trometer	79
5.7	Field of the magnetic materials around the main spectrometer	79
5.8	Magnetic field time development	80
5.9	Magnetic field below the detector platform during a detector magnet system test	81
5.10	Magnetic field below the pre spectrometer platform during and after a DPS2-F magnet test	82
5.11	Variation of dipole geometry	83
5.12	Regions for Dipole placement at the main spectrometer	85
5.13	Field strength agreements for dipole simulations	86
5.14	Angular agreements for dipole simulations	87
5.15	Simultaneous angular and field strength agreements for dipole simulations	87
5.16	Mean ratio dependence of dipole strength fits	88
5.17	Mean angle difference dependence of dipole strength fits	88
5.18	Comparison between measured and simulated field of magnetic materials	89
5.19	Difference vectors between measured and simulated field of magnetic materials	90
5.20	Simulated magnetic materials field in the equatorial plane	90
5.21	Simulated magnetic materials field in the central part of the equatorial plane	91
6.1	Magnetic field on the x-axis in the analyzing plane	94
6.2	Magnetic field changes on the x-axis of the analyzing plane	95
6.3	Magnetic field changes in the analyzing plane	95
6.4	On-axis transmission simulation	97
6.5	Off-axis transmission simulation	98
6.6	Transmission simulations with the magnetic materials setup	99
6.7	Zoom in on the transmission simulations data of the magnetic materials setup	99

6.8	Radial drift velocities	101
6.9	Azimuthal magnetic field components in the analyzing plane	101
6.10	Azimuthal magnetic field gradients in the analyzing plane	102
6.11	Radial and azimuthal drift velocities at $z = 0$	103
6.12	Ratio of radial to azimuthal drift velocity	104
6.13	Radial and azimuthal drift velocities at $z = 4$ m	105
6.14	Ratio of radial to azimuthal drift velocity at $z = 4$ m	105
7.1	Mobile sensor unit	108
7.2	Positions of magnetic monitoring stations around the main spectrometer	109
7.3	Prototype of the continuous magnetic field monitoring stations	111
7.4	Setup of inclinometer test measurements	112
7.5	Data of inclinometer test	112
7.6	Angular sensitivity of the laser calibration setup	114
A.1	Sketch of a fluxgate magnetometer	118
A.2	Technical drawing of the Bartington Mas-03MS sensor	118
A.3	Working principle of the inclinometers	120

1. Introduction

1.1 Advent of Neutrino Physics

Of all radioactive decays known at the beginning of the 20th century, beta decay continued to puzzle physicists with various questions. Unlike alpha and gamma decays, this process results in a continuous energy spectrum of its emitted particle. From the observed reaction



a discrete energy spectrum was expected with the electron having an energy equivalent to the mass difference between neutron and proton. Since the electron was emitted with less energy, this meant that energy was not conserved in this process. Angular momentum was also violated, since one spin $1/2$ particle decayed into two spin $1/2$ particles. This apparent conflict began to clear when Wolfgang Pauli postulated the existence of a third, invisible decay product in 1930, which he called "neutron" [1]. This particle had to be electrically neutral, to remain undetected. Furthermore it would have to be of spin $1/2$ and have a small mass compared to the electron. 4 years later in 1934, Enrico Fermi formulated his consistent theory of beta decay [2]. He named this particle "neutrino", "small neutron", since the name neutron had in the meantime been given to the electrically neutral nucleon [3]. With this description it was possible to account for energy conservation as well as angular momentum conservation in the decay



This picture easily explains the observed continuous electron energy spectra since a part of the total decay energy is carried away by the undetected neutrino. Angular momentum conservation was also saved, since the neutrino could be emitted with spin opposite to the electron-spin (Fermi-transition) or opposite to the proton-spin (Gamow-Teller-transition). Those spins would cancel out and leave the third decay product to carry the spin of the original particle.

The validation of this theory had to wait another 22 years until 1956, when Clyde Cowan and Fred Reines made a successful direct observation of neutrinos [4]. Dropping plans to use a thermonuclear explosion as a neutrino source they settled for the weaker but

less-destructive Savannah river reactor as a powerful and continuous neutrino source. The detected reaction was an induced inverse beta decay of protons in a water target:

$$\bar{\nu}_e + p \rightarrow e^+ + n \quad (1.3)$$

Further experiments resulted 1962 in the observation that neutrinos produced by pion decay produced only muons in secondary reactions [5]. This established the existence of two distinct neutrino species, as hypothesized by Pontecorvo in 1960 [6]. Later, the measurement of the invisible decay width of the Z^0 Boson at LEP yielded the number of light neutrino species as $N = 3.00 \pm 0.08$ [7]. So today, three neutrino flavours, ν_e , ν_μ and ν_τ are established since in 2000 the DONUT collaboration announced the first direct observation of a ν_τ [8].

The standard model of particle physics includes these three neutrino species as well as their antiparticles. While the standard model treats them as massless, since 1998 the observations of neutrino oscillations e.g. at the Super-Kamiokande experiment [9] point towards massive neutrinos. This is a first clear indication of physics beyond the standard model.

The standard model as well as the LEP result mentioned above only include light neutrinos. It is possible for additional sterile neutrinos to exist [10]. These would not interact and only mix with the first three states, thus the term sterile. If those existed, they might provide Cosmology with a suitable candidate for dark matter particles. Cosmology also gives limits on the mass of the light neutrino flavours from structure formation analyses, see section 1.2.2 for details.

Direct neutrino mass measurements were only able to set upper limits on this mass so far. The most stringent upper limit today is $m_{\nu_e} = 2.2 \text{ eV}/c^2$ [11] provided by the Mainz [12] and Troitsk [13] neutrino mass experiments. In 2011, the Troitsk collaboration published a re-analysis with an upper limit of $m_{\nu_e} < 2.05 \text{ eV}/c^2$ 95 %C.L. [14]. The **K**arlsruhe **T**ritium **N**eutrino experiment with its design sensitivity of $0.2 \text{ eV}/c^2$ (90% C.L.) has a 5σ discovery potential for an electron anti-neutrino rest mass of $0.35 \text{ eV}/c^2$ [15].

1.2 Neutrinos in Particle Physics and Cosmology

The standard model of particle physics has a working description of neutrinos and their interactions with other particles discussed in 1.2.1. Whereas cosmology includes the influence of neutrinos in the formation of light elements shortly after the big bang and as a contributing mass factor in the structure formation of the universe which will be addressed in 1.2.2.

1.2.1 Neutrinos in the Standard Model

The standard model of particle physics describes the elementary particles and their interactions. There are six quarks arrayed in 3 generations (u, d, c, s, t, b). These carry a strong interaction colour charge and an electrical charge of $+2/3$ (u, c, t) or $-1/3$

(d, s, b). Then there are 6 leptons (e, μ, τ and ν_e, ν_μ, ν_τ) also in 3 generations paired as follows: $(\nu_e, e), (\nu_\mu, \mu), (\nu_\tau, \tau)$. Leptons carry a weak interaction charge, but only the top tier (e, μ, τ) carry an electrical charge of $-1 e$, while the neutrinos are electrically neutral. All quarks and leptons have spin $1/2$ and are thus fermions. In addition to these fermions, which constitute the known particles, there are the interaction bosons. Gluons mediate the strong interaction between quarks, photons, the W^\pm and Z^0 bosons mediate the electroweak interaction. The recently at LHC discovered Higgs boson gives the quarks and leptons their mass. Neutrinos however are massless in the standard model.

Generation	1	2	3
Quarks	$\begin{pmatrix} u \\ d \end{pmatrix}$	$\begin{pmatrix} c \\ s \end{pmatrix}$	$\begin{pmatrix} t \\ b \end{pmatrix}$
Leptons	$\begin{pmatrix} e \\ \nu_e \end{pmatrix}$	$\begin{pmatrix} \mu \\ \nu_\mu \end{pmatrix}$	$\begin{pmatrix} \tau \\ \nu_\tau \end{pmatrix}$

Table 1.1: Standard model fermions

While the standard model works very well for particle physics, it leaves some open questions. The most prominent perhaps is the lack of a description of gravity, but other recent discoveries are not explained as well. For example, the standard higgs-mechanism does not give mass to neutrinos, so the standard model treats those as massless particles as opposed to observations of neutrino oscillations. Those require the mass eigenstates of neutrinos to be nonzero. For more information on neutrino oscillations see below in 1.3.1. For now it should be noted that the phenomenon of massive neutrinos is a first evidence for physics beyond the standard model.

1.2.2 Neutrino Influence on Cosmology

In cosmology, neutrinos play an important role for example in primordial nucleosynthesis, but also in the matter-antimatter asymmetry of the universe [16] as well as the possible existence of heavy neutrinos which are candidates for dark matter constituents [17]. Furthermore, cosmology can place bounds on the neutrino mass from the primordial neutrino density and structure formation in the universe.

Hard Upper Limit From Neutrino Density

In analogy to the Gerstein-Zeldovich limit [18] for the mass of ν_μ an absolute upper bound on the sum of the mass of all three neutrino flavours can be derived. Let us consider the very early state of the universe with protons and neutrons in thermal equilibrium. For elements heavier than hydrogen to form, this equilibrium needs to be broken. This becomes apparent when looking at the number ratio between protons and neutrons in thermal equilibrium as given by the Boltzmann-factor:

$$\frac{n_n}{n_p} = e^{-\frac{\Delta mc^2}{kT}} \quad (1.4)$$

where $\Delta m = m_n - m_p = 1.3$ MeV is the mass difference of neutron and proton. The formation of light elements is only possible, if the universe has cooled down to a sufficiently low temperature to allow the formation of deuterium. This point is reached when the number of photons with a thermal energy high enough to destroy deuterium via the photodissoziation process

$$D + \gamma = n + p \quad (1.5)$$

is negligible. Now if neutrons and protons were still in thermal equilibrium, the number of neutrons would be much too low to form considerable amounts of deuterium. Whereas the breaking of the thermal equilibrium means that the number of neutrons is only determined by their decay with a half-life of minutes. This allows the universe to cool down to temperatures that allow primordial nucleosynthesis to begin.

The breaking of the equilibrium (1.4) happens, when the expansion rate H of the universe becomes lower than the interaction rate Γ . Since the n-p equilibrium is maintained by neutrino reactions, this marks the time of the freeze out of neutrinos. The weak interaction rate drops steeply with the Temperature ($\Gamma \propto T^5$), this mechanism is very sensitive to the freezeout temperature.

At the time of freeze out the number density of one type of neutrinos is given by

$$\frac{n_{\nu i}}{n_\gamma} = \frac{\bar{n}_{\nu i}}{n_\gamma} = \frac{3}{8} \quad (1.6)$$

after the annihilation of positrons and electrons, the additionally created photons change this to

$$\frac{n_{\nu i} + \bar{n}_{\nu i}}{n_\gamma} = \frac{3}{11} \quad (1.7)$$

Today, the number density of photons in the universe is $n_\gamma = \frac{410.4}{\text{cm}^3}$ [19], and (1.7) gives the number density of neutrinos as $n_\nu = \frac{112}{\text{cm}^3}$ per flavour.

The hardest upper bound on the neutrino mass can now be derived with the assumption that the matter density of the universe is entirely composed of neutrinos and furthermore that the universe is flat, which means its density is the critical density

$$\Omega_\nu = \frac{\rho_\nu}{\rho_c} \leq 1 \quad (1.8)$$

This gives an upper bound on the sum of neutrino masses

$$\sum m_{\nu i} < 94 \text{ eV}/c^2 \Omega h^2. \quad (1.9)$$

With a hubble-parameter of $h = 0.7$ and the matter density fraction $\Omega_{\text{matter}} < 0.3$ this states that the mass of all neutrino flavours combined has to be lower than $14 \text{ eV}/c^2$ [20].

Further Bounds From Primordial Nucleosynthesis

More sophisticated approaches allow for a number of other parameters to be deduced. The number of relativistic particle species at the time of primordial nucleosynthesis heavily influences the abundance of light elements [21]. First, the neutron to proton ratio depends on the number of particle species g_* . As mentioned above, this ratio is critical for the abundance of deuterium which is needed to produce other elements. Secondly, although the freeze out temperature does not depend on g_* , the time at which this temperature is reached does. These two effects influence the number of surviving neutrons.

Structure Formation and Neutrino Mass

The formation of structures in the universe like galaxies and galaxy clusters results from the contraction of matter in denser regions. The density profile is fundamentally influenced by dark matter, since it is only subject to gravity and therefore dark matter is not kept from collapsing by radiation pressure unlike baryonic matter. Hot dark matter e.g. in the form of relativistic neutrinos, on the opposite is able to leave these overly dense regions of space, since they also do interact only weakly with the denser matter. This smears out small scale structures, since these neutrinos have mass and when they leave these regions, the density there decreases. This is especially efficient for small scales, since the hot dark matter remains longer in larger structures due to the sheer amount of time it takes them to traverse these large distances. Figure 1.1 visualizes this effect nicely with simulations of structure formation under the influence of different neutrino masses.

This being said, hot dark matter nivellates density structures to a degree and opposes structure formation. This effect is a direct result of its mass and thus observing structures in the universe constrains the neutrino mass[22].

The actual structure distribution in the universe can be measured experimentally by large scale galaxy surveys, like the Sloan Digital Sky Survey SDSS [25] or the 2dF Galaxy Redshift Survey [26]. Since the smearing effect of neutrinos is strongest in small structures, therefore in the density fluctuation power spectrum $P(k)$ it is most prominent at large wavenumbers k . Figure 1.2 shows such a power spectrum obtained from the SDSS as well as the influence of a nonzero neutrino mass on the formation of small structures.

There is an abundance of these kinds of analyses, since only in conjunction with additional data, as well as other parameters, can a contribution of hot dark matter to the total matter density Ω_{tot} be discerned. For example a combination of SDSS and WMAP data gives an upper limit for the neutrino mass of [27]

$$\sum_i m_\nu < 1.7 \text{ eV}/c^2 \text{ (95 \% C.L.)} \quad (1.10)$$

But these cosmological limits are a bit uncomfortable, since all cosmological models contain a large variety of parameters. Some of these are degenerate, i.e. they produce a

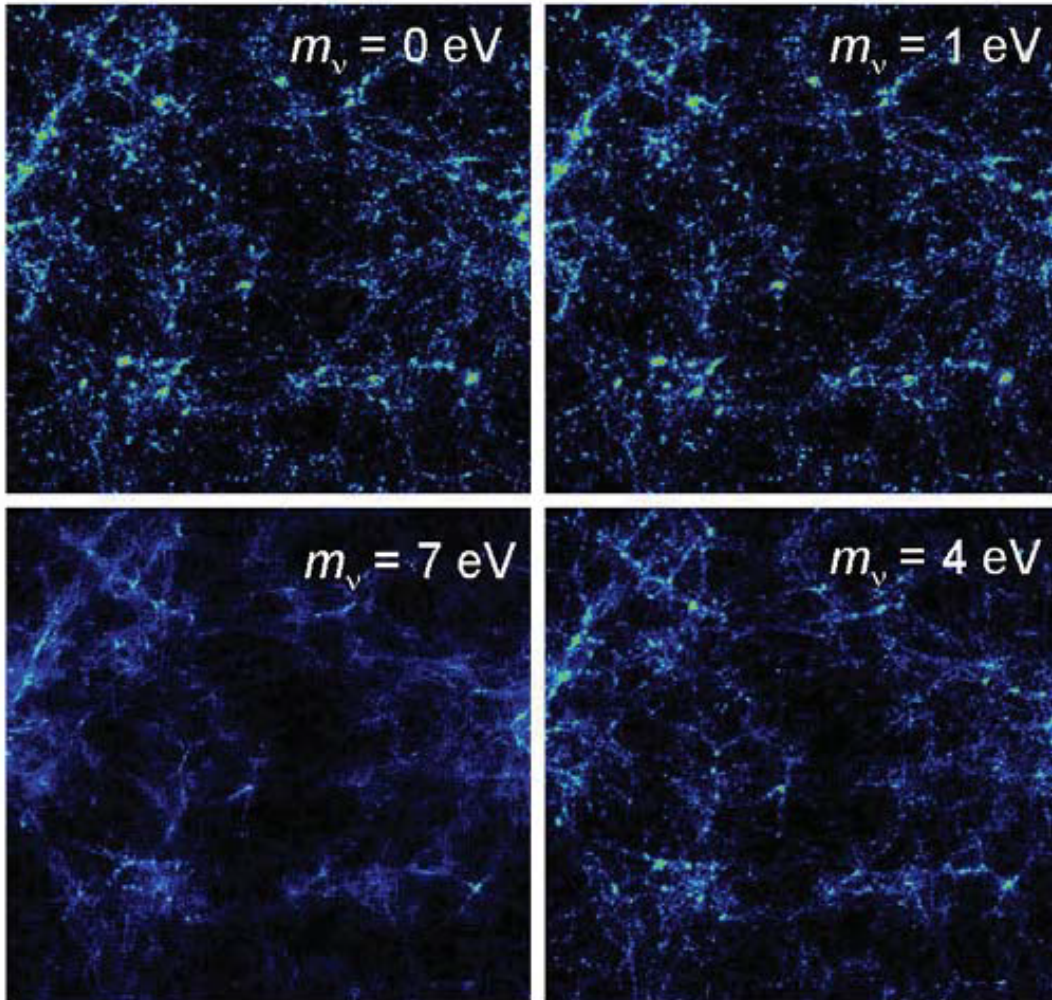


Figure 1.1: Effect of neutrino mass on structure formation in the universe. The figures show simulations of structures evolved from small density fluctuations influenced by hot dark matter neutrinos with different masses. The larger neutrino masses smear out small structures, while leaving large structures mostly untouched.

similar effect as hot dark matter neutrinos. For example dark energy w could also smear out small structures and it is not easily understandable, which part of the smearing comes from neutrinos and which from dark energy.

All in all, cosmological limits are more stringent than the direct mass measurements today, but it has to be noted that these limits are strongly model dependent and neutrino mass predictions vary strongly from model to model. So cosmology makes a valuable contribution to the search for the neutrino mass, but cannot substitute a direct laboratory measurement.

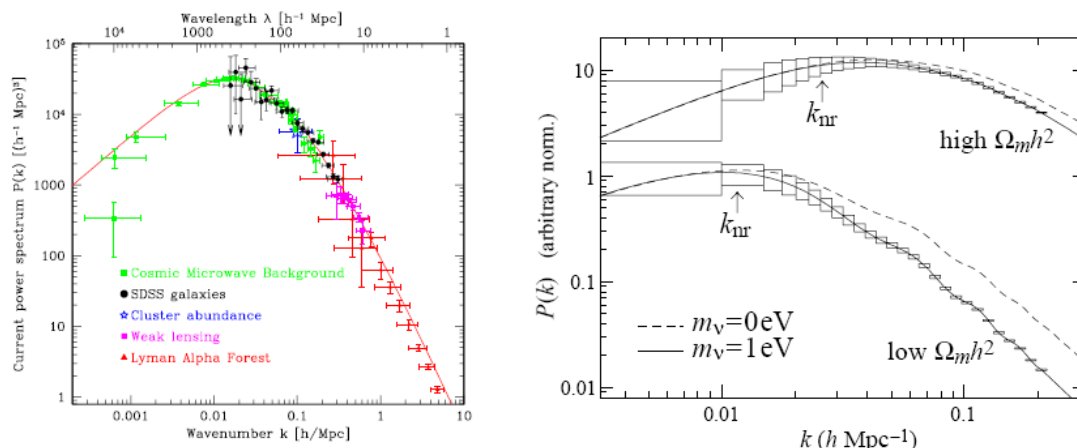


Figure 1.2: **left:** Power spectrum of density fluctuations in the universe [23]. **Right:** Influence of neutrino mass at small scales [24]. Massive neutrinos smear out small structures with wavenumbers $k > 0.01 \text{ h} \cdot \text{Mpc}^{-1}$

1.3 Physics of Massive Neutrinos

The definite discovery that neutrinos are in fact not massless, came from oscillation experiments. Neutrino oscillation means the fact that neutrinos can be detected in another flavour than they were created in. The probability for this is periodic in the propagation distance, therefore oscillations. This phenomenon requires the mass eigenstates of neutrinos to be different from their flavour eigenstates, and therefore nonzero. Details will be given below in 1.3.1. Determining the oscillation parameters allows measuring the squared mass differences between two of these mass eigenstates, but cannot fix the absolute mass scale. This also means that the mass hierarchy is not fixed.

In order to directly measure neutrino masses it is necessary to go beyond oscillation experiments. Double beta decay opens a window to the neutrino mass if it can be observed without emitted neutrinos. This neutrinoless double beta decay requires neutrinos to be their own antiparticles, and the frequency with which it occurs is dependent on the neutrino mass. A model independent method of measuring neutrino masses is offered by beta-decay spectrum measurements. Due to kinematic reasons, a neutrino mass deforms the energy spectrum of the emitted electrons. This effect is only visible near the endpoint of the spectrum. Since only few electrons fall into this energy region, observation of this effect is a nontrivial challenge.

1.3.1 Neutrino Oscillation Experiments

The solar neutrino deficit

Neutrino oscillations are how the neutrino mass game started. The observation of the solar neutrino deficit raised questions about our understanding of neutrino physics.

A large number of neutrinos are created in the nuclear fusion processes in the solar core. Since they only interact weakly they leave the sun undisturbed. The number of

neutrinos reaching the surface of the earth per square meter can be roughly estimated through the solar power output

$$E_{\odot} = 1369 \frac{\text{W}}{\text{m}^2} \quad (1.11)$$

Integrated over the surface of a sphere with radius $r = 1 \text{ AE}$ gives the total solar output. The main energy releasing process in the sun is the fusion of hydrogen into helium



each releasing $\sim 26 \text{ MeV}$. Consequently, the total solar neutrino flux from the sun at earth Φ_{\odot} equates to

$$\Phi_{\odot} = 6.6 \cdot 10^{10} \frac{1}{\text{cm}^2 \text{ s}} \quad (1.13)$$

To refine this rough estimate additional processes have to be considered. Among 1.12 different pp-fusion chains and the CNO-cycle also produce neutrinos. A detailed analysis of these processes gives a complete spectrum of neutrinos originating from the sun as shown in figure 1.3 [28].

The first measurement of the solar neutrino flux was done with the homestake experiment by Ray Davis. It employed a radiochemical technique for detecting neutrinos. In a large tank filled with 600 t of perchlorethylene containing ${}_{37}\text{Cl}$, the induced beta decay



was utilized for indirect neutrino detection. After each measurement period of several weeks, the Argon atoms were chemically separated from the detector liquid. Their decay into ${}_{37}\text{Cl}$ produced an excited state which goes into its ground state via the emission of an Auger electron. This electron can then be detected and the number of events allows to determine how much ${}_{37}\text{Ar}$ was produced during the measurement period. Since the solar neutrino flux is so accurately predictable, it came as a big surprise when Ray Davis measured only $(34 \pm 6) \%$ of the predicted events for neutrino energies $E_{\nu} > 0.7 \text{ MeV}$.

Later, other experiments like Gallex/GNO [29], SAGE [30] and Kamiokande [31], using different targets and detection techniques, also measured significantly lower fluxes than expected and confirmed the solar neutrino deficit established by the Homestake experiment. This posed a massive problem to solar neutrino physics. Either the solar models were incorrect, or the neutrinos somehow disappeared on their way to earth. As it turned out the solar models at the time were fairly accurate and the second case was in fact true. All the experiments conducted could only detect electron neutrinos in the charged current channel and were effectively blind to μ - and τ -neutrinos as they were insensitive to neutral current interactions. A solution to the solar neutrino deficit

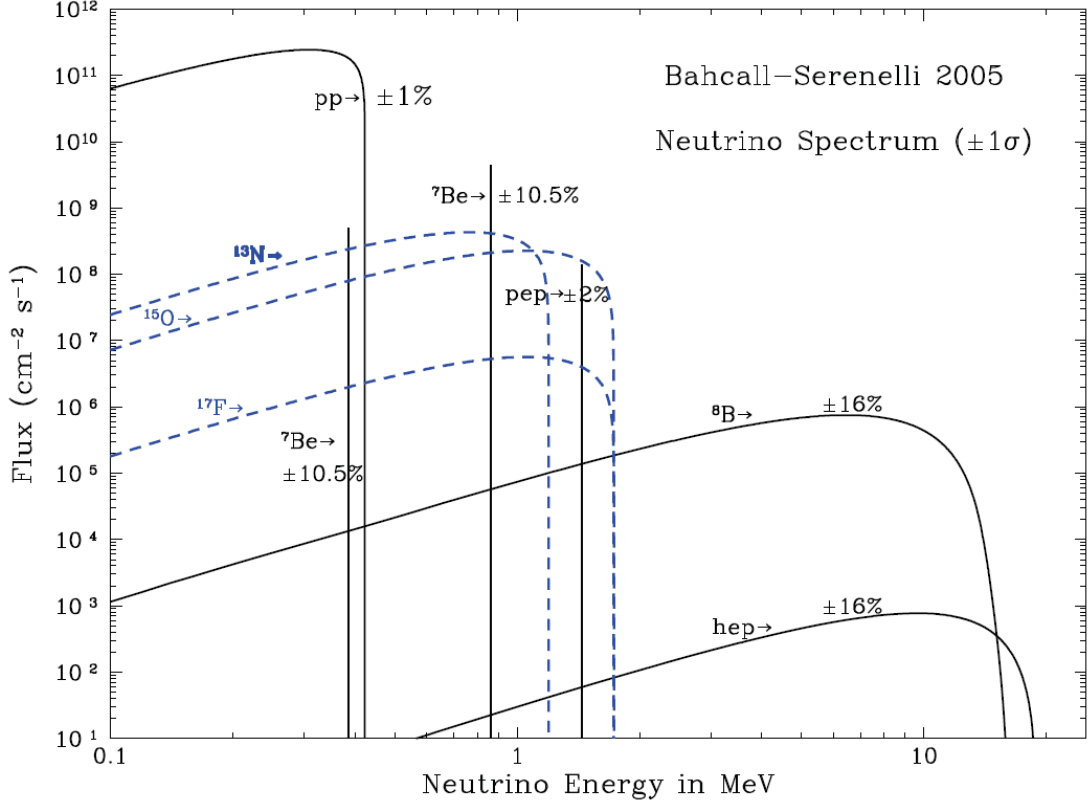
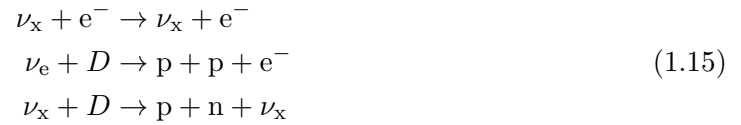


Figure 1.3: The neutrino flux of different processes in the sun as a function of neutrino energy. This is an important information for determining the expected number of neutrino detections since detectors have varying energy thresholds.

was offered by the Sudbury Neutrino Observatory (SNO) in 2001. It was designed to be sensitive to all neutrino flavours. Contrary to previous experiments it could not only detect electron neutrinos which interact via charged currents, this means $\nu_e - e$ scattering. SNO was also sensitive to neutral currents and was able to detect also μ - and τ -neutrinos via the dissociation of deuterium. [32]. Both detection principles are illustrated in figure 1.4. The reactions under consideration are



The experiment was conducted in three phases. In the first phase the detector vessel was filled with 1000 t of pure heavy water. In phase two NaCl salt was added as a medium to enhance neutron capture and in the third phase, the salt was removed and replaced by ${}^3\text{He}$, again for neutron capture to enhance the sensitivity to neutral current reactions.

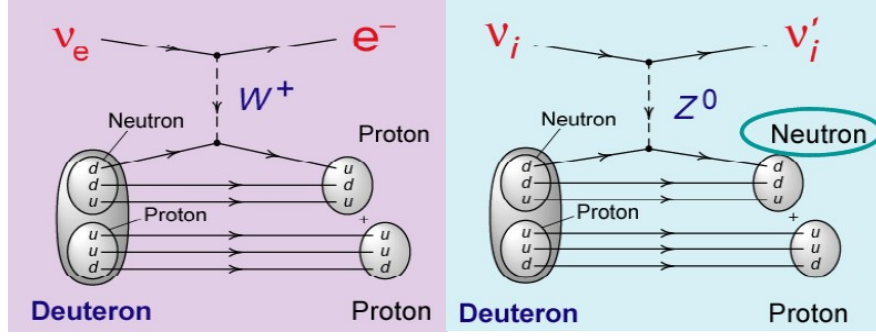
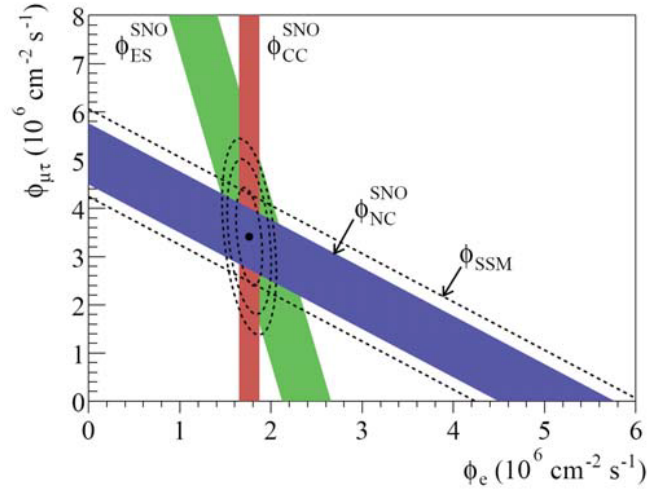


Figure 1.4: left: Neutrino detection via charged currents, basically an induced beta-decay. right: Neutrino detection with neutral currents via dissociation of deuterium.

Figure 1.5: Flux of ν_{μ} Neutrinos from the sun as measured in the SNO experiment. The dashed line shows the expectation from solar models. The red band originates from the detection of charged current interactions, i.e. electron neutrinos. The green band represents elastic scattering and the blue band neutral current reactions, which tackles all neutrino flavours. The total flux agrees with theoretical predictions and the intersection of all three bands indicates that it is composed of $1/3 \nu_e$ and $2/3 \nu_{\mu/\tau}$.



This setup allowed to measure the total neutrino flux and the flux of electron neutrinos separately. The different phases were used to cross-check the neutral current reactions with different detection techniques.

As a result, SNO concluded that the total neutrino flux from the sun matched theoretical predictions, but these neutrinos were detected in all three flavours [33]. Figure 1.5 shows the obtained results.

Mathematical Description of Neutrino Flavour Oscillations

For neutrinos to undergo flavour change, the mass eigenstate, which propagates, has to be different from the flavour eigenstate, which determines the interactions. The mass eigenstate can then be described as a superposition of flavour eigenstates. This gives a mixing matrix describing the relations between the states:

$$\begin{pmatrix} \nu_e \\ \nu_\mu \\ \nu_\tau \end{pmatrix} = \begin{pmatrix} U_{e1}^* & U_{e2}^* & U_{e3}^* \\ U_{\mu1}^* & U_{\mu2}^* & U_{\mu3}^* \\ U_{\tau1}^* & U_{\tau2}^* & U_{\tau3}^* \end{pmatrix} \cdot \begin{pmatrix} \nu_1 \\ \nu_2 \\ \nu_3 \end{pmatrix} \quad (1.16)$$

Here, ν_α are the flavour eigenstates, ν_i the mass eigenstates. The mixing matrix U is called the Pontecorvo-Maki-Nakagawa-Sakata Matrix (PMNS) and contains trigonometrical functions of three mixing angles Θ_{ij} and one non-trivial complex Dirac-phase δ_D . Factorized into these components it is commonly written as

$$U = \begin{pmatrix} 1 & 0 & 0 \\ 0 & c_{23} & s_{23} \\ 0 & -s_{23} & c_{23} \end{pmatrix} \cdot \begin{pmatrix} c_{13} & 0 & s_{13}e^{-i\delta_D} \\ 0 & 1 & 0 \\ -s_{13}e^{-i\delta_D} & 0 & c_{13} \end{pmatrix} \cdot \begin{pmatrix} c_{12} & s_{12} & 0 \\ -s_{12} & c_{12} & 0 \\ 0 & 0 & 1 \end{pmatrix} \quad (1.17)$$

If neutrinos are Majorana particles, equation (1.17) gets an additional factor containing two Majorana phases δ_M . The Majorana nature of the neutrino would allow neutrinoless double-beta decay to occur:

$$U_M = U \cdot \begin{pmatrix} e^{-i\delta_{M1}} & 0 & 0 \\ 0 & e^{-i\delta_{M2}} & 0 \\ 0 & 0 & 1 \end{pmatrix} \quad (1.18)$$

In interactions, neutrinos always participate in a flavour eigenstate which can be written as a superposition of mass eigenstates. Consider a neutrino produced at $t = 0$ in the electron-type flavour eigenstate:

$$|\nu(t=0)\rangle = |\nu_e\rangle = U_{e1}^* |\nu_1\rangle + U_{e2}^* |\nu_2\rangle + U_{e3}^* |\nu_3\rangle \quad (1.19)$$

The propagating states are the mass eigenstates with a defined energy and momentum. Therefore at a time $t > 0$ the superposition of propagated eigenstates is no longer the pure ν_e but instead:

$$|\nu(t=0)\rangle = U_{e1}^* e^{-iE_1 t} |\nu_1\rangle + U_{e2}^* e^{-iE_2 t} |\nu_2\rangle + U_{e3}^* e^{-iE_3 t} |\nu_3\rangle \quad (1.20)$$

So if the neutrino is detected after a finite time, there is a chance that it will react in another flavour eigenstate than the electron-type in which it was produced.

To determine the probability to find the neutrino in a specific flavour eigenstate it is convenient to consider the propagating mass eigenstates as a superposition of flavour eigenstates. With this, the neutrino state ν_α at a certain time t can generally be written as

$$\begin{aligned} |\nu_\alpha\rangle &= \sum_{k=1,2,3} U_{\alpha k}^* e^{-iE_k t} |\nu_k\rangle \\ |\nu_\alpha\rangle &= \sum_{\beta=e,\nu,\tau} \left(\sum_{k=1,2,3} U_{\alpha k}^* e^{-iE_k t} U_{\beta k}^* \right) |\nu_\beta\rangle \end{aligned} \quad (1.21)$$

With this notation the term in brackets gives the amplitude of the flavour transition

$$A_{\nu_\alpha \rightarrow \nu_\beta}(t) = \sum_{k=1,2,3} U_{\alpha k}^* e^{-iE_k t} U_{\beta k} \quad (1.22)$$

The probability $P(t)$ of finding a certain flavour state ν_β is given by

$$\begin{aligned} P(t) &= |\langle \nu_\beta | \nu_\alpha(t) \rangle|^2 |A_{\nu_\alpha \rightarrow \nu_\beta}(t)|^2 = \left| \sum_{k=1,2,3} U_{\alpha k}^* e^{-iE_k t} U_{\beta k} \right|^2 \\ &= \sum_{k,j} U_{\alpha k}^* U_{\beta k} U_{\alpha j} U_{\beta j} e^{-i(E_k - E_j)t} \end{aligned} \quad (1.23)$$

In the case of ultra relativistic neutrinos the exponent $-i(E_k - E_j)t$ is given by $-i \frac{\Delta m_{jk}^2 L}{2E}$ with $p_k = p = E$.

Here, $\Delta m_{jk}^2 = m_j^2 - m_k^2$ is the difference of the squared neutrino masses, L the traveled distance and E the energy of the neutrino.

It is much easier to consider mixing between only two flavours. In this scenario, the transition probability is given by:

$$P_{\alpha \rightarrow \beta}(L/E) = \sin^2(2\Theta) \sin^2\left(\frac{\Delta m^2 L}{2E}\right) \quad (1.24)$$

The transition probability is thus given by the mixing angle Θ between the mass and flavour eigenstates, the difference of the squared masses Δm^2 , the energy of the neutrino E and the traveled distance L . The mixing angle determines the amplitude of the neutrino oscillations, while the frequency is given by the mass splitting, energy and traveled distance. Neutrino energy and traveled distance can be chosen in a specific experiment and then it is possible to determine the mass differences and mixing angles. Specific experiments and their results will be discussed in the next section.

Experimental Determination of Oscillation Parameters

The three different mixing angles Θ_{12} , Θ_{13} , Θ_{23} and their corresponding mass splittings Δm_{12}^2 , Δm_{13}^2 and Δm_{23}^2 require different setups to measure. There are two principal types of experiment for measuring neutrino oscillations:

- Appearance experiments search in a neutrino ensemble created in only one flavour state for the appearance of neutrinos of a different flavour.
- Disappearance experiments look for deficits in neutrino ensembles of a known flux of a certain type of neutrinos.

Different oscillation parameters can be measured easier by one or the other method.

Θ_{12} is called the solar mixing angle, since solar neutrinos happen to be a very good sample to measure this parameter. Experiments like the aforementioned Homestake experiment as a disappearance experiment and the SNO experiment, which was sensitive to all three flavours and therefore an appearance experiment, have determined the solar neutrino parameters. The most recent results are

$$\sin^2 \Theta_{12} = 0.306(0.312)_{-0.015}^{+0.018} \quad (1.25)$$

These values are taken from the particle data group (pdg) review in 2012 [34].

The second mixing angle Θ_{23} is measured with neutrinos from cosmic ray showers and long baseline accelerator experiments. The first approach with atmospheric neutrinos is pursued for example by the Super-Kamiokande experiment [35]. These neutrinos are created in the muon- and electron-flavour state from pion decay and muon decay respectively. The fraction of muon- to electron-neutrinos in the air shower can be obtained from the following consideration:

In cosmic ray induced air showers, the neutrinos come from the hadronic part of the shower. The electromagnetic component contains only electrons and positrons from pair production and photons from bremsstrahlung. These processes alternate while the shower progresses through the atmosphere until the energies of individual particles are too low for pair production. Therefore, this component does not produce any neutrinos. Regardless of the initial reaction in the hadronic part, the ratio of muon- to electron type neutrinos is determined by pion decay. Charged pions produced in nuclear interactions of the shower particles with atmospheric nuclei decay into muons

$$\pi^\pm \rightarrow \mu^\pm + (\bar{\nu}_\mu) \quad (1.26)$$

where one muon type neutrino is produced. The muons decay further into electrons:

$$\mu^\pm \rightarrow e^\pm + (\bar{\nu}_e) + (\bar{\nu}_\mu) \quad (1.27)$$

In this second interaction, another muon-type neutrino and an electron-type neutrino are produced. To first order, the ratio of muon- to electron-type neutrinos is 2 : 1. This is modified by a fraction of pions decaying directly into electrons, and muons that live long enough to reach the earth's surface without producing further neutrinos. But these effects are well studied by cosmic ray experiments like Cascade/Kascade Grande [36] and the Pierre-Auger-Observatory [37]. With this information it is possible to compare the measured neutrino flux of electron- and muon-type neutrinos to the produced quantity.

Long Baseline experiments like MINOS [38], T2K [39] or OPERA [40] for example use pure-flavour neutrino beams produced in accelerator facilities by fixed target collisions. A detector is placed in a distance given by equation (1.22), since the neutrino energy is determined by the beam energy of the accelerator.

The most up-to-date summary of results is again given by the pdg review [34]:

$$\sin^2 \Theta_{23} = 0.42_{-0.03}^{+0.08} \quad (1.28)$$

In recent years, there has been a great effort to measure Θ_{13} with reactor experiments. Since the CHOOZ experiment provided only an upper limit [41], more recent experiments like Double CHOOZ [42], RENO [43] and Daya Bay [44] have raced to determine Θ_{13} . The current results from the cited publications are:

$$\begin{aligned} \sin^2 2\Theta_{13} &= 0.092 \pm 0.016 \pm 0.005 \quad (\text{DayaBay}) \\ \sin^2 2\Theta_{13} &= 0.113 \pm 0.013 \pm 0.019 \quad (\text{RENO}) \\ \sin^2 2\Theta_{13} &= 0.086 \pm 0.041 \pm 0.030 \\ &\text{or } 0.017 < \sin^2 2\Theta_{13} < 0.16 \quad (\text{DoubleCHOOZ}) \end{aligned} \quad (1.29)$$

All these experiments use electron neutrinos from nuclear power reactors and look for a disappearance on short baselines. On this scale, the oscillation into muon-type neutrinos is insignificant at these energies due to the larger mass splitting. To improve sensitivity the new generation experiments also use a near detector to directly measure the flux of electron neutrinos and abolish the need to rely on calculations based on the power output of the reactors.

A combined analysis of the most recent data from T2K, MINOS, Daya Bay, RENO and DoubleCHOOZ conducted in [45] gives the following best fit:

$$\sin^2 2\Theta_{13} = 0.096 \pm 0.013 (\pm 0.040) \text{ at } 1\sigma (3\sigma) \quad (1.30)$$

Along with the mixing angles, the mass splittings have been determined by oscillation experiments. But since the measured quantity is the difference of squared masses Δm^2 instead of Δm , it is not possible to determine the exact hierarchy of the neutrino mass eigenstates. The two mass splittings accessible with oscillation experiments are usually referred to as solar and atmospheric mass splittings Δm_{\odot}^2 and Δm_{atm}^2 . These parameters have been derived from a global fit given in the pdg 2012 review [34] to be:

$$\begin{aligned} \Delta m_{\odot}^2 [10^{-5} \text{ eV}^2] &= 7.58_{-0.26}^{+0.22} \\ \Delta m_{\text{atm}}^2 [10^{-3} \text{ eV}^2] &= 2.35_{-0.09}^{+0.12} \end{aligned} \quad (1.31)$$

Since the sign of the mass splitting is not known, this allows for two distinct scenarios, the normal and inverted hierarchy. In the normal hierarchy, the smaller mass splitting Δm_{\odot}^2 connects ν_1 and ν_2 , and the larger Δm_{atm}^2 connects ν_2 and ν_3 . In the inverted scenario, ν_1 and ν_2 are separated by Δm_{atm}^2 and ν_2 and ν_3 have only the small mass splitting Δm_{\odot}^2 . The two scenarios are illustrated in Figure 1.6 from [46].

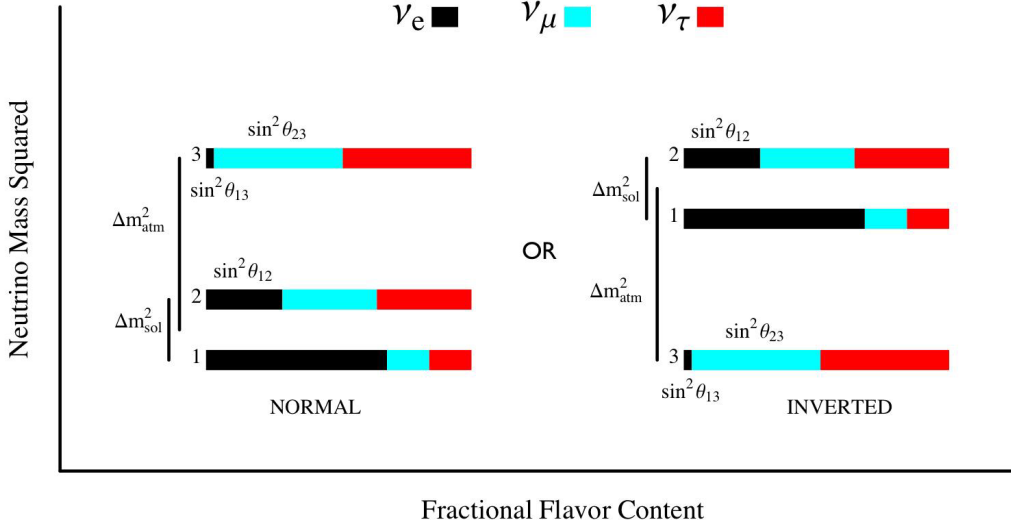


Figure 1.6: Neutrino mass hierarchy scenarios. The coloured parts of the bars indicate the fraction of the respective flavour eigenstates composing the mass eigenstates. **Left:** In the normal hierarchy scenario, the smaller solar mass splitting is the mass difference between the lower two mass eigenstates. The third eigenstate is again set apart from the second by the larger atmospheric mass splitting. **Right:** In the inverted hierarchy scenario, the lowest mass eigenstate is set apart from the other two by the large atmospheric mass splitting, while the remaining eigenstates are split by the solar mass splitting.

If the mass of the lowest mass eigenstate would already be in the eV range, the mass splitting would be relatively small and the masses of the neutrino mass eigenstates would be quasi-degenerate.

To measure the absolute mass scale of neutrinos, oscillation experiments are inadequate and another approach has to be taken.

1.3.2 Direct Neutrino Mass Experiments

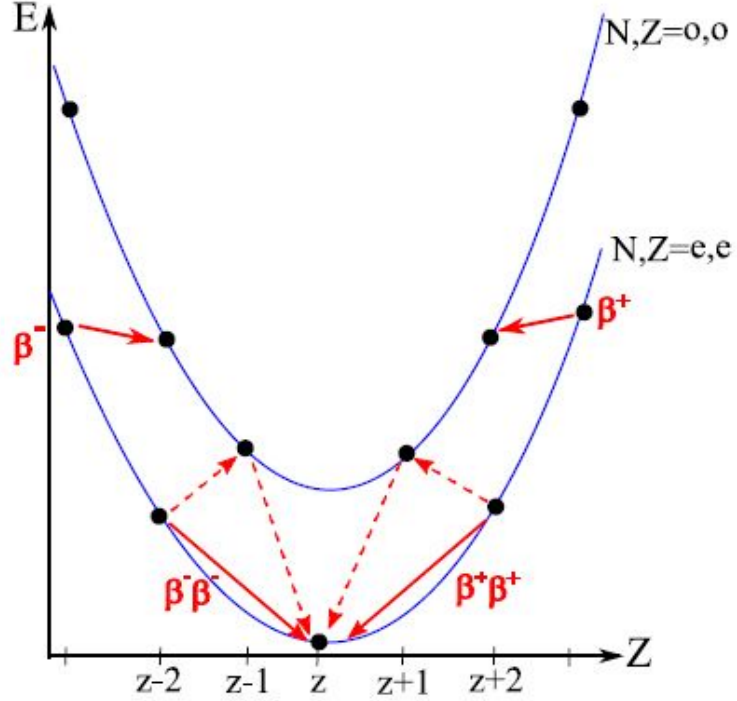
Neutrinoless Double- β -Decay Experiments

Neutrinoless double- β -decay offers a possibility to access the absolute neutrino mass, but only if the neutrino is a Majorana particle, i.e. its own antiparticle. If this was the case, neutrinos and anti-neutrinos would only be set apart by their helicity, neutrinos being right-handed, anti-neutrinos left handed.

Double- β -decay isotopes require that the daughter nucleus $(A, Z + 1)$ of a single- β -decay of the nucleus (A, Z) would be an energetically higher state. But when the nucleus $(A, Z + 2)$ is again energetically lower than (A, Z) , it is possible for the decay

$$(A, Z) \rightarrow (A, Z + 2) \quad (1.32)$$

Figure 1.7: Mass parabola of double- β -decay elements. Nuclei with an even atomic mass number A can only have either odd-odd nucleon number N and charge number Z (upper parabola) or even-even N and Z (lower parabola). β -decay can only occur if the energy of the daughter nucleus ($N, Z\pm 1$) is lower than that of the original nucleus (N, Z). If this is not the case, but ($N, Z\pm 2$) is energetically lower, then (N, Z) can undergo two subsequent β -decays as shown by the dashed lines. This figure is taken from [48].



to happen, i.e. two coincident β -decays via the virtual state ($A, Z + 1$). This is further illustrated in figure 1.7. In the nuclear shell model this is only possible for isotopes with an even nucleon number A because those have an even-even or odd-odd nuclei number N and charge number Z configuration. Double- β -decay was first observed in 1987 with a ^{82}Se sample [47]. In this type of decay two electrons and two electron neutrinos are emitted. Therefore it is a multi body decay and the electrons show a continuous spectrum.

In neutrinoless double- β -decay ($0\nu\beta\beta$) only two mono-energetic electrons are emitted. This is only possible if the left handed electron anti-neutrino $\bar{\nu}_e$ created in one β -decay-vertex is absorbed as a right-handed electron-neutrino ν_e in the second vertex. Figure 1.8 shows the Feynman-diagrams of ($2\nu\beta\beta$) and ($0\nu\beta\beta$) reactions.

The undisputed discovery of such a mono-energetic line above the continuous double- β -spectrum as sketched in figure 1.9 would be proof that the neutrino is a Majorana particle. A measurement of the half-life of the ($0\nu\beta\beta$) decay would allow a determination of the effective majorana mass m_{ee} of the electron anti-neutrino. This mass is a coherent sum of the mass eigenstates constituting the electron neutrino:

$$m_{ee} = \left| \sum_i U_{ei}^2 \cdot m_{\nu i} \right| \quad (1.33)$$

It is possible for the matrix elements U_{ei}^2 to contain complex phases as shown in (1.17) and (1.18). This may lead to cancellations in the effective mass sum. The most stringent

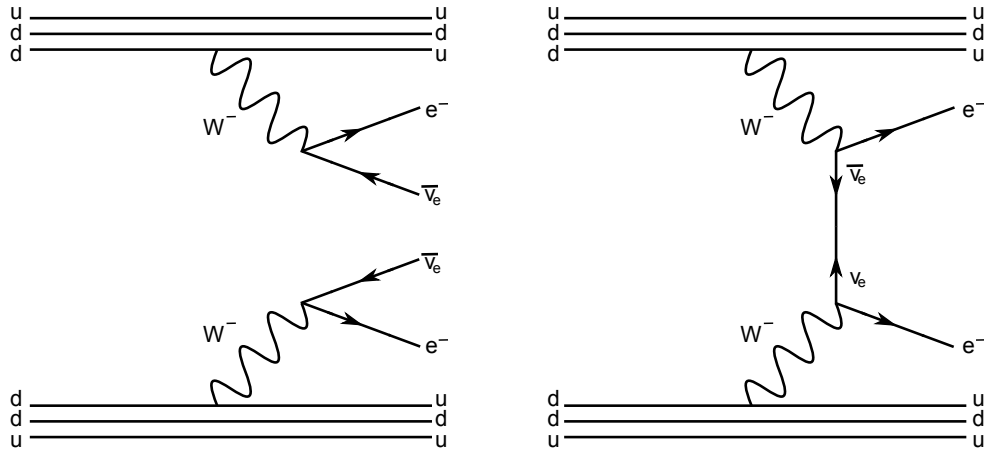


Figure 1.8: Left: Feynman-diagram of standard double- β -decay: Two neutrinos and two electrons are emitted. **Right:** Feynman-diagram of neutrinoless double- β -decay: the anti-neutrino created in one vertex is absorbed as a neutrino in the second vertex. Only two mono-energetic electrons are emitted.

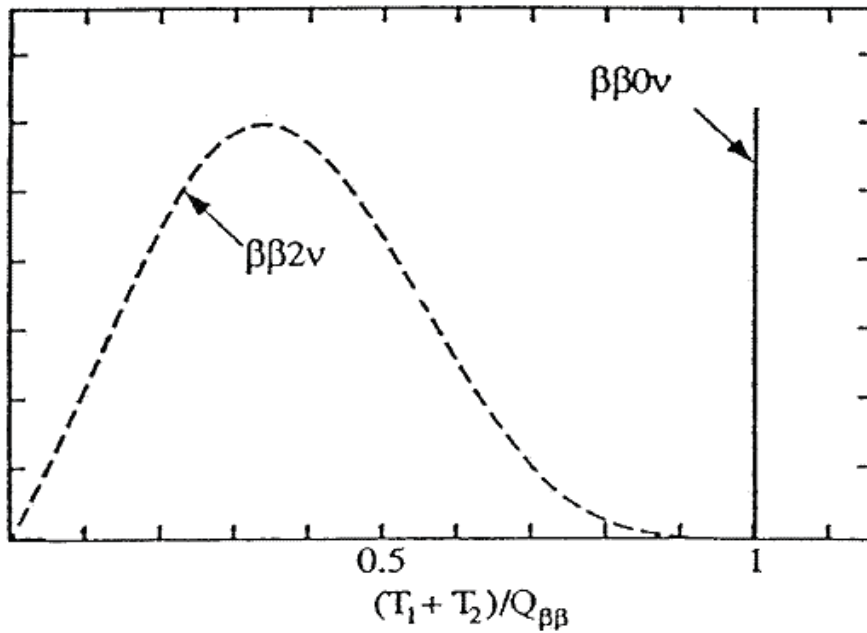


Figure 1.9: Energy signature of neutrinoless double- β -decay, the two mono-energetic electrons produce a peak above the continuous spectrum of standard double- β -decay electrons. This figure is taken from [49].

upper limit up to date has been determined by the Heidelberg-Moscow experiment. Via the observation of 10 kg of enriched ^{76}Ge , with a total exposure of 71.7 kgy, it could produce an upper limit of $m_{ee} < 0.35 \text{ eV}/c^2$ [50]. A part of the collaboration claims to have found an actual mass of $m_{ee} = 0.44 \text{ eV}/c^2$ [51], but this result is a topic of heated discussion and not universally accepted. To prove or refute this claim, the GERmanium Detector Array GERDA [52] uses the ^{76}Ge from the Heidelberg-Moscow experiment as well as additional detectors. Improved sensitivity and lower background will determine the truth about the $m_{ee} = 0.44 \text{ eV}/c^2$ claim. Other double- β -decay experiments like CUORE [53], SuperNEMO [49], EXO [54] and Majorana [55] also search for the mono energetic signature of neutrinoless double- β -decay.

Kinematic Neutrino Mass Experiments

If the neutrino is not a Majorana particle, double- β -decay experiments will be unable to find a mono-energetic peak above the continuous spectrum, and thus would be unable to measure any neutrino mass.

The kinematics of single- β^- -decay provides a model-independent indicator for the mass of the electron anti-neutrino. In this weak interaction, a nucleus (A, Z) decays into its daughter nucleus $(A, Z + 1)$ via the emission of an electron e^- and an electron anti-neutrino $\bar{\nu}_e$. In this 3-body decay, the electron has a continuous energy spectrum. Since the nucleus is orders of magnitudes more massive than the electron and the neutrino it can be assumed to stay at rest. Consequently, the energy of the decay is distributed among the other decay products. The weakly interacting neutrino leaves the detector without any interaction and only the electron can be measured. The shape of the electron energy spectrum dN/dt in the energy region E to $E + dE$ can be derived from Fermi's golden rule

$$\frac{dN}{dt} = \frac{d^2N}{dt dE} = \frac{2\pi}{\hbar} |\mathcal{M}| \rho(E) \quad (1.34)$$

where $\rho(E)$ is the phase-space density of the possible end states of electron and electron anti- neutrino and \mathcal{M} the nuclear matrix element.

As shown in [56] dN/dt is then

$$\frac{dN}{dt + dE} = R(E) \cdot \sqrt{(E_0 - E)^2 - m_{\nu_e}^2 c^4} \cdot \Theta(E_0 - E - m_{\nu_e} c^2) \quad (1.35)$$

with

$$R(E) = \frac{G_F^2}{2\pi^3 \hbar^7 c^5} \cos^2 \Theta_C |\mathcal{M}^2| F(Z + 1, E) \cdot p \cdot (E + m_e c^2) \cdot (E_0 - E) \quad (1.36)$$

- E is the kinetic energy of the electron, $m_e c^2$ its mass and p its momentum.
- E_0 is the end point energy, the maximal kinetic energy of the electron for a vanishing neutrino mass.

- $m_\nu c^2$ is the rest mass of the electron anti neutrino.
- $F(Z+1, E)$ is the Fermi function with the charge number of the daughter nucleus ($Z+1$).
- G_F is the Fermi constant.
- \mathcal{M} is the nuclear matrix element.
- Θ_C is the Cabbibo angle.
- $\Theta(E_0 - E - m_\nu)$ is the Heaviside function, it is included for reasons of energy conservation.

Since contemporary mass experiments are not sensitive to the small mass splittings described in (1.31), the neutrino mass used in (1.35) is an effective electron anti-neutrino mass given by the incoherent sum over the mass eigenstates

$$m_{\nu\text{eff}}^2 = \sum_i |U_{ei}^2| \cdot m_{\nu_i}^2 \quad (1.37)$$

In contrast to the coherent sum measured by neutrinoless double- β -decay experiments here no mass term cancellations due to the complex phases can occur. If the mass of one neutrino flavour eigenstate is measured with this approach, it is possible to determine the spectrum of the mass eigenstates with knowledge of the matrix elements U_{ei} and mass differences Δm_{\odot}^2 and Δm_{atm}^2 from oscillation experiments.

When measuring the β -decay spectrum, only the region near the endpoint, where $m_{\nu_e}^2 c^4$ is comparable to $(E_0 - E)^2$, contains information about the neutrino mass. But only a small fraction of electrons happen to be in that energy range. Therefore it is desirable to have an isotope with an energy endpoint as low as possible.

The element with the lowest β -decay energy endpoint is ^{187}Re , but the downside of this isotope is its long half-life of $t_{\frac{1}{2}} = 4.35 \cdot 10^{10}$ a. To achieve a usable rate, large quantities of material have to be observed. Experiments using ^{187}Re like MARE [57] use cryogenic bolometers which serve simultaneously as source and as detector. The energy deposited by the stopped decay electron heats the crystal and the temperature rise can be measured by micro-calorimeters. This allows to determine the electron energy and consequently the energy spectrum of ^{187}Re . The highest sensitivity of $m_{\nu_e} < 15$ eV/ c^2 with this approach was achieved by the Milano experiment [58].

Another viable isotope is tritium, with a rather low endpoint but a much shorter half life of $t_{\frac{1}{2}} = 12.3$ a. This allows for higher statistics in shorter time and makes up for the disadvantage of a slightly higher endpoint. The energy spectrum of tritium- β -decay has been analyzed since the 1950s, and offered the highest sensitivity on m_{ν_e} up to date. The experiments to achieve the best upper limits on the neutrino mass with this technique were the Mainz [59] ($m_{\nu_e} < 2.3$ eV/ c^2) and Troitsk [13] ($m_{\nu_e} < 2.05$ eV/ c^2) experiments. Both have reached their maximum achievable sensitivity and are concluded.

Reviewing the contents of this chapter, it becomes evident that a new experiment with sub-eV sensitivity is needed to measure the neutrino mass in a model-independent way. With this, cosmologically relevant neutrino mass regions and the so far inconclusive results of double- β -decay experiments can be explored and validated. The **K**arlsruhe **T**ritium **N**eutrino experiment KATRIN is such an experiment. This work is part of the effort to measure the effective absolute mass of the electron anti-neutrino with the KATRIN experiment, which is currently being built at the Campus North of the Karlsruhe Institute of Technology.

2. The KATRIN Experiment

The **K**arlsruhe **T**ritium **N**eutrino experiment is designed to investigate the endpoint of the energy spectrum of tritium- β -decay electrons. With this information it will be able to determine the absolute effective mass of the electron-antineutrino with an unprecedented sensitivity of $m_{\bar{\nu}_e} = 0.2 \text{ eV}/c^2$ [15]. Since this method involves only purely kinematical observables as well as the fundamental principles of energy- and momentum conservation, it allows for a model-independent measurement of the neutrino mass. The measured quantity in this process is m_{ν}^2 and the KATRIN sensitivity limit of this quantity is an improvement by a factor of 100 with respect to the predecessor experiments in Mainz [59] and Troitsk [13]. This goal imposes high demands on all components of the experiment. Energy resolution of the system, achievable statistics as well as background reduction are critical for the success of the project. To achieve the best possible performance all systems must be driven to the technically feasible state of the art. Basic informations in this chapter are taken from the KATRIN design report [15]. Updated information is taken into account and referenced separately.

2.1 Tritium-Beta-Decay

As described in section 1.3.2, the mass of the electron anti neutrino can be obtained from the form of the electron energy spectrum of tritium- β -decay



by observing the electron rates near the endpoint $E_0 = 18.57 \text{ keV}$ of the spectrum.

The mass of the electron anti neutrino m_{ν_e} enters in the form of the spectrum

$$\frac{dN}{dE} = R(E) \sqrt{(E_0 - E)^2 - m_{\nu_e}^2 c^4} \Theta(E_0 - E - m_{\nu_e} c^2) \quad (2.2)$$

only as a kinematic term. So, β -decay allows for a model independent determination of the neutrino mass. It is therefore irrelevant, whether the neutrino is a dirac or a majorana particle, in contrast to measurements using the half-life of neutrinoless double- β -decay or cosmological derivations.

Figure 2.1 shows a comparison between two spectrum models, one with $m_{\nu} = 1 \text{ eV}/c^2$ and the other with $m_{\nu} = 0$.

The signature of a nonvanishing neutrino mass is only apparent near the endpoint of the spectrum. Most decay electrons do not carry any information about the neutrino

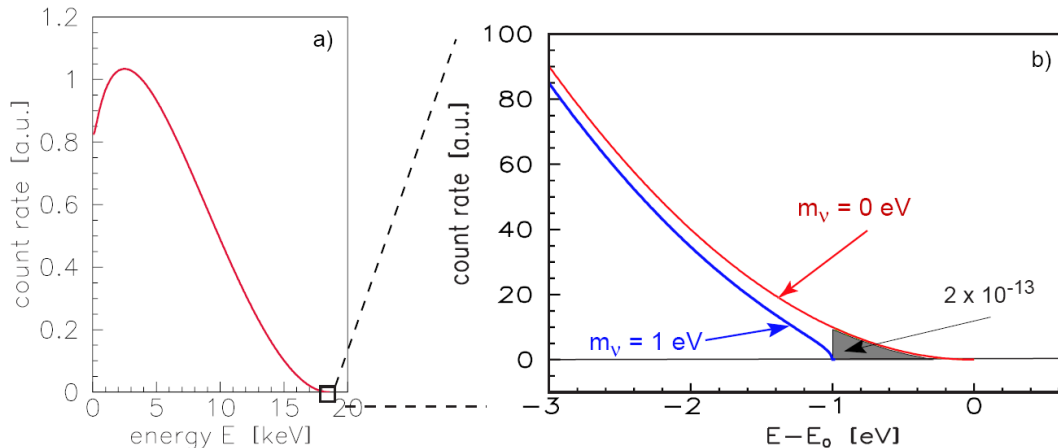


Figure 2.1: **Left:** Spectrum of the kinetic energy of tritium- β decay electrons. **Right:** Zoom in on the endpoint region. The red curve shows the spectrum for a vanishing neutrino mass, the blue curve is a spectrum as it would be expected for a neutrino mass of 1 eV. The signature KATRIN is looking for is a shift in the form of the spectrum.

mass. The fraction of electrons emitted within 1 eV of the endpoint is only $2 \cdot 10^{-13}$. This leads to the need for a high luminosity in β -decay experiments and simultaneously a fine energy resolution.

The choice of tritium over other elements in the KATRIN experiment can be understood when considering the following points:

Tritium has the second lowest energy endpoint combined with a very low half-life of only $t_{\frac{1}{2}} = 12.3$ a. Electrons with energies lower than a few eV below the endpoint carry no information about the neutrino mass. Choosing an element with a low endpoint energy increases the fraction of electrons that can be used for neutrino mass analyses. Compared with Rhenium, the element with the lowest endpoint and a half-life of $t_{\frac{1}{2}} = 4.35 \cdot 10^{10}$ a this translates to a luminosity of a factor $> 10^8$ higher.

Furthermore, tritium ${}^3\text{H}$ and its daughter nucleus helium ${}^3\text{He}^+$ have simple and therefore precisely computable electron shell configurations. The nuclear matrix element $\mathcal{M}^2 = 5.55$ can be calculated with high precision and is furthermore energy independent due to the super-allowed nature of the decay [60].

Having this in mind, the KATRIN experiment was designed with a windowless, gaseous tritium source and an electrostatic spectrometer of the MAC-E Filter principle. The combination of these components allows for the highest possible sensitivity on the mass of the electron anti neutrino.

2.2 The KATRIN Measurement Principle

2.2.1 MAC-E Filter

The **m**agnetic **a**diabatic **c**ollimation with **e**lectrostatic filtering is a technique used by the KATRIN experiment and its predecessors in Mainz and Troitsk to measure the

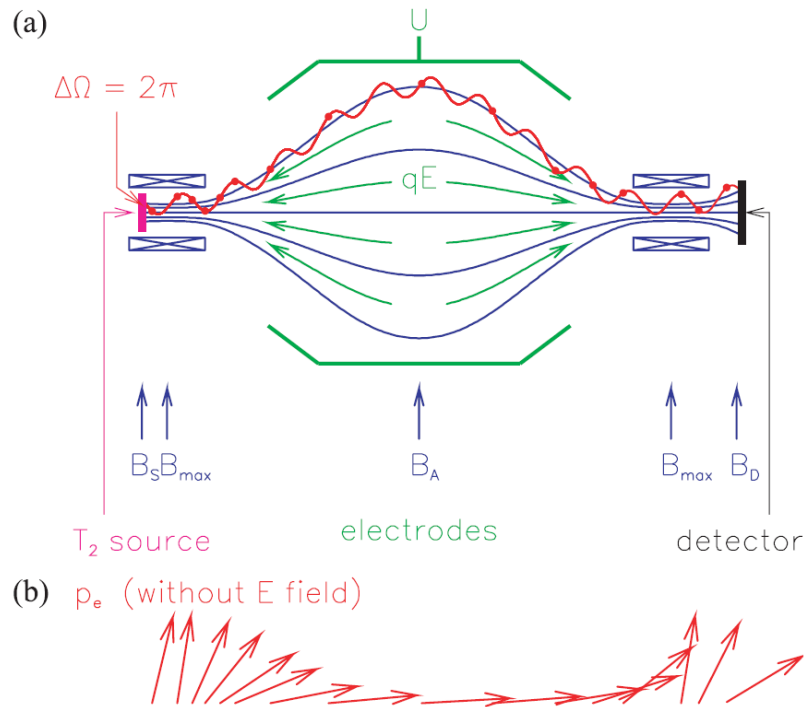


Figure 2.2: Schematic of a MAC-E Filter: Two solenoids create a magnetic field that guides the electrons and transforms their rotational movement into longitudinal movement. An electrode system creates a retarding electrostatic potential that discriminates electrons with regard to their longitudinal energy. The detector registers the fraction of electrons that have passed the electrostatic barrier.

energy spectrum of electrons near the endpoint of tritium- β -decay. The electrostatic filter provides a high energy resolution and the collimation grants the spectrometer a large emission angle acceptance of nearly 2π . The method was first proposed in [61] and has since been very successful.

The principle setup of an MAC-E Filter as shown in figure 2.2 consists of two solenoid magnets that create an axially symmetric, inhomogeneous field to guide the electrons from the decay through the spectrometer. There, a cylindrical electrode system creates an electrostatic potential barrier. This barrier either transmits or reflects incoming electrons, depending on their energy. Since radioactive sources emit isotropically, the incoming electrons have different distributions of cyclotron and longitudinal energy. The magnetic field gradient transforms the energy of the rotational motion into longitudinal motion which can be analysed by the electrostatic potential. This setup allows for a very high energy resolution combined with a large angle acceptance, both critical attributes, as explained above.

The transformation of kinetic energy perpendicular to the electric field into longitudinal kinetic energy needs to be adiabatic. In order to ensure adiabaticity, the transformation

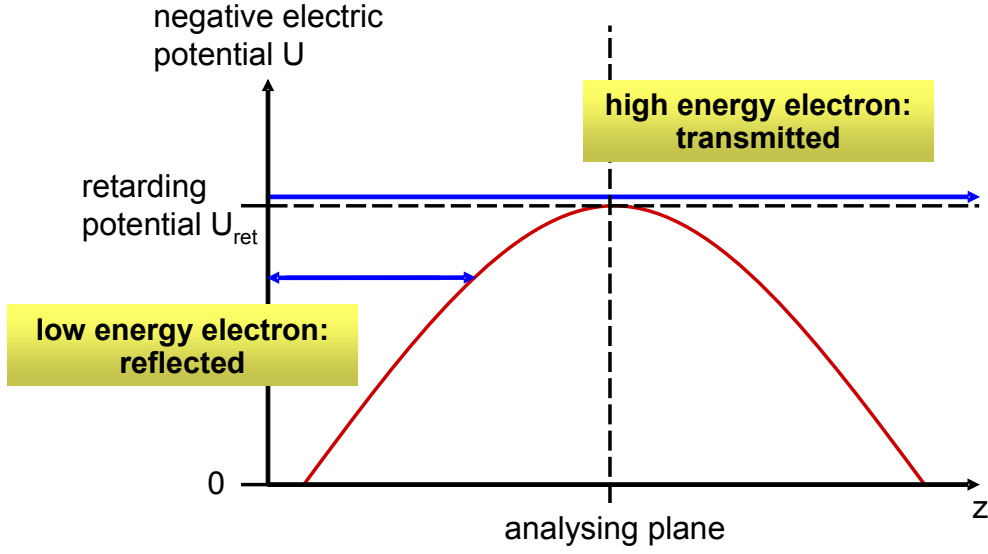


Figure 2.3: Energy analysis by retarding electrostatic potential: Only electrons with a sufficiently large energy can pass the analysing plane, electrons with an energy lower than $E = qU_{\text{ret}}$ are reflected.

has to be slow so that the magnetic moment of the electron with respect to its cyclotron motion is conserved [62]:

$$\mu = \frac{E_{\perp}}{B} = \text{const.} \quad (2.3)$$

This means, that the transversal energy E_{\perp} decreases with the magnetic field. In the case of the KATRIN main spectrometer, the ratio between the maximal magnetic field and the magnetic field in the analysing plane is $\frac{|\vec{B}_{\text{max}}|}{|\vec{B}_{\text{a}}|} = \frac{6 \text{ T}}{0.3 \text{ mT}} = 20000$. This is then also the factor by which the transversal energy is reduced. So when the electron has traveled from the entrance of the MAC-E filter to the analysing plane almost all of its energy is in the longitudinal motion and can thus be analysed by the retarding potential. Then, while it is traveling towards the exit and the magnetic field is increasing, its energy is transformed back to the original configuration.

But again, the basic principle of energy analysis is rather simple: An electrostatic barrier repels electrons and only those with sufficiently large energy pass the analysing plane as sketched in 2.3.

Acceptance angle

The following derivations are done extensively in [63]. The maximum magnetic field also sets the maximal angle under which electrons can be emitted from the source and still reach the detector. This angle Θ_{max} depends on the ratio of the magnetic

field strength in the source $|\vec{B}_s|$ and the maximal field strength $|\vec{B}_{\max}|$. Consider the magnetic moment of the electron in the source and at the location of maximal field:

$$\frac{E_{\perp s}}{|\vec{B}_s|} = \frac{E_{\perp \max}}{|\vec{B}_{\max}|} \quad (2.4)$$

Since the Energy E is proportional to the squared momentum $E \propto p^2$, and the transversal momentum is $p_{\perp} = P \sin(\Theta)$, the transverse energy is

$$E_{\perp} = E \sin^2(\Theta) \quad (2.5)$$

The maximal angle is reached, when the angle at the point of strongest magnetic field is 90° , meaning all kinetic energy is in the transversal motion $E_{\perp} = E$. Then 2.4 becomes

$$\frac{E \sin^2(\Theta_{\max})}{|\vec{B}_s|} = \frac{E}{|\vec{B}_{\max}|} \quad (2.6)$$

From here, the maximum acceptance angle Θ_{\max} for the nominal field strengths $|\vec{B}_s| = 3.6 \text{ T}$ and $|\vec{B}_{\max}| = 6 \text{ T}$ follows as

$$\sin(\Theta_{\max}) = \sqrt{\frac{|\vec{B}_s|}{|\vec{B}_{\max}|}} \quad (2.7)$$

$$\Rightarrow \Theta_{\max} = 51^\circ \quad (2.8)$$

Energy resolution

The maximal field strength in the KATRIN setup is inside the pinch magnet bore, at the exit of the main spectrometer. This means, that an electron with sufficient energy to pass the electrostatic barrier may be reflected nonetheless, if its starting angle was too large. On the other hand, higher energy electrons retain a fraction of their transversal energy in the analysing plane since the magnetic field does not drop to zero. Consider an electron with a starting angle $\Theta = \Theta_{\max}$ which is transmitted and an electron with a starting angle $\Theta = 0$ of the same energy which is obviously also transmitted. The difference in kinetic energy of these electrons in the analysing plane is the energy resolution of the MAC-E filter. The energy resolution describes the fact, that electrons may be reflected although they have sufficient energy to pass the electrostatic barrier.

It can be derived as:

$$\begin{aligned}
\Delta E &= E_{\perp\Theta_{\max}}^a - E_{\perp\Theta_0}^a = E_{\perp\Theta_{\max}}^a \\
\Delta E &= E_{\perp\Theta_{\max}}^s \cdot \frac{|\vec{B}_a|}{|\vec{B}_s|} \\
\Delta E &= E_{\perp\Theta_{\max}}^{\max} \cdot \frac{|\vec{B}_a|}{|\vec{B}_{\max}|} \\
\Delta E &= E \cdot \frac{|\vec{B}_a|}{|\vec{B}_{\max}|}
\end{aligned} \tag{2.9}$$

For the KATRIN experiment with $E = 18.6$ eV, $|\vec{B}_a| = 3 \cdot 10^{-4}$ T and $|\vec{B}_{\max}| = 6$ T this gives:

$$\Delta E = 0.93 \text{ eV} \tag{2.10}$$

Transmission function

The dependency of transmission on the acceptance angle means that the transmission probability is not a clear Heaviside Θ -Function. It rather depends on the electron energy in a more complicated way.

While passing through the spectrometer, the transversal motion of an electron is transformed into longitudinal motion, while at the same time the electrostatic potential reduces its longitudinal energy as the electron moves against the potential barrier and gains potential energy. At the analysing plane, the equipotential area at the highest potential, it is only transmitted if its longitudinal energy is positive

$$E_{\parallel a} \geq 0 \tag{2.11}$$

Since the field gradients are low due to the size of the KATRIN apparatus, the electron motion is adiabatic and the magnetic moment is conserved. Therefore the sum of kinetic and potential energy does not change:

$$\begin{aligned}
E_s + qU_s &= E_a + qU_a \\
&= E_{\parallel a} + E_{\perp a} + qU_a \\
\Rightarrow E_{\parallel a} &= E_s - E_{\perp a} + q(U_s - U_a)
\end{aligned} \tag{2.12}$$

with (2.4) and (2.5) this gives

$$E_{\parallel a} = E_s - E_s \sin^2(\Theta_{\max}) \frac{|\vec{B}_a|}{|\vec{B}_s|} + q(U_s - U_a) \quad (2.13)$$

from here, with (2.11) this leads to

$$0 = E_s - E_s \sin^2(\Theta_{\max}) \frac{|\vec{B}_a|}{|\vec{B}_s|} + q(U_s - U_a) \quad (2.14)$$

$$\Rightarrow \sin^2(\Theta_{\max}) = \frac{E_s + q(U_s - U_a)}{E_s} \frac{|\vec{B}_s|}{|\vec{B}_a|} \quad (2.15)$$

With this relation between starting angle and energy it is possible to derive the probability of an electron with a certain energy to be transmitted. For this, the angular distribution of the source is needed. But for a gaseous radioactive source, it is reasonable to assume an isotropic distribution. Then, the cosine of the starting angle is equally distributed. Therefore, the probability for an electron to be emitted with an angle $\Theta < \Theta_{\max}$ is given by:

$$T(\Theta < \Theta_{\max}) = 1 - \cos(\Theta_{\max}) \quad (2.16)$$

using (2.15) yields

$$T(E_s, qU) = 1 - \sqrt{1 - \frac{E_s + q(U_s - U_a)}{E_s} \frac{|\vec{B}_s|}{|\vec{B}_a|}} \quad (2.17)$$

This is the transmission function. It describes the fraction of electrons with a starting energy E that are transmitted. It is a fundamental property of the MAC-E Filter, the narrower the transmission function, the better the energy resolution of the spectrometer. Various effects may worsen the transmission function and have to be carefully checked and taken into account or corrected. Aside from background electrons tampering with the measurement other effects include time variations in the source parameters (density, temperature, etc.), space-charge effects, scattering of signal electrons on residual gas, the final states of the ${}^3\text{HeT}^+$ ions, time fluctuations of the retarding potential and lastly inhomogeneities in the electric and magnetic fields. Great care has to be taken in handling these challenges.

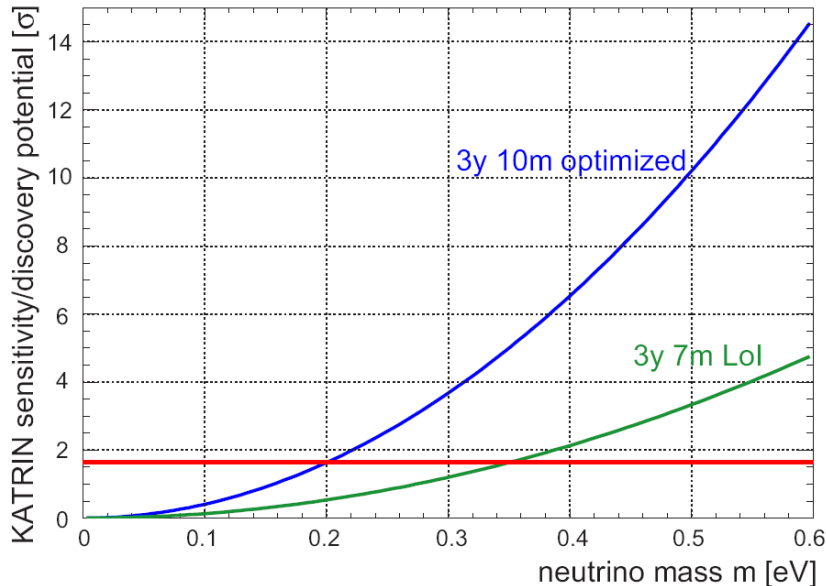


Figure 2.4: Sensitivity of the KATRIN experiment: KATRIN will be sensitive to sub-eV neutrino masses after three years of measurement time. The blue curve shows the sensitivity for the current design, compared to the original design with a smaller spectrometer (green curve). The red line is the sensitivity limit for an upper mass limit.

2.3 An Overview of the KATRIN Experiment

The **K**arlsruhe **T**ritium **N**eutrino experiment uses the MAC-E filter technique described above to analyse the energy spectrum of electrons from tritium β -decay. From this spectrum, the mass of the electron antineutrino can be deduced. The smallness of the neutrino mass presents a big challenge on the sensitivity of the experiment.

The design specifications aim for a discovery potential of a neutrino mass of $0.35 \text{ eV}/c^2$ with 5σ significance after three years of measurement time, or an upper exclusion limit of $0.2 \text{ eV}/c^2$ at 90% C.L. if no mass can be determined. Figure 2.4 shows the sensitivity of the KATRIN experiment depending on the neutrino mass.

To achieve this sensitivity all components of the experiment have to work in concert with each other. Only through great effort on all accounts and consideration of all details can this be done. Figure 2.5 shows an overview of the KATRIN experiment and its components which will be introduced in the following sections.

2.3.1 Windowless Gaseous Tritium Source

The radioactive source used in the KATRIN experiment consists of molecular gaseous tritium with a high purity. The gas is injected into the 10 m long WGTS source tube via capillaries at $T = 27 \text{ K}$ at an isotopic purity of $> 95 \%$ [64]. The molecules diffuse in approximately 1 s towards both ends of the source tube where pumps are installed. This leads to a nonlinear density profile in the source. The inlet pressure allows a regulation of the source density. The integrated density along the axis of the beam tube is called

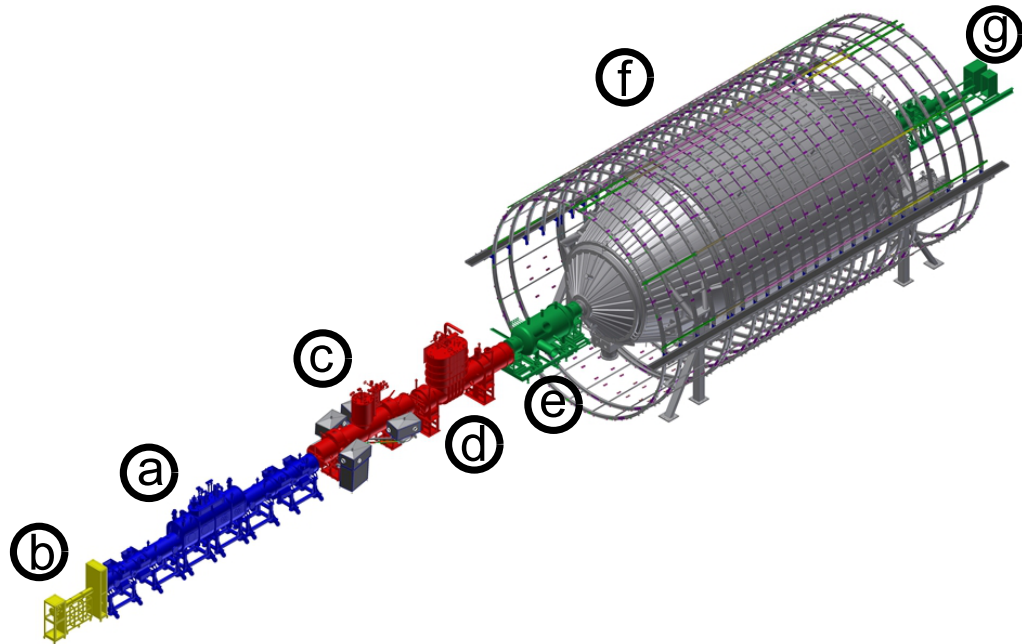


Figure 2.5: Overview of the KATRIN experiment. Blue: Windowless gaseous tritium source (a). Yellow: Rear section (b). Red: transport section with differential (c) and cryogenic (d) pumping section. Green: Pre-spectrometer (e) Grey: Main spectrometer (f) and its air coil system, and behind it the detector (g).



Figure 2.6: The windowless gaseous tritium source consists of a 16 m long cryostat containing the beam tube. This 90 mm beam tube is kept on a stable temperature by a 2-phase neon cooling system

the column density [65]. The stability of the column density directly affects the stability of the source luminosity. Therefore it has to be monitored constantly [66].

The decay probability of a tritium molecule while traveling through the source is 10^{-9} . The electrons which are emitted in forward direction are guided adiabatically by a magnetic field of $B_s = 3.6$ T through the transport section to the spectrometer. $5 \cdot 10^{19}$ molecules are injected per second. This results in a total of $1.8 \cdot 10^{11}$ decays per second in the analysed flux tube of 191 Tcm^2 .

To achieve a stable rate, the column density has to be very stable which depends on the inlet pressure and the temperature of the source gas along the 10 m beam tube. The low temperature also minimizes the effects of a doppler-shift on the electron energy due to the thermal molecule motion. Measurements with the WGTS-demonstrator, which is currently upgraded to the full WGTS cryostat, have achieved a much better stability than the design limit of 30 mK [67] [68].

2.3.2 Transport Section

The transport section is directly attached to the WGTS. Its purpose is twofold. First it has to guide the electrons adiabatically from the source to the spectrometer section and secondly it has to extract the tritium from the beam tube, so that it cannot decay inside the spectrometers and add to the background rate. The requirements on the background rate of the main spectrometer of $10^{-3} / \text{s}$ allow a maximum partial tritium pressure of 10^{-20} mbar. To achieve this goal with the nominal pumping speed of the main spectrometer, no more than $10^{-14} \frac{\text{mbar} \cdot \text{l}}{\text{s}}$ flow into the vacuum vessel. The source parameters discussed above imply that the transport section must reduce the tritium flow by a factor of 10^{14} . This is achieved by a sequential combination of differential and cryogenic pumping.

Differential Pumping Section

Adjacent to both ends of the WGTS are the differential pumping sections DPS1-F (front) and DPS1-R (rear). Due to their proximity to the source they have to be kept on the same strict operating conditions as the WGTS and are integrated into the WGTS cryostat. At the back of the DPS1-R is the rear section which contains monitoring devices for the source parameters [69]. Downwards along the beamline following the DPS1-F is the DPS2-F, shown in figure 2.7.

The DPS2-F contains a series of 4 pump-ports, equipped with turbomolecular pumps. The combined differential pumping of DPS1-F and DPS2-F reduces the flow of neutral tritium gas by a factor of 10^7 . Furthermore, the beam tube is bent twice in a 20° angle to prevent neutral tritium molecules to directly travel further down the beamline. Unfortunately, positive ions such as the decay product ${}^3\text{HeT}^+$ are guided along the magnetic field lines and the turbomolecular pumps are ineffective in removing these ions. To address this problem, an electrode with a slightly more positive potential is installed at the exit of the DPS2-F. This does not hinder the movement of electrons, but reflects positive ions back towards the source [70]. To determine the composition of ions in the DPS2-F two Fourier Transform Ion Cyclotron Resonance (FT-ICR) traps [71] are installed at the entrance and exit.

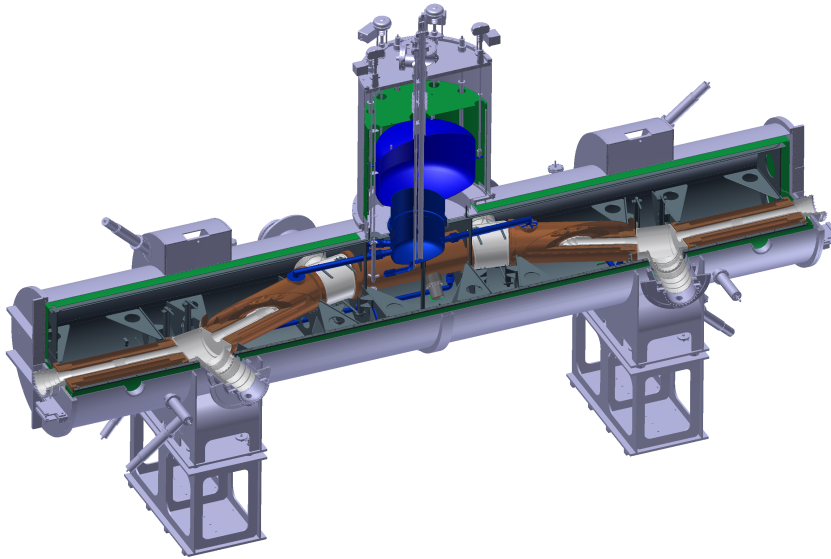


Figure 2.7:
Schematic
view of the
DPS2-F. This schematic shows the magnets (brown), the beam tube (silver) and the cryostat with its pump ports (dark grey). Note the bending of the beam tube which prevents neutral particles from streaming freely towards the spectrometer section.

Cryogenic Pumping Section

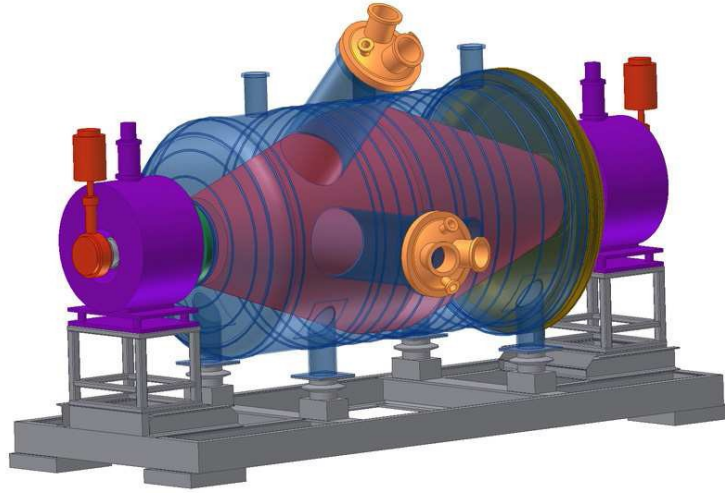
Beyond the DPS2-F, the tritium flow is so low that further differential pumping would be ineffective and another technique has to be applied. In the Cryogenic Pumping Section CPS, a part of the beam tube will be cooled with liquid helium to $T = 3 - 5$ K. At this temperature it is possible to freeze tritium onto the wall. To increase this effect, the beam tube will be coated with argon frost. Not only does this increase the surface significantly, but it also reduces contamination of the CPS, since the tritium will be frozen to the argon which can be flushed regularly, in contrast to the steel beam tube. Like the DPS2-F the CPS has a chicane and allows no direct line of sight from its entrance to the spectrometer region.

2.3.3 Electrostatic Spectrometers

The analysis of the kinetic energy of decay electrons is done by large electrostatic spectrometers working according to the MAC-E filter principle as explained in 2.2.1. Most electrons do not carry any information on the neutrino mass and would only crowd the main spectrometer. These electrons might scatter on residual gas molecules in the main spectrometer and ionize them. These positive ions would then be trapped and may again scatter and ionize further molecules, sending their electrons towards the detector. Or they might scatter with signal electrons and alter their energy. Any such scenario is not desirable. Therefore the electrons first enter the pre-spectrometer which operates on a fixed potential. Here, the bulk of the electrons, those with low energy, are already deflected. Of the 10^{11} electrons per second entering the pre-spectrometer only 10^3 will move on to the main spectrometer. There the flux will be reduced further by 5 orders of magnitude so that only 10^{-2} electrons per second hit the detector.

In addition, the pre-spectrometer served as a testing ground for technologies used at the main spectrometer, e.g. putting the vessel itself on high voltage, not only the electrode

Figure 2.8: The KATRIN pre-spectrometer: The vacuum vessel is shown in blue, the superconducting magnets that form the guiding field are shown in violet. The inner electrode system is shown in red and the support structure below the spectrometer is shown in grey.



system inside. This electrode system is able to shape the field and reduce inhomogeneities and also serves as a repellent against electrons ejected from the spectrometer hull by cosmic muons or natural radioactivity.

After passing the pre-spectrometer, the electrons in the endpoint region, which are of interest to KATRIN, enter the main spectrometer. There they are analysed with an energy resolution of $\Delta E = 0.93$ eV.

Situated in parallel to the main spectrometer is the monitor spectrometer. This is essentially the modified spectrometer from the Mainz experiment [12]. It will be connected to the main spectrometer high voltage and uses monoenergetic nuclear electron sources to measure fluctuations in the retarding potential of the main spectrometer. To minimize mutual influences on the respective magnetic fields, the monitor spectrometer is placed in a separate building.

Pre-spectrometer

The KATRIN pre-spectrometer is a cylindrical tank of 1.68 m inner diameter and 3.38 m length. The vessel is made of 10 mm stainless steel, and is closed on both sides by special flanges. Through these flanges, the inner electrode system is installed. Furthermore there are two cylindrical pump ports on the side of the spectrometer for a non-evaporable getter pump and ultra high vacuum (UHV) equipment. The entire vessel can be put on high voltage up to 35 kV and is fixed on ceramic insulators on a holding structure made of stainless steel. The heating/cooling circuit and the turbomolecular pumps are also insulated from the vessel by ceramic parts. The electrode system also rests on glass and ceramic insulators and can be put on a different high voltage than the vessel hull. With a slightly more negative potential than the hull, the wires repel electrons created on the inner surface and divert them from the inner volume. This is another measure against background, in addition to the magnetic field which guides those electrons back to the wall due to their gyration around the magnetic field lines. The use of a wire electrode to shield the spectrometer is a new design that was successfully tested at the pre-spectrometer test experiments. Figure 2.8 shows a schematic view of the pre-spectrometer.

The pre-spectrometer test experiments are finished, and the pre-spectrometer itself is set up in the KATRIN main experimental hall. In the neutrino mass measurement setup, it will cut off the low energy part of the spectrum which carries no information about the neutrino mass. But even before that it has been invaluable as a test setup for the inner electrode system principle, the vessel on high voltage, the heating/cooling system the detector system and data acquisition as well as the slow control. All these concepts have been evaluated and will find use at the main spectrometer.

Main-spectrometer

Beyond the pre-spectrometer is the KATRIN main spectrometer. In between these two components sits a single magnet which provides a guiding field for both MAC-E filters. Located on the other side of the 23.3 m long spectrometer is the pinch magnet with the maximal field of $B_{\text{max}} = 6$ T. It focuses the electrons onto the detector and determines the energy resolution and the acceptance angle of the MAC-E filter. The inner diameter of the main spectrometer is 9.8 m. The large size is required because the magnetic field decreases to $B_a = 0.3$ mT while having to accommodate the flux tube of 191 Tcm^2 . The need for adiabatic motion of the electrons dictates the length of the spectrometer. The transformation of transversal momentum to longitudinal momentum has to happen slowly to conserve the magnetic moment $\mu = \frac{E_{\perp}}{B}$. The energy resolution of the nominal setup is 0.93 eV. The pressure due to the ultra high vacuum setup of the spectrometer will be 10^{-11} mbar to minimize the probability of electrons scattering on residual gas molecules.

Like the pre-spectrometer, the main spectrometer is equipped with an inner electrode system. It is mounted on rails fastened to the steel hull and separated by ceramic insulators so that it can be set on a different potential than the hull. This allows for fine tuning of the analysing potential and shields against background electrons from the hull.

Since the magnetic field in the analysing plane is only $B_a = 0.3$ mT, it is necessary to compensate the earth's magnetic field. At $\approx 50 \mu\text{T}$ it amounts to $1/6$ th of the analysing field strength and cannot be neglected. For this purpose, a large air coil system has been installed in addition to an axial air coil system for adjusting the magnetic guiding field of the MAC-E filter. The commissioning of these systems was part of this work and is described in chapter 3.

Monitor Spectrometer

The retarding potential of the MAC-E filter has to be known with great precision to analyse the electron spectrum properly. A broadening of the analysed energy by a factor of σ^2 will lead to a systematic error in the observable neutrino mass squared of $\Delta m_{\nu}^2 = -2\sigma^2$. The design sensitivity of the experiment demands a 60 mV precision over a 3 year measurement period which translates to a 3 ppm stability at 18.6 kV. The effects of calibration uncertainties in KATRIN are discussed in [72].

In addition to a high precision voltage divider [73] and direct calibration of the main spectrometer with photoelectrons from $^{241}\text{Am/Co}$ or conversion electrons from $^{83\text{m}}\text{Kr}$, the high voltage of the main spectrometer will also be determined by the monitor

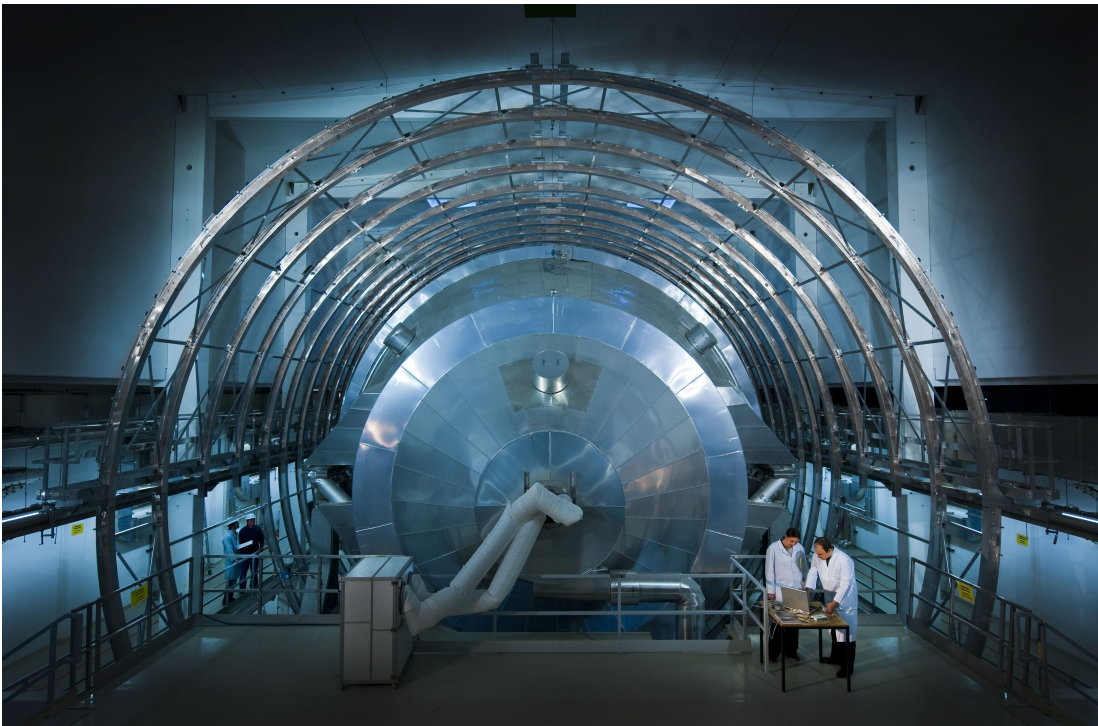


Figure 2.9: The KATRIN main spectrometer. The stainless steel vessel is covered by a thermal insulation which is held in place by aluminum sheets visible in the picture. The support structure for the air coil system is also shown. The pre-spectrometer will be connected to the flange where the air vent tubes exit the spectrometer.

spectrometer. The main advantage is that these measurements do not interfere with the main spectrometer operation.

The monitor spectrometer will be electrically connected to the main spectrometer and measure monoenergetic lines of nuclear sources. This allows for a direct and continuous high precision measurement of the high voltage used to analyse the tritium decay-electrons.

Since the pre-spectrometer test experiment was concluded and the pre-spectrometer is set up in the experimental hall, the monitor spectrometer has been used successfully to develop methods for actively removing stored particles. These test experiments include a magnetic pulse to break the storage condition, an electric dipole field to drift them out of the spectrometer and heating by electron cyclotron resonance to increase their energy until they escape the spectrometer to the wall. At least some of these methods will be implemented in the main spectrometer setup to lower the background count rate caused by stored particles.

2.3.4 Focal Plane Detector

The focal plane detector system is attached to the main spectrometer. The detector itself is a monolithic segmented silicon PIN diode. It detects the electrons transmitted by the main spectrometer with an efficiency of $> 90\%$. Since the electric and magnetic fields in the analysing plane are not completely homogeneous, as figure 2.11 shows, the detector is split into 148 pixel. Each pixel has the same area and they are arranged in 12 concentric rings, each divided into 12 pixels, except for the central circle which is divided into 4 pixels. Figure 2.10 shows the layout of the detector. The segmentation leads to much smaller inhomogeneities dB/dr and dU/dr as opposed to a single pixel covering the whole area. Each pixel will measure a separate β spectrum with its own retarding potential and magnetic field. The combination of all pixels will then be used for the neutrino mass analysis.

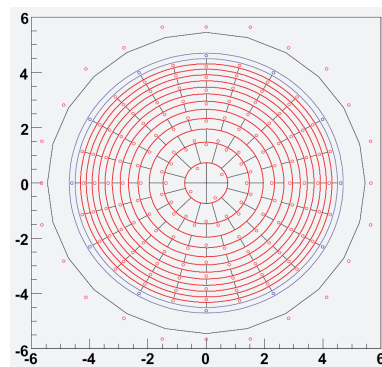


Figure 2.10: Layout of the KATRIN focal plane detector

2.4 Demands on the Magnetic Field in the Main Spectrometer

Along the whole KATRIN setup, electrons are guided by magnetic fields that vary in strength over 5 orders of magnitude. It is imperative that the electron transport is adiabatic in spite of electric and magnetic gradients. This is achieved by the size of the apparatus which allows for the field strength changes to be spread over a large distance. Especially great care has been taken to design the magnetic field in the main spectrometer. Since the electric potential is essentially homogeneous along the cylindrical part of the spectrometer, the magnetic field has to ensure the transmission condition (2.11). It is also important for reducing background from the spectrometer hull by a factor of 10^5 in addition to the electrode system.

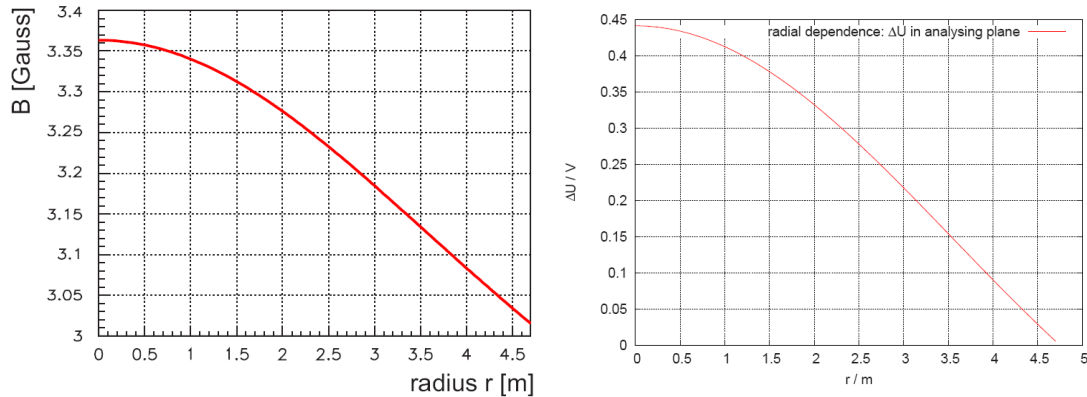


Figure 2.11: Design field strengths in the analysing plane: The left plot shows the radial inhomogeneity of the magnetic field in the analysing plane, the right plot shows the equivalent for the electric potential. The detector is segmented to limit ΔB and ΔU for each pixel.

2.4.1 Transmission Properties

To optimize the transmission properties of the spectrometer it is of advantage to have a smooth transition in the magnetic field as well as the smallest possible radial inhomogeneity. The axial air coil system is the ideal tool to adjust the field in the axial direction. It also increases the radial homogeneity since its field is strongest near the coils and weakest in the center as opposed to the solenoid field which is strongest in the center. The superposition of both fields shows a better homogeneity than each field alone. Axial symmetry is also desirable as electrons are guided to the detector and the risk to connect the vessel hull with magnetic field lines to the source or the detector is minimized. Such an effect might be introduced by the earth's magnetic field which is compensated by another air coil system at the main spectrometer. Both air coil systems will be discussed in chapter 3.

2.4.2 Background Reduction

Axial symmetry is also a crucial factor in guiding electrons from the spectrometer hull back out of the spectrometer volume. An axially inhomogeneous magnetic field might guide electrons away from the wall into the spectrometer where they might be stored and cause further background or move directly onto the detector itself. Besides the earth's magnetic field the air coil systems themselves introduce a small inhomogeneity due to their technical realisation as discrete wires. In addition, the walls of the experimental hall are reinforced with a limited amount of steel which also introduces an inhomogeneous field of a few μT in the main spectrometer. These effects are small but have to be studied and understood nonetheless. Further discussion of the inhomogeneities, their sources and effects can be found in chapters 5 and 6.

3. The Air Coil Systems at the KATRIN Main Spectrometer

The magnetic guiding field in the KATRIN experiment is mainly provided by superconducting magnets. As explained in 2.2.1, the field strength in the analysing plane drops to $1/20000$ th of the maximum field value to give the high energy resolution of the spectrometer. The very low field strength makes the MAC-E filter setup susceptible to outside disturbances of the magnetic field. At 0.3 mT, the earth's magnetic field is not negligible and disturbs the electrons trajectories. It is also important that the field does not drop to quickly along the beam axis, the solenoid field itself drops rather quickly with $1/r^3$ and measures to ensure the transmission condition 2.11 need to be taken. The tools for this task are the two air coil systems specifically designed and built around the KATRIN main spectrometer. The **Earth's Magnetic field Compensation System** (EMCS) compensates the geomagnetic field at the main spectrometer site and the **Low Field Coil System** (LFCS) is able to influence the magnetic field in the axial direction of the main spectrometer [74] [75]. Much design work and preliminary measurements have also been done in [76]. Commissioning has been done in this work and in [77], a diploma thesis supervised in the scope of this work.

3.1 Motivation of the Air Coil Systems

In order to optimize the transmission properties of the main spectrometer, the magnetic guiding field needs to meet certain criteria:

The magnetic flux tube, the region defined by the source diameter and magnetic field, of 191 Tcm^2 must not touch the spectrometer wall and also not come close to the inner electrode system. If the field lines crossed the vessel hull, electrons from tritium decay emitted at large distances from the beam line center would collide with the wall and not reach the detector. Furthermore, electrons emitted from the hull by cosmic muons or natural radioactivity would directly be guided onto the detector. This would reduce the real signal rate and might introduce a significant increase in background. Figure 3.1 illustrates the problem.

The region near the inner electrode system is defined by its near field, unlike the inner volume of the spectrometer. At these close distances, the discreteness of the wires would form local minima and maxima in the electrostatic potential. This is a configuration suited for trapping charged particles and might also violate the transmission condition.

Fulfilling the transmission condition means that:

- an electron with a starting energy $E < qU_a$ lower than the transmission energy is reflected.

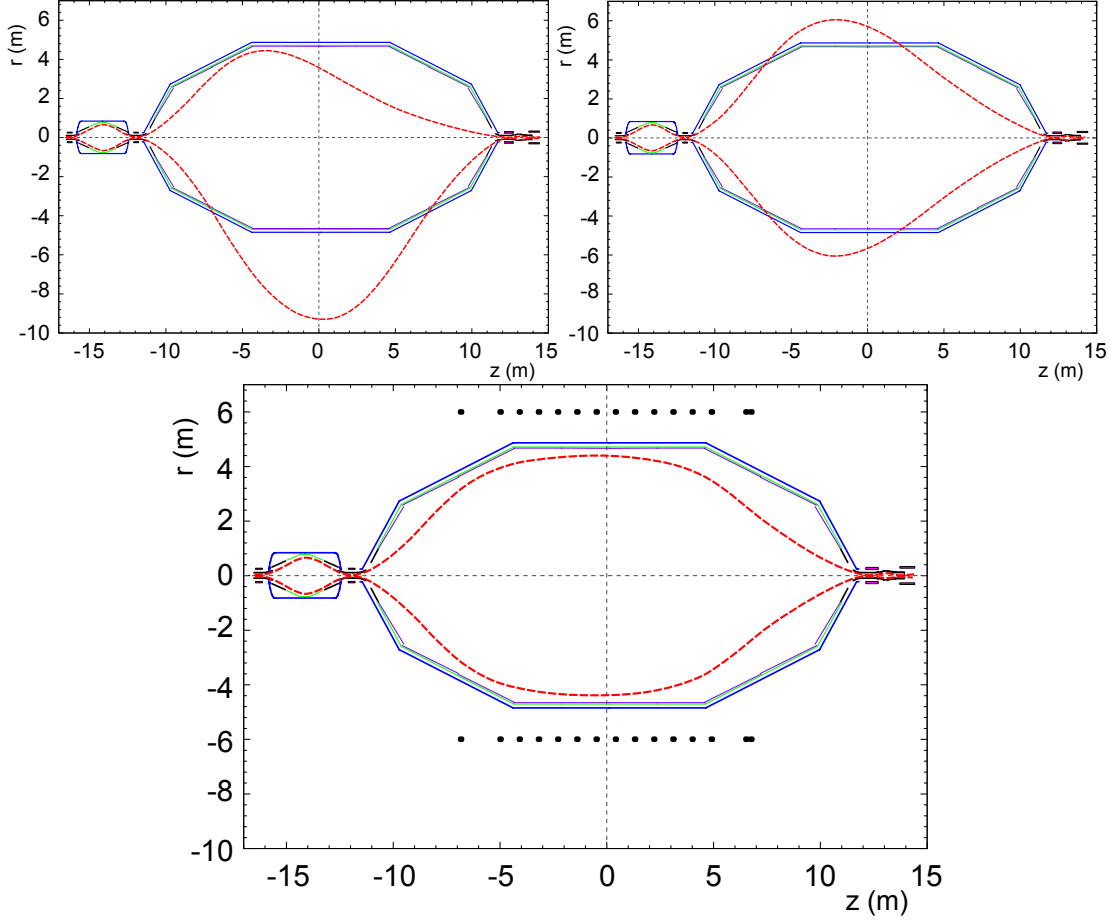


Figure 3.1: Magnetic flux tube in the KATRIN spectrometers for different configurations: The walls of the main and pre spectrometer are drawn in dark blue, the inner electrode system is light blue. Superconducting magnets are indicated by red bars. The dashed line shows the flux tube of 191 T cm^2 . **top left:** Here the field is only composed of the solenoid field and the earth's magnetic field. **top right:** The magnetic solenoid field with the earth's magnetic field compensated. **bottom:** The superconducting solenoids, EMCS and LFCS combined shape the field into its desired form.

- an electron with a starting energy $E > qU_a$ higher than the transmission energy is transmitted.
- an electron with a starting energy $E = qU_a$ equal to the transmission energy has a longitudinal energy $E_{\parallel} = 0$ only in the analysing plane and positive longitudinal energy everywhere else.

The last point is critical since this would mean that there are multiple turning points instead of one analysing plane and the electric potential in all these points would have to be considered.

The magnetic field needs to be as homogeneous as possible to minimize dB/dr over one detector pixel. This is crucial since an uncertainty in the magnetic field translates into a worsening of the energy resolution ΔE of the spectrometer.

For background reduction through magnetic shielding, it is important that the field is axially symmetric. The equation of motion of a charged particle in an electromagnetic field

$$m\ddot{\vec{r}} = q\dot{\vec{r}} \times \vec{B}(\vec{r}, t) + q\vec{E}(\vec{r}, t) \quad (3.1)$$

in the adiabatic approximation and perpendicular to the magnetic field yields terms proportional to $\vec{E} \times \vec{B}$ and $\vec{B} \times \nabla \vec{B}$ [73]. If the field is perfectly axially symmetric, this only leads to a circular motion around the flux tube, but if the symmetry is broken these terms would lead to particles entering the inner volume of the spectrometer and hitting the detector. This leads inevitably to an increase in background.

The stronger the field is, the better the magnetic shielding works. On the other hand, a good energy resolution is achieved by a low minimal field. The possibility to vary the field strength and find a compromise between shielding and energy resolution is crucial.

To address these points the air coil systems of the main spectrometer have been designed as flexible as possible with separately powered x- and y-direction compensation systems of the EMCS and individually powered coils in the LFCS.

3.2 Electromagnetic Design

In order to fulfill all these requirements, great care has been taken to design the air coil systems as flexible as possible. In this section the general design criteria will be discussed.

3.2.1 Low Field Coil System

The current of each coil in the LFCS can be set individually to be able to fine-tune the magnetic field in the spectrometer as well as determining the final strength of the analysing field. As discussed above, the LFCS has to ensure that the flux tube does not come near the electrodes and the vessel hull. It also allows to weigh the field strength between energy resolution and magnetic shielding. It is also possible to improve the radial homogeneity of the field in the analysing plane. But above all, the transmission condition has to be satisfied.

The wire electrode of the KATRIN main spectrometer is designed in a way that all electrodes in the cylindrical part are on the same high voltage. This results in a homogeneous potential along the beam axis, which cannot guarantee the transmission condition. Slight disturbances in the potential could violate the transmission condition and cause the longitudinal energy to drop to zero outside the analysing plane. To avoid this risk, a magnetic field with one global minimum also has to be very homogeneous along the beam axis. Such a setup is shown in figure 3.2.

To counter this effect, a magnetic field with local minima before and after the analysing plane can be applied. In this configuration, small fluctuations in the retarding potential would not be dangerous, since the longitudinal energy of the electron has been increased due to the gradient towards a lower field strength. Close to the analysing plane, the field

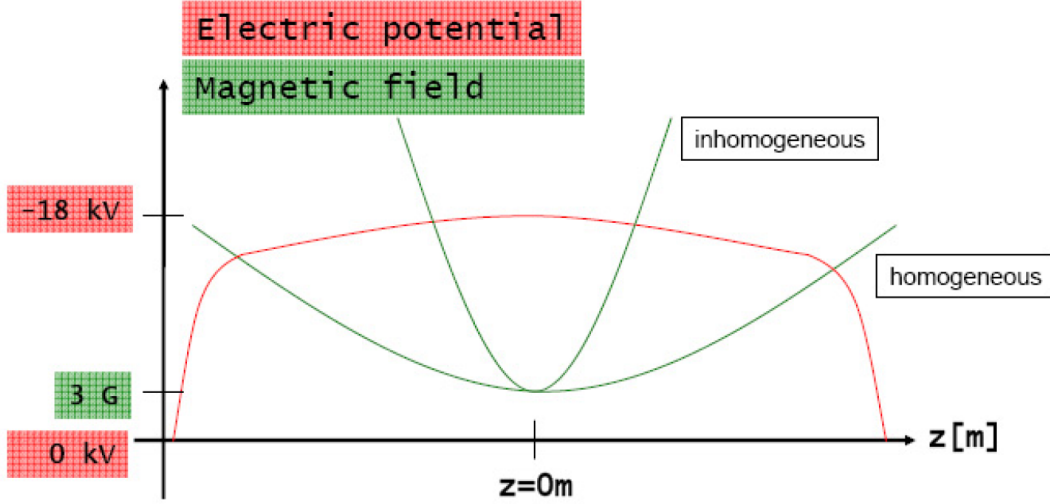


Figure 3.2: Magnetic field configuration with one global minimum: The electric potential is very homogeneous along the z-axis. In order not to violate the transmission condition, the magnetic field has to be homogeneous as well since small disturbances in the potential could lead to reflection of electrons.

strength increases again and electrons with an energy below the transmission energy will still be reflected. The longitudinal energy of the electron can be expressed as:

$$E_{\parallel} = E_s - E \cdot \frac{|\vec{B}|}{|\vec{B}_s|} + q(U_s - U) \quad (3.2)$$

The larger the term $\frac{|\vec{B}|}{|\vec{B}_s|}$ gets, the smaller the longitudinal energy of the electron is. A local magnetic field maximum at $z = 0$ will then be the point of minimal longitudinal energy when the electric potential U is homogeneous. So the magnetic field serves as an energy discriminator. Such a situation is shown in figure 3.3 In this configuration the radial inhomogeneities of the magnetic field in the analysing plane would also be lower. Figure 3.4 compares the global minimum situation with the local minima setup.

The two minima setup is favourable with respect to the transmission condition, but since the magnetic field is generally lower in some regions, the magnetic shielding is weaker. In addition to that, a local magnetic field minimum is a trapping region for charged particles which might increase background. It is yet unclear, which field setup provides the best results, and the final decision has to be made based on test experiments. But with a flexible LFCS, both solutions are equally viable. A detailed discussion of the issue can be found in appendix A of [63] and in [75].

3.2.2 Earth Magnetic Field Compensation System

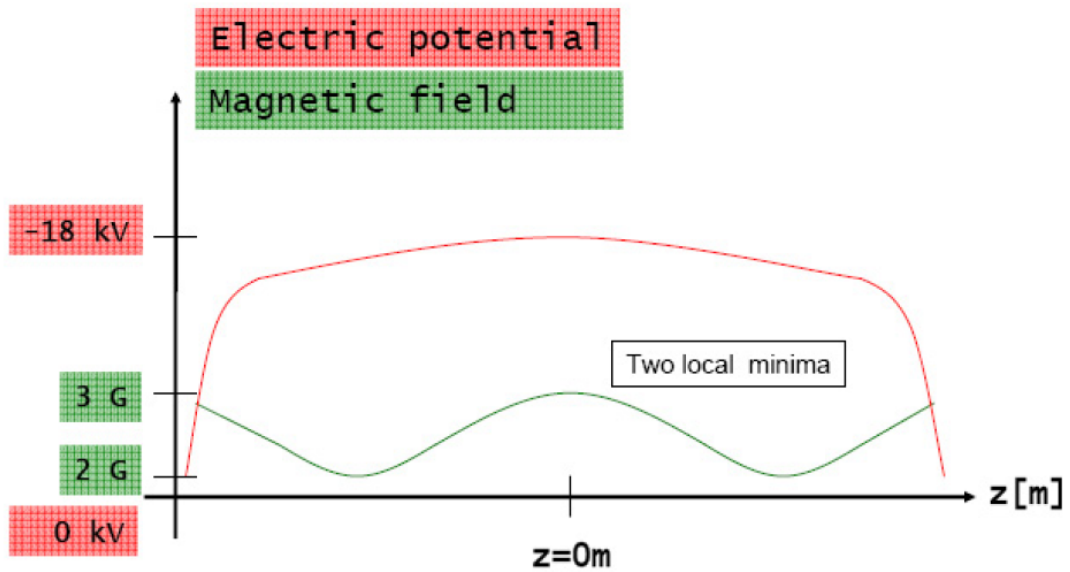


Figure 3.3: Magnetic field configuration with two local minima: The electric potential is the same as in 3.2, but the magnetic field shows two local minima which ensures the transmission condition is satisfied.

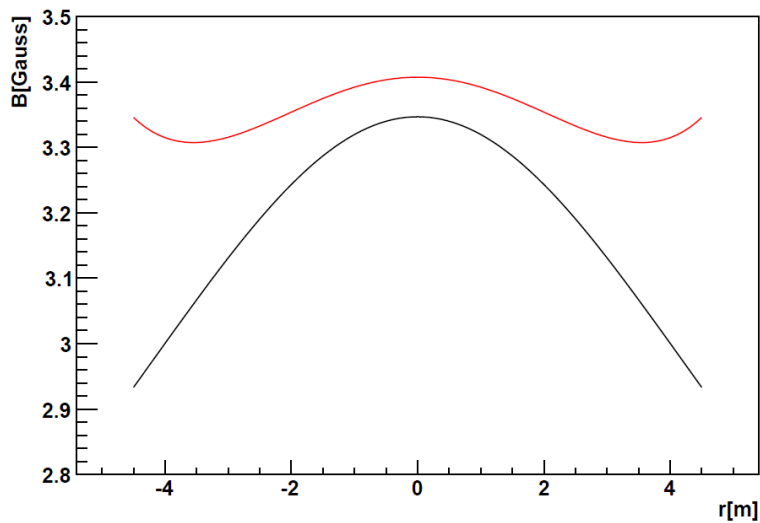


Figure 3.4: Radial homogeneity of the magnetic field in the analysing plane: The black curve shows the radial field dependence in a global minimum configuration, the red curve shows the same with two local minima before and after the analysing plane.

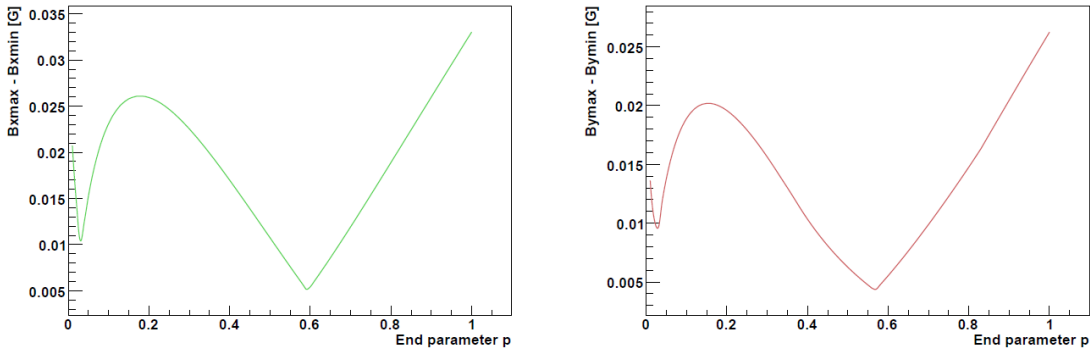


Figure 3.6: Influence of the end parameter on field homogeneity: The plots show the maximal differences in absolute field on a circle of $r = 4.5$ m with varied end parameters p . The right plot shows the field inhomogeneity in the x-direction and the left in y-direction. Both for a coil system designed to produce a field in y-direction. A value of $p \approx 0.6$ gives the best result and has been chosen for the KATRIN EMCS.

For compensating the earth's magnetic field, a very homogeneous field is needed. A coil system as first proposed in [78] provides such a field: A $\cos(\Theta)$ current distribution on a spherical surface produces a very homogeneous field in the volume. This was later generalized to ellipsoidal coil geometries in [79]. This approach also works for an infinitely long ellipsoid, a cylinder. At the KATRIN main spectrometer, this concept has been applied to compensate two components of the earth's magnetic field, the y- and x-component. The z-component is taken into consideration with the LFCS and solenoid fields. The ellipsoid geometry has been approximated by a 24 m long cylindrical setup. This is sufficiently long that the field in the central region is still very homogeneous. Two separate perpendicular systems provide fields in x- and y-direction. Despite the coils not being elliptical in shape, in the central part of the spectrometer where the field influence is greatest, the homogeneity is very good, even at outer radii, see figure 3.7. The $\cos(\Theta)$ current distribution is approximated by placing the wires on the intersections of equidistant planes with a circle as shown in figure 3.5. The number of loops fixes the distance between the planes, but the distance to the bottom of the circle is a free parameter and affects the homogeneity of the system as shown in figure 3.6. The inhomogeneities are largest at large radii as there the fields of individual wires becomes visible.

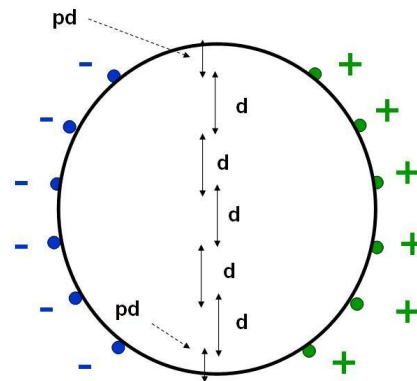


Figure 3.5: Schematic of a cosine coil design: This sketch shows the current loops in equal distances d . The distance of the lowermost current loop to the bottom of the circle is determined by the end parameter $p \cdot d$ with $p < 1$.

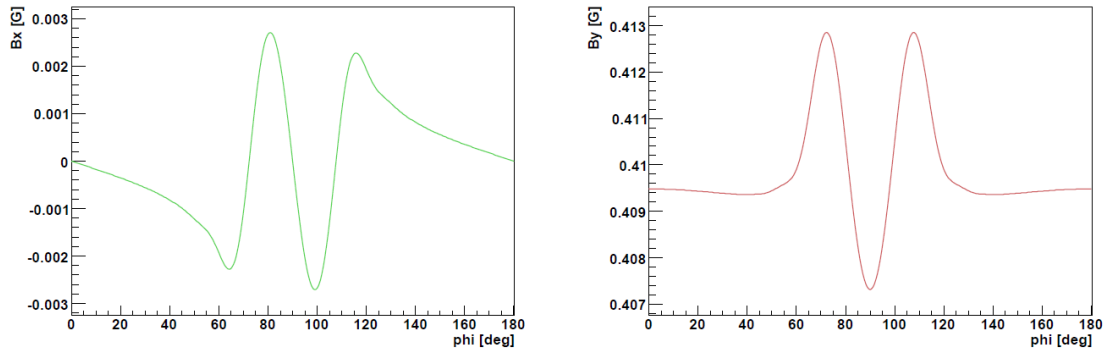


Figure 3.7: Azimuthal field fluctuations of a cosine coil system: The plots show the field produced by a cosine coil system in y-direction on a half circle in the analysing plane with $r = 4.5$ m. This design is with an optimized end parameter. **left:** Field in x-direction. **right:** Field in y-direction.

3.3 Technical Realisation

The KATRIN air coil system needs to be a powerful and flexible tool for adjusting magnetic fields in the main spectrometer. During day-to-day measurements the air coils have to provide a variety of field strengths, depending on the desired field configuration. In the testing and commissioning phase of the main spectrometer they need to fulfill an even broader role. They have to compensate for not yet installed magnetic components as well as provide exotic field configurations for specific measurements.

3.3.1 Electrical Layout

For the guiding field, the co-axial LFCS needs to include 14 separate coils where the first 13 have to deliver 0 – 500 ampere turns and the last coil 0 – 2000 ampere turns. To compensate the earth’s magnetic field, we need 16 turns at approximately 47 A for the vertical component and 10 turns at 15 A for the horizontal component. These will be implemented in two perpendicular cosine coil systems. This configuration provides a very homogeneous field inside the volume of the wiring. For test measurements, the flux tube may be shifted up to ± 0.5 m, therefore the EMCS has to offer the possibility to deliver 47 ± 25 A or 15 ± 44 A respectively.

In this range of settings a balance of conductor material and electricity cost has been aimed for. As conductor material, a 70 mm^2 cross section aluminum cable was chosen since it is lighter than copper. The reduced weight lowers the costs for the support structure which compensates for the higher power consumption.

Each coil is powered by a SM3000 Series Delta Elektronika Power supply. This allows for more flexibility in adjusting the magnetic fields.

3.3.2 Support Structure

The cables which form the EMCS and LFCS are supported by a mechanical structure made from aluminium and stainless steel for optimal magnetic properties. This structure carries the cables and defines their positions as required by the electromagnetic

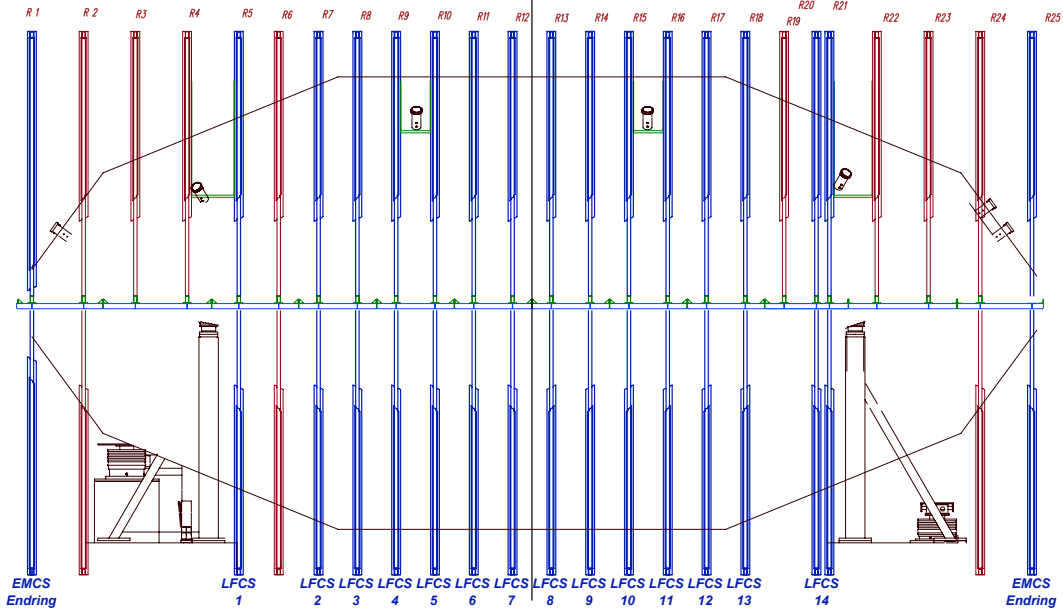


Figure 3.8: Overview of the KATRIN Main spectrometer and the LFCS air coils. The figure shows the aluminum rings of the support structure. Rings instrumented with cables are shown in blue, they are marked with their respective numbers below. The end rings of the EMCS are also shown, but not the cables along the cylindrical part of the cosine coils. The red numbers above the coils identify the corresponding mechanical support structure rings.

design. The main elements of the support structure are 25 rings which define the geometry. Each ring consists of 12 sections made from rectangular aluminium profiles bent to an outer radius of 6300 mm, the inner radius is 6160 mm. The profiles cross section is 80 mm · 140 mm with a wall thickness of 4 mm. Mechanical stiffness is achieved by 24 u-shaped transverse aluminium girders of 50 mm · 50 mm · 3 mm per ring. To each ring an inner and outer belt of 5 mm aluminium sheet is welded. The 205 mm wide outer belt carries combs holding the cables, the inner belt of 140 mm width is reserved for attaching equipment like magnetic field sensors. The whole structure is supported on rails mounted to the support pillars of the main spectrometer building. Figure 3.8 shows an overview of the KATRIN main spectrometer and the LFCS air coils.

3.3.3 Mechanical Layout

The coil windings consist of single conductor aluminium cables with 70 mm² cross section and a 14 mm² radius. LFCS coils 1,2,12 and 13 have 14 windings, LFCS coil 14 has 28 windings and two support rings to accommodate the additional cable. All other LFCS coils consist of 8 windings. The LFCS cables are held in place by combs attached to the outer belt approximately 1 m apart on the circumference. These Combs define a layer of 2 · 4 cables which are held by a clamping bar.

The horizontal parts of the EMCS cables are running across the rings through aluminium pipes with 40 mm diameter. These pipes are fixed to each ring they cross by clamps. The inner diameter of these pipes allows for a deviation of up to 11 mm from

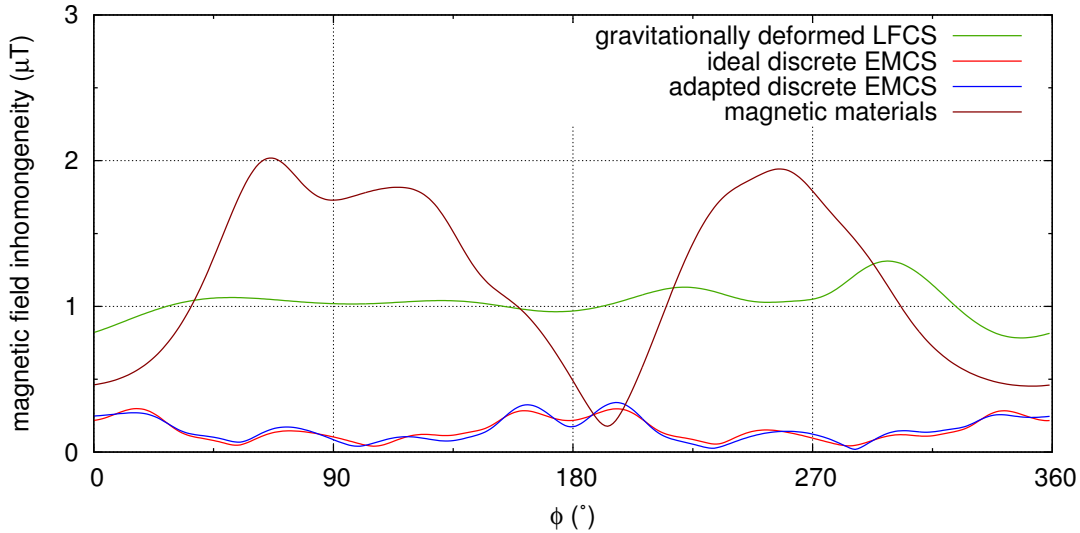


Figure 3.9: Comparison of magnetic field inhomogeneities. The plot shows the inhomogeneities in the analysing plane in a circle with radius $r = 4.5$ m. 0° is the top of the spectrometer and the values are ordered counter-clockwise, so 90° is in positive x-direction. The additional inhomogeneities introduced by the gravitational deformation of the LFCS are shown in green. The ideal (red) and adapted (green) EMCS systems show no large differences, so the change in wiring of the EMCS is not problematic. The field of the magnetic materials is shown in brown for comparison.

the reference position of the cables. The vertical correction system has $2 \cdot 8$ loops with constant spacing $\Delta y = 0.74$ m between two loops and $0.6 \cdot \Delta y$ between the first loop and the bottom and the last loop and the top of the system. The horizontal system is built in a similar fashion with $2 \cdot 5$ loops and a spacing $\Delta x = 1.14$ m.

Gravitational Deformation and Correction

Due to the weight of the support structure, it deforms under its own weight so that the actual radial positions of the cables deviate from their reference position up to ± 5 cm in extreme cases. Most of the air coil system is within its design specification of ± 3 cm at a 10 m radius. The actual positions of the cables have been measured with ± 5 mm accuracy and negative deviations from the reference radius have been corrected by wooden spacers.

The design cable paths of the EMCS collide with the support pillars of the main spectrometer. In these regions, alternative layouts have been designed and simulated. The solution which introduces the least variation from the design field has been chosen. Figure 3.9 compares these changes to those introduced by the gravitational deformation and the intrinsic inhomogeneities of the EMCS.

These variations are small effects, but will nonetheless be represented by the field simulations. Since the KATRIN focal plane detector is segmented, every part of the analysing plane is mapped separately and has to be analysed with its respective corresponding magnetic fields and electric potentials. Since this is the case, these small deviations

do not influence the energy resolution of the main spectrometer. For analysis, these fields have to be reproduced reliably by simulations, since no further measurements inside the vacuum vessel are possible. This means that the field sources need to be well understood and analysed in detail.

3.4 Commissioning of the Air Coil Systems

In the scope of this work, precise magnetic field measurements have been done inside the spectrometer with a very high spatial and directional resolution made possible by a cooperation with the Geodesic Institute of KIT. Along with these magnetic field measurements, detailed geometry data about the air coil systems was used to simulate the magnetic fields at the positions at which they were measured to ensure that the simulations represent the fields correctly within 1 % accuracy or better. Since the KATRIN experiment has to rely on field simulations for analysis, this confirmation is a very important step towards the analysis of neutrino mass data.

3.4.1 Measurements Inside the Main Spectrometer

The most interesting part with respect to magnetic field simulation requirements is the central volume of the main spectrometer, since the field will be weakest there. So a deviation of the simulated field from the actual field will have largest effects here.

Measurement Procedure

During the installation phase of the inner electrode system, access to the main spectrometer volume was made possible by the intervention system, a specially developed aluminium scaffolding. The intervention system included a platform with variable height and position along the spectrometer axis. With this system it was possible to cover a large volume of the central main spectrometer with only minimal disturbances due to permanently magnetized material in the vicinity of the sensor. The intervention system has been dismantled, after the electrode installation was completed, so no further measurements inside the spectrometer were possible.

Unfortunately, there was no way to determine the exact currents in the air coils aside from the display on the power supplies with a 1 A accuracy for the LFCS and 0.1 A for the EMCS. A direct and independent measurement of the currents was possible five months after the magnetic field measurements with a DC/DC converter. The position and orientation of the magnetometer has been mounted in a special holding structure shown in figure 3.10. The aluminum structure was designed to hold the magnetometer and four reflector spheres for the laser tracker. The magnetometer has been referenced to the position of the reflector spheres whose position in the main spectrometer were measured. This setup allowed for a reconstruction of the orientation of the magnetometer axes with a precision of $0.1^\circ - 0.2^\circ$.

With this setup it was possible to take magnetic field values with precise position and orientation information at 46 points in the equatorial plane of the main spectrometer. At each of these points, the LFCS coils were set to 0, 30 A and 60 A individually and collectively. The EMCS in y-direction was set to 0 and 50 A, the x-direction EMCS to 0 and 15 A. The positions are shown in figure 3.11

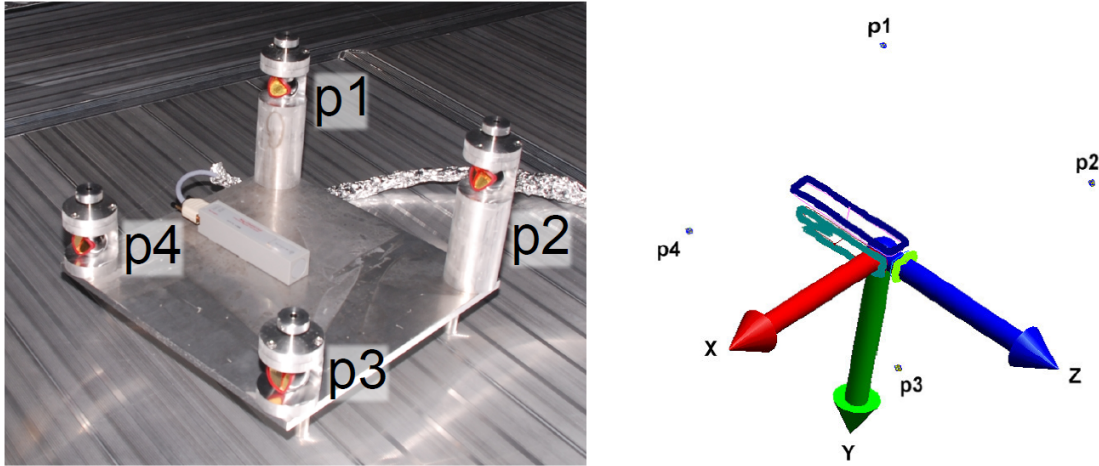


Figure 3.10: Holding structure used of the magnetometer during measurements in the main spectrometer. **left:** Shown here is the fluxgate magnetometer on the aluminium structure during calibration. Nested inside the four aluminum cylinders are reflector spheres for the laser tracker to which the magnetometer has been referenced. With this construction an angle resolution of 0.1° was possible. Spatial resolution is limited by the arrangement of sensor element in the magnetometer to 15 mm. **right:** The calibration measurement connecting the magnetometer reference frame to the four reflector points [80].

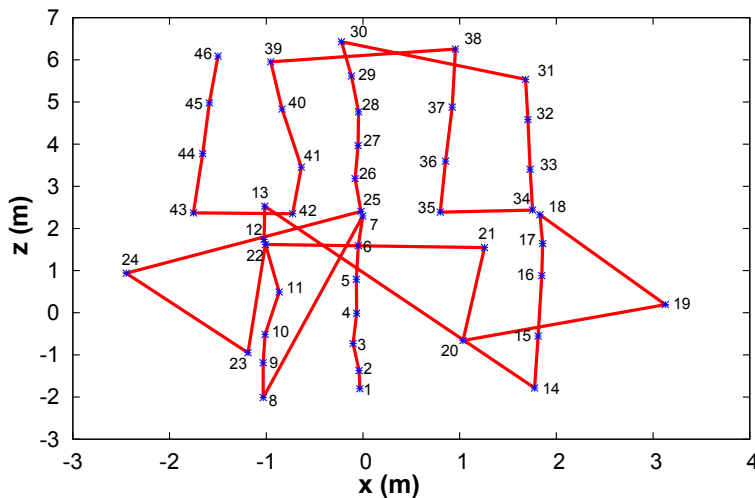


Figure 3.11: Positions of magnetic field measurements in the main spectrometer: The blue points mark the positions, where magnetic field values were taken. The red lines along with the numbers indicate the order in which the measurements were done. The analysing plane is at $z = 0$, all values were taken at $y = -0.4$ m

Comparison with Simulations

The magnetic field measurements were done with and without current in the coils. Then the background field was subtracted vectorially from the measurements with current, so that only the magnetic field of the air coils remains.

The magnetic field simulations shown in this sections were done with the currents taken during the magnetic field measurement from the power supply displays as well as with the more accurate values obtained with a current transformer five months later. The manufacturer Delta Elektronika claims the maximum drift of the power supplies over five months is 0.3 A [81]. This corresponds to a maximum 1 % – 0.5 % error depending on the current. Despite this systematical uncertainty, this improves the current measurement with respect to the power supply display by 1 order of magnitude or more for the LFCS coils. The EMCS power supply display is accurate to 0.1 A, here the DC/DC converter does not improve the current measurement by much, but as can be seen in figure 3.13 both values are in excellent agreement.

These simulated magnetic field values can be compared directly to the measured values. Figure 3.12 shows simulated and measured values with all LFCS coils simultaneously at 30 A (a) and 60 A (b). On the y-axis, the absolute magnetic field strength is shown over the measurement position on the x-axis. The position numbers correspond to those in figure 3.11. The red crosses are measured field values with their statistical error bars coming from averaging over 1000 measurements. Simulated field values with currents from the power supply display are shown in blue diagonal crosses. Their error bars are a direct result of the inaccuracy of the digital display. The black stars show simulated magnetic field values with currents from the DC/DC converter. The errors on this magnetic field is also a direct result of the uncertainty in the current measurement. In both cases, the simulations with the DC/DC converter currents provide a better agreement with the measured values. Although they do not agree within their respective error bars, the values still fit together very well. In both cases, the simulated values are systematically lower than the measured ones. This is most probably due to a drift in the 14 power supplies providing current for the LFCS coils. As discussed above, such a drift is well within the specifications of the power supplies. It can easily be avoided by calibrating the power supplies in regular intervals or monitoring the currents continuously in an independent way.

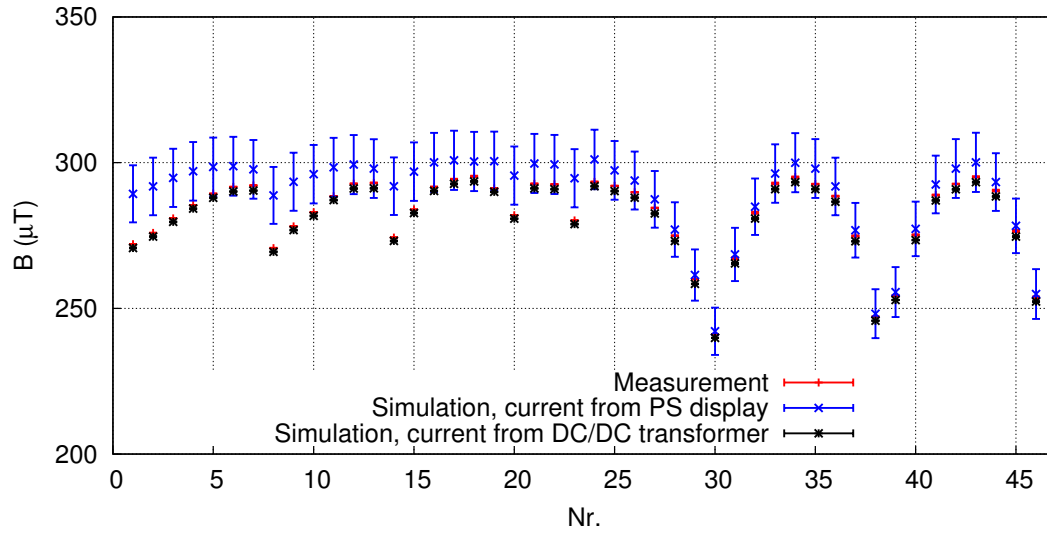
Figure 3.13 is a similar display for the EMCS data. Again, the red crosses are measured absolute magnetic field strengths, the blue diagonal crosses simulations with currents from the display and the black stars simulations with currents from the DC/DC converter. Due to the lower absolute field value, the simulated fields match the measured values within the experimental errors, although the relative accuracy is not significantly better than for the LFCS. Still, this result shows that the EMCS is very well understood. Even though measurement and simulation agree within their errors, the best simulation values are still systematically lower than the measured mean values as in the LFCS data.

In contrast to the absolute values, the relative deviations of simulated and measured values are shown in the histograms 3.14 and 3.15. The inlays show the direction of

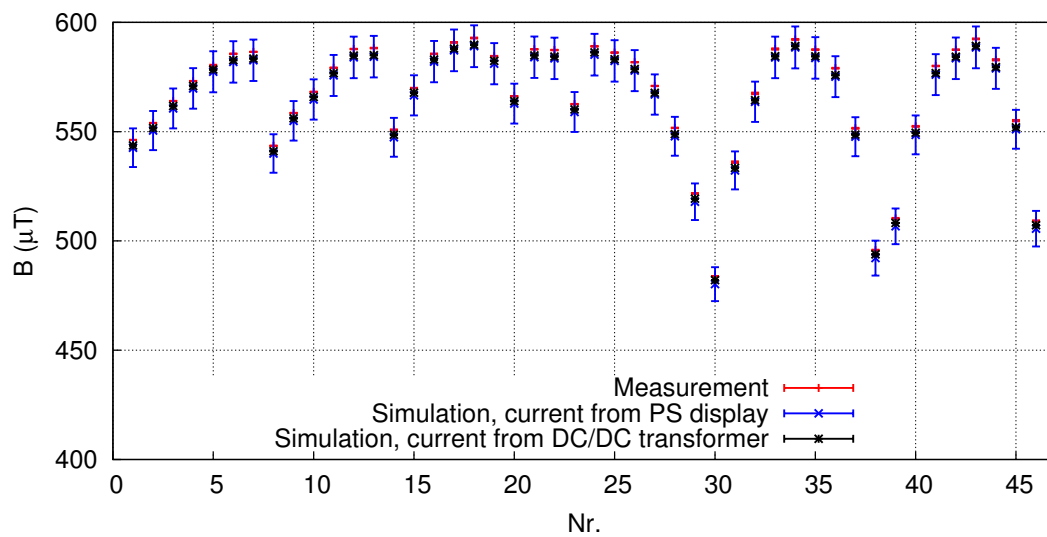
the field that was measured, in figure 3.14 this is the LFCS system at 30 A and 60 A. The histogram shows all measured field values with single LFCS coils, which means 14 measurements at each position. The data nicely show that the simulations represent the actual situation inside the main spectrometer to well below 1 % precision for both current settings. Also, the lower field values are only slightly less accurate than the 60 A data. This means that the reached accuracy is not a case of a small systematic error, but rather that the whole system is well represented in the magnetic field simulations.

In figure 3.15 magnetic field data and simulation comparisons for the EMCS in both directions are shown. (a) shows the vertical y-component correction system and (b) the x-component. Again, the relative differences between simulation and measurement are in the 0.1 % region for both systems. As discussed in 3.13 this is as good as it gets for the EMCS since the simulation data points are within the experimental error bars.

Figures 3.12 to 3.15 only show information about the absolute field strength. To address the directional deviations of the simulations from the measured data, figures 3.16 and 3.17 show the angular difference of the same data as 3.14 and 3.15. For the LFCS as well as the EMCS, the deviations are at the limit of the calibration accuracy of 0.1 %. Again, the deviations do not depend as strongly on the air coil current to suggest a systematic connection. The only factor is the systematic uncertainty introduced by the calibration. The most probable reason that the deviation in the y-direction EMCS data is lower is that the reflector point spread is larger in the x-z-plane the deviations on the y-direction.

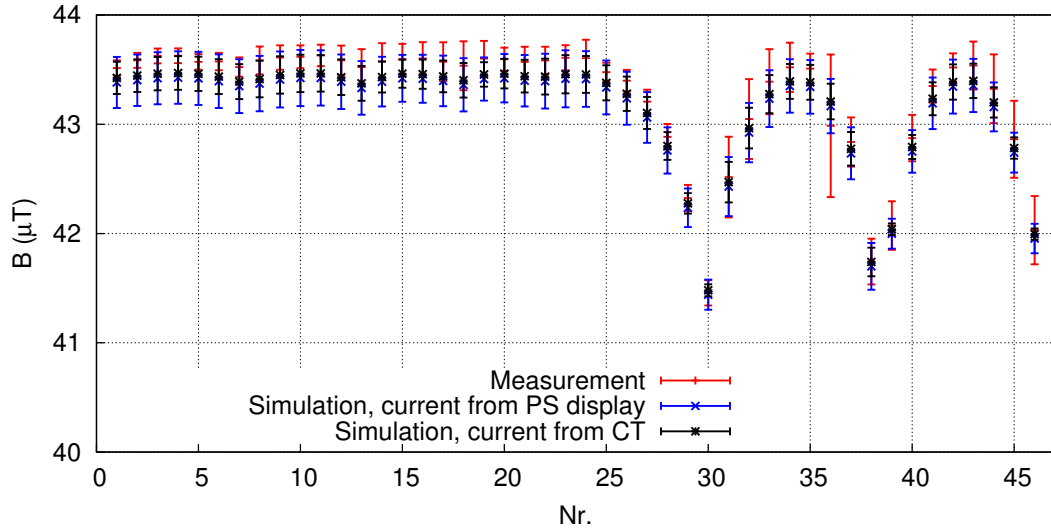


(a)

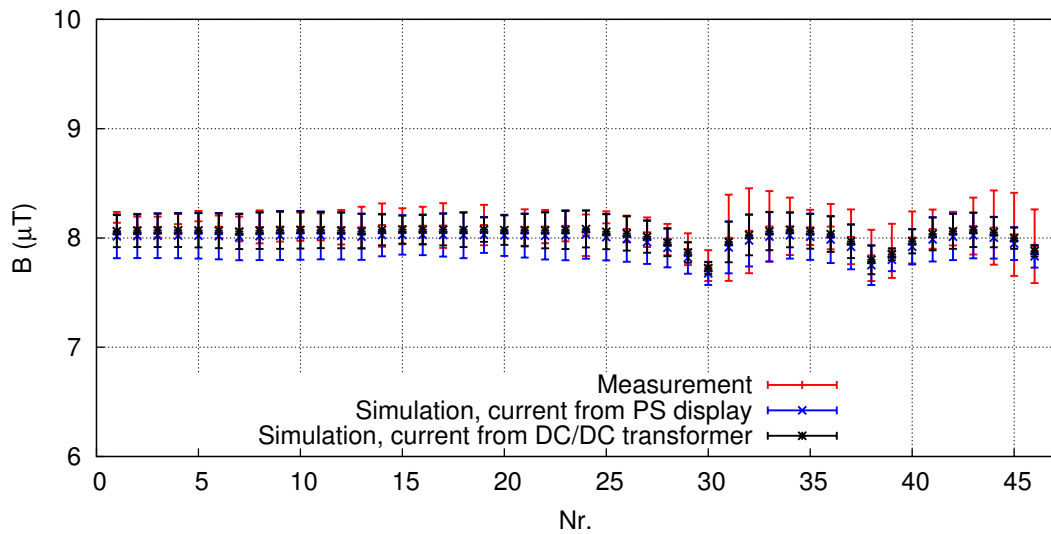


(b)

Figure 3.12: Comparison of measured and simulated magnetic LFCS fields in the main spectrometer. The plots show the measured field values taken at the positions shown in figure 3.11 with the experimental error bars in red. These errors are in the order of 10 nT and are not resolved in the figures. The simulated field values are shown in blue with currents from the power supply display and black with currents from the DC/DC converter. The error bars in the simulation are a direct propagation of the error on the currents. (a) shows all LFCS coils simultaneously at 30 A, (b) the same at 60 A. Although the black simulation values with the current transformer currents do not match the simulation within the error bars, the agreement between measurement and simulation is better than 1 % as shown in figure 3.14.

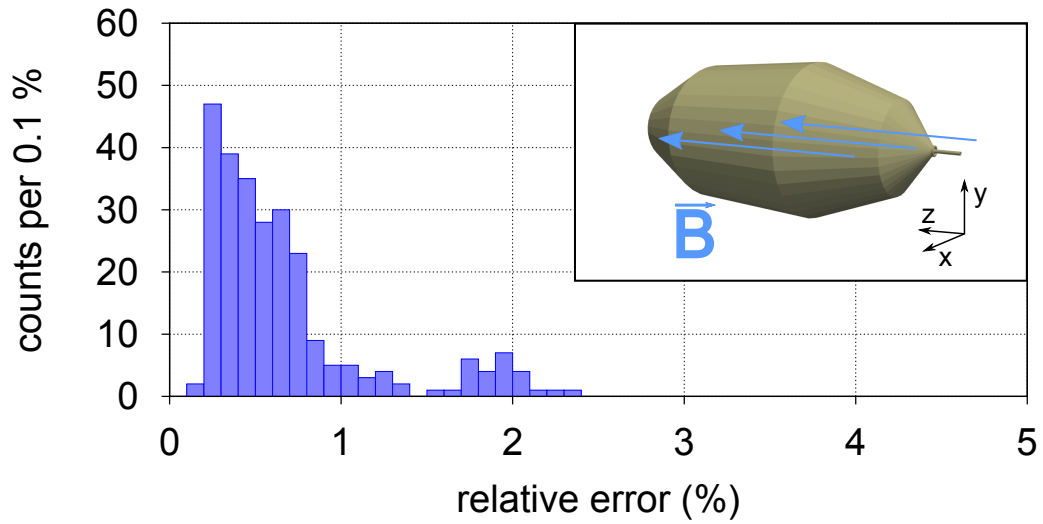


(a)

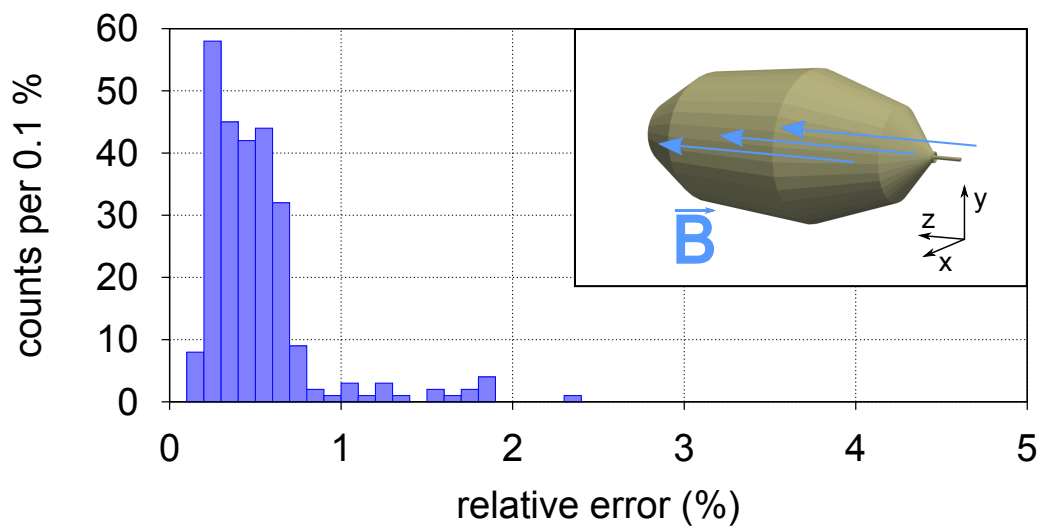


(b)

Figure 3.13: Comparison of measured and simulated magnetic EMCS fields in the main spectrometer. The plots show the measured field values taken at the positions shown in figure 3.11 with the experimental error bars in red. These errors are in the order of 10 nT and are not resolved in the figures. The simulated field values are shown in blue with currents from the power supply display and black with currents from the DC/DC transformer. The error bars in the simulation are a direct propagation of the error on the currents. (a) shows the y-EMCS at 50 A and (b) the x-EMCS at 15 A. Since the displays of these power supplies already have an accuracy of 0.1 A, the DC/DC converter does not improve the accuracy of the simulations by much, but the agreement is already within the experimental error bars.



(a)



(b)

Figure 3.14: Histograms showing the deviation of the simulated absolute LFCS field values with respect to the measured values. (a) Shows the comparison with individual LFCS coils at 30 A, (b) with individual LFCS coils at 60 A. Simulated values were taken with the currents from the DC/DC converter measurements. The vast bulk of deviations in all situations are below 1%.

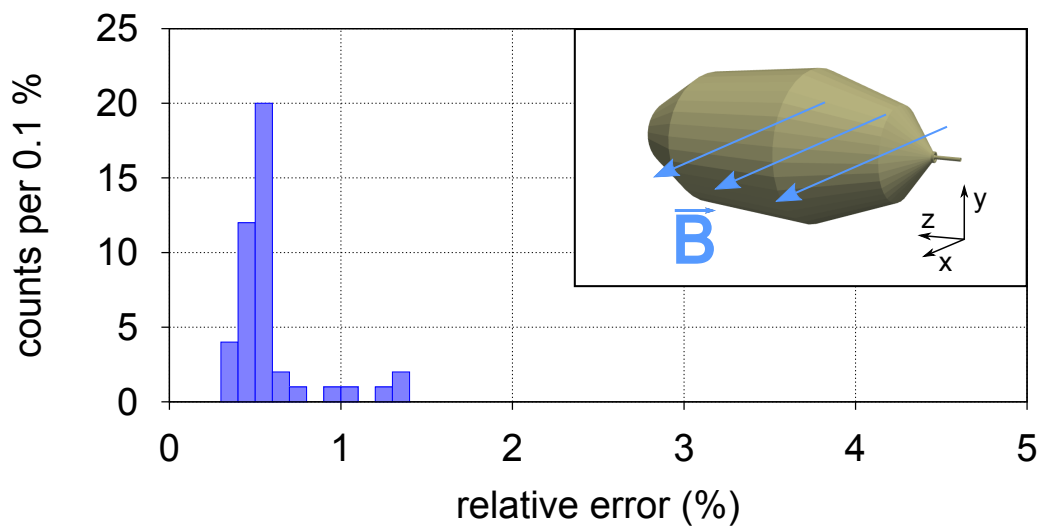
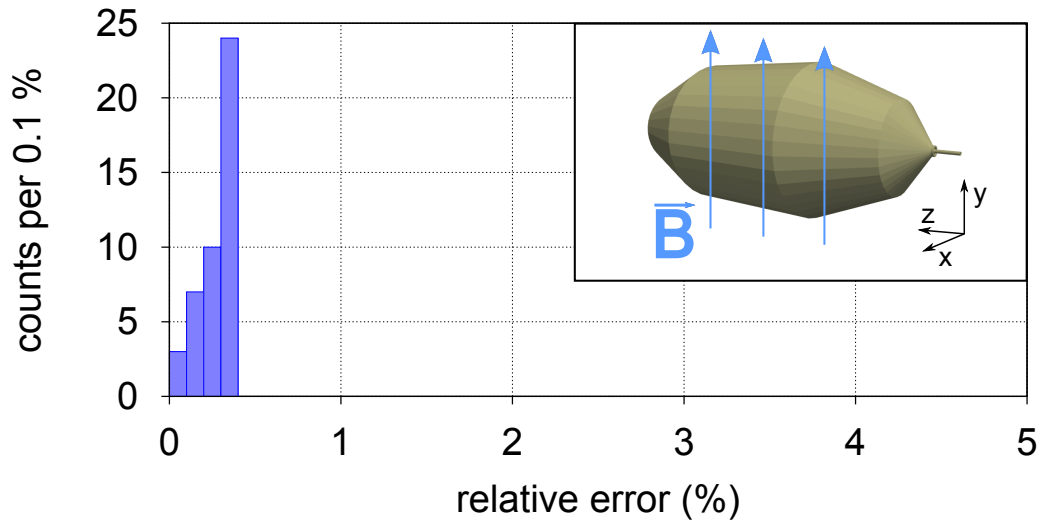
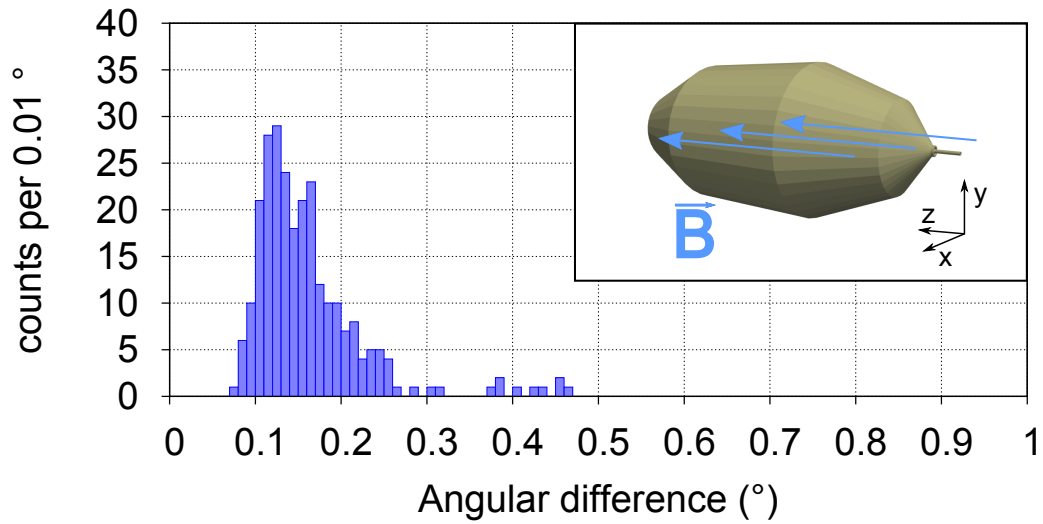
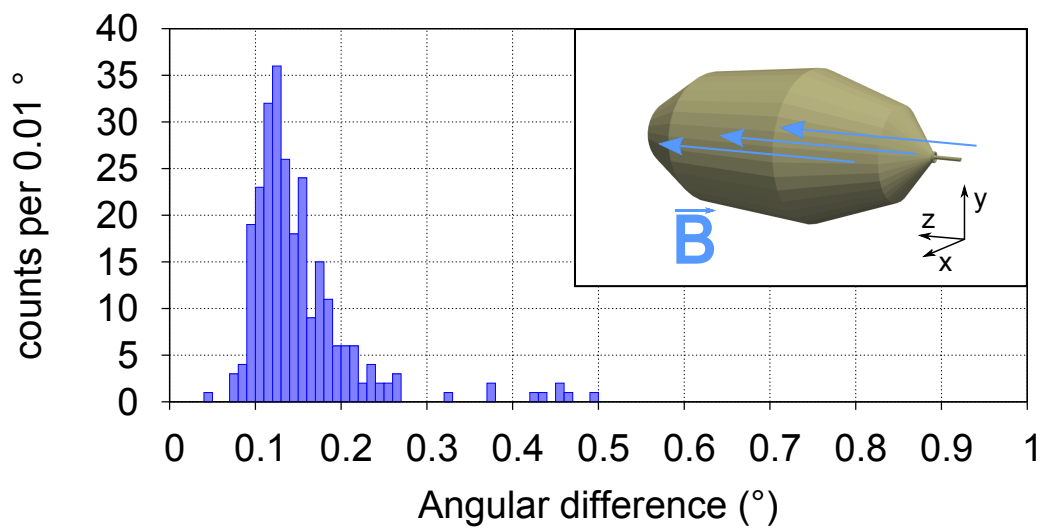


Figure 3.15: Histograms showing the deviation of the simulated absolute EMCS field values with respect to the measured values. (a) the EMCS in vertical direction at 50 A and (b) the EMCS in horizontal direction at 15 A. Simulated values were taken with the currents from the DC/DC converter measurements. All deviations are well below 1% and within the experimental error bars.

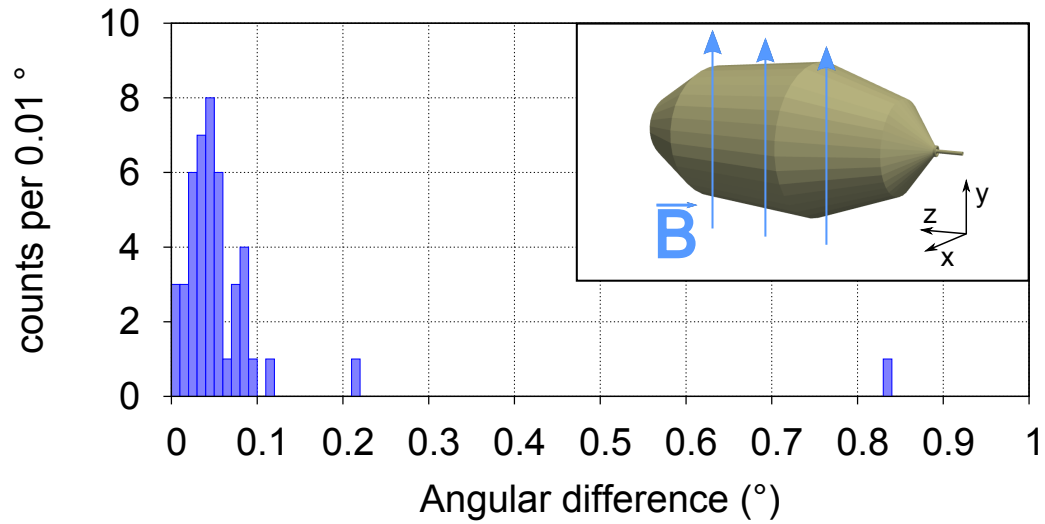


(a)

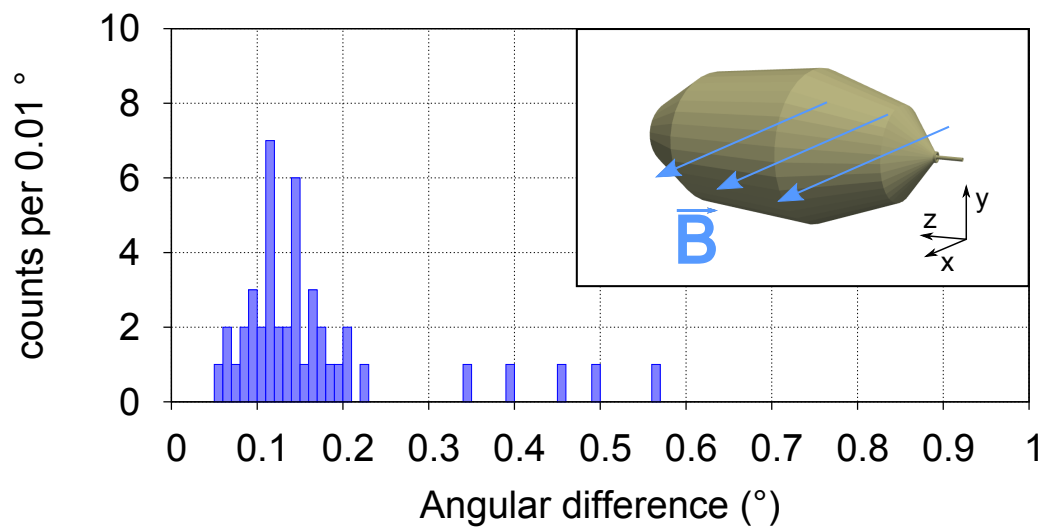


(b)

Figure 3.16: Histogram showing the angular deviations of simulated LFCS field vectors with respect to the measured vectors. As in 3.14 (a) Shows the comparison with individual LFCS coils at 30 A, (b) with individual LFCS coils at 60 A and simulated values were taken with the DC/DC converter current values. The majority of values are clustered between 0.1° and 0.2° which is the limit of the directional measurement with the laser tracker.



(a)



(b)

Figure 3.17: Histogram showing the angular deviations of simulated EMCS field vectors with respect to the measured vectors. Again (a) shows the EMCS values in vertical direction at 50 A and (b) the EMCS in horizontal direction at 15 A with currents measured with the DC/DC converter. As with the LFCS comparison, the values are at the limit of the direction measurement accuracy.

3.4.2 Field Linearity Studies

Another important aspect to look at in this data is linearity. Besides a nonlinearity in the power supply behaviour, an induced magnetisation in the structural materials in the main spectrometer hall can introduce a nonlinearity in the magnetic field.

To study these possible effects, another set of measurements have been taken. In this measurement shown in figure 3.18, the currents applied to the individual air coils were directly measured with a DC/DC converter to 0.1 %. At the same time, their magnetic field was measured at a defined position. For the LFCS coils 1 through 3, this was at the south flange, for 13 and 14 at the north flange of the main spectrometer. The measured magnetic field values do not show a discernible deviation from a linear behaviour and match the simulated values within 0.7 % to 0.2 % depending on the coil. Since the discrepancy is systematic and is constant within one set data set for each coil this can only mean that there is a degree of uncertainty in the distance of the magnetometer to the coil in this measurement. Nonetheless, no nonlinear behaviour has been found for single coils.

An induced magnetization of the structural material would be greatest if all coils at once are powered. Such a scenario was present during the commissioning measurement discussed in the previous section. To check for a magnetization effect, the magnetic fields with the LFCS at 30 A and 60 A are compared in figure 3.19. The field strength at the location of walls of the main spectrometer is below 0.5 mT for 60 A, so the magnetization curve is expected to behave approximately linearly. Since the structural materials used in the main spectrometer hall construction are ferromagnetic, an influence of an induced magnetization would increase the magnetic field of the air coil system. The ratios of the x- and y-components of the magnetic field show a variation of a few percent, as can be expected due to their small value. The absolute field strength is mainly determined by the field in z-direction. The ratio of absolute field strengths is constant at 0.49815 ± 0.00017 (1σ) for all measurement points. This small deviation on the permille level does not indicate a magnetic materials effect as it is in the wrong direction. Instead it is more likely due to an error in the calibration of the power supplies. Since an accurate calibration at this point was not possible, it is not unlikely that the offset of at least some of the power supplies was nonzero.

In conclusion of this chapter it can be noted that the air coil systems at the KATRIN main spectrometer are very nice tools for influencing the magnetic field inside the spectrometer to compensate the earth's magnetic field and optimize the transmission properties of the MAC-E Filter. The air coil systems are well understood and their magnetic fields are represented by simulations below the percent level. Furthermore, no evidence for a nonlinear behaviour caused by induced magnetization has been found.

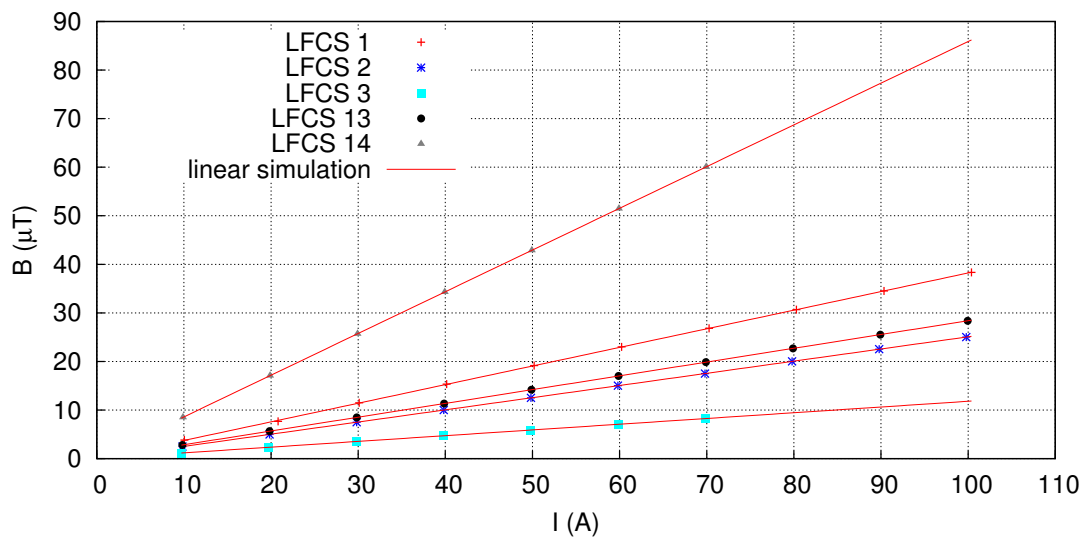


Figure 3.18: LFCS magnetic fields with precise currents: Shown here are the magnetic fields of various LFCS coils at the south (LFCS 1, 2 and 3) and north flanges (LFCS 13 and 14) of the main spectrometer in dependence of the applied air coil current. The red lines are simulations which include the air coil geometry and the measured currents with a linear dependence of the magnetic field on the electric current. The errors on the magnetic field are in the 10 nT regime and not visible in the plot, the error on the current is 0.1 % and also is not visible in the graph.

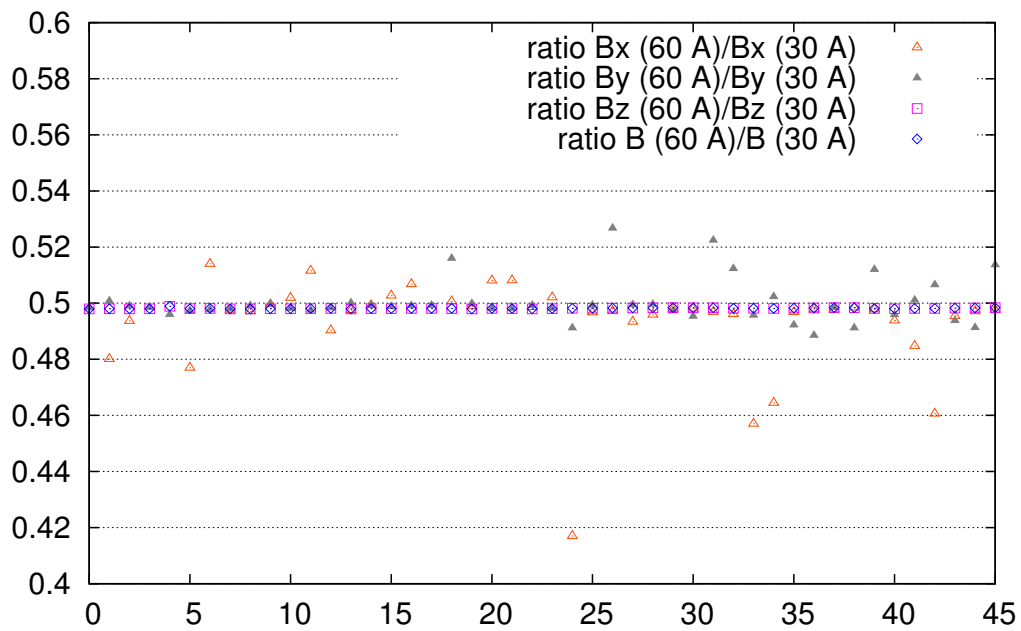


Figure 3.19: Linearity of the LFCS: This graph shows the ratios of magnetic field components produced by all LFCS coils at 30 A and 60 A. The x- and y-components have a spread of a few percent. Since they are small, this spread is not unexpected and no cause for concern. The absolute field strength ratio which is dominated by the z-component is compatible with 0.5 to an excellent degree.

4. Magnetic Field Models for the KATRIN Main Spectrometer

In order to describe the KATRIN setup with its electric and magnetic fields correctly, detailed simulations have to be performed. The KASSIOPEIA simulation software was specifically designed and developed to be a full representation of the KATRIN experiment from source to detector. It is capable of detailed particle tracking simulations to complement the measurements with the KATRIN system. In terms of magnetic fields, this includes simulation not only the fields of the superconducting magnets and the air coil systems discussed in the previous chapter, but also the field of magnetized structural materials.

4.1 The KASSIOPEIA Simulation Software

The main simulation tool for the KATRIN experiment is the KASSIOPEIA software, a C++ based simulation of the KATRIN experiment. It has been developed within the KATRIN collaboration to include creation, trajectory calculation within electromagnetic fields and detection of particles. KASSIOPEIA modules include different particle generators and tracking methods, several field calculation methods. It also includes a variety of physical processes like a doppler broadening in the source, scattering of particles on residual gas molecules, synchrotron radiation and low energy processes in silicon detectors. [63] has an exhaustive description of KASSIOPEIA, in this section the basic properties and workings will be summarized. In section 4.2 the different magnetic field calculation methods will be discussed in more detail as they are of greater relevance to this work.

4.1.1 Aims of KASSIOPEIA

The goal of the KASSIOPEIA simulation is threefold:

It is a valuable tool for the electromagnetic design of KATRIN components. Electric and magnetic fields in the whole KATRIN experiment can be calculated with high precision and speed. Different field calculation methods allow for a range of applications from very fast axially symmetric field calculations to precise and fully three dimensional field models. A very nice example of an application in this function is the design and commissioning of the KATRIN air coil system in chapter 3 of this work.

KASSIOPEIA makes use of these field calculations for full monte carlo simulations to complement measurements with specific experimental setups. The trajectories of particles in electromagnetic fields can be calculated throughout the KATRIN setup down to machine precision. During the commissioning phase and test experiments this

is an invaluable tool to interpret measurements. In the scope of this work it allowed for an estimate of the influence of magnetic materials on transmission properties and background conditions in chapter 6.

Furthermore, the application of KASSIOPEIA allows to investigate systematic effects in the tritium source and also simulations of the actual neutrino mass measurements of KATRIN. In this capacity detailed source models including the tritium final states, doppler broadening, density distributions and energy losses as well as fitting of the integrated tritium β -spectrum are involved. Such applications can be found for example in [65].

4.1.2 Organisation of Monte Carlo Simulations

The data provided by KASSIOPEIA is structured in four levels of detail. Each level of information is saved in a specific data container depending on the detail of information provided. The four levels are run, event, track and step.

Run

The highest level of organisation is a run. It contains all information produced in a single instance of KASSIOPEIA. It is the sum of all events and stores information concerning the whole run like the number of events, the physical time the run took. No physical parameters in the simulation may be changed during one run. This organisation level is resembling an experimental run, a fixed time of data taking with fixed experimental parameters.

Event

An event is composed of a primary particle created by a generator module and its secondary and subsequent particles created by particles of that same event. All those particles are represented by tracks which are linked to the event. It also contains general information like a creation ID, number of tracks and initial and final time.

Track

In a track, physical information about single particles and their trajectories are managed. A particle is represented by an instantaneous physical state of a track, defined by a position and a momentum vector, rest mass, charge, spin, lifetime and particle ID number matching the PDG standard. In KASSIOPEIA, track contain the initial particle state as well as the current state which is consecutively updated as the simulation progresses. In addition, they contain non-physical information used in the simulation like an event-unique ID number that is sequentially assigned to particles within an event. If it is a non-primary particle, the parent particle track number is also stored, for primary particles this is -1 by default. It also stores parameters like path length, elapsed time, number of steps in the trajectory calculation and an exit condition ID containing the reason why track calculation was stopped.

Step

A step is the most detailed level of information considered in KASSIOPEIA. It is an incremental discrete change of the physical particle state in a track. It is generally divided in two conceptual parts. First the numerical solution to an equation of motion and second the simulation of discrete physical processes like scattering or synchrotron radiation that may occur during the step. Steps also keep track of their initial state represented as a particle. If the step computation is successful and the final state is physically acceptable this final state becomes the most current physical state of the track containing the step.

4.1.3 Particle Creation and Tracking

To run a simulation, KASSIOPEIA utilizes managers, they control the activation of modules at a specific time. These modules are responsible for initializing and updating the contents of the data containers discussed above.

Particle Creation

The generation of particles is done by methods in the **KASSIOPEIA Particle Generator** KPAGE developed in [82]. It allows for a modular construction of particle starting parameters. These parameters are time, position, energy and direction. All of these can be determined by various methods and mixed to accommodate a wide range of different starting conditions to simulate all kinds of experimental conditions from tritium measurements to background processes triggered by the decay of heavy isotopes like Radon in the spectrometer volume.

Particle Tracking

The computation of particle trajectories is done by the KTRACK simulation package for any kind of particle. KTRACK allows to choose between the accurate solving of the Lorentz equation and the faster guiding center method using the adiabaticity of the motion. In the latter, the gyrotron motion is analytically approximated. In both methods, additional physical processes can be taken into account. So for each simulation, the option of adding synchrotron radiation or elastic and inelastic scattering on various residual gas elements can be chosen. KTRACK also allows to choose from a variety of conditions on which the tracking is stopped, like a geometry intersection a maximal number of steps or elapsed time and others.

Particle Detection

To simulate a realistic detector response, the **KATRIN** electron scattering in silicon package KESS developed in [83] was developed to compute the interactions of low-energy electrons with a kinetic energy of $E_{\text{kin}} < 50$ keV. No previous simulation code was able to cover this energy range which is of interest to the KATRIN experiment.

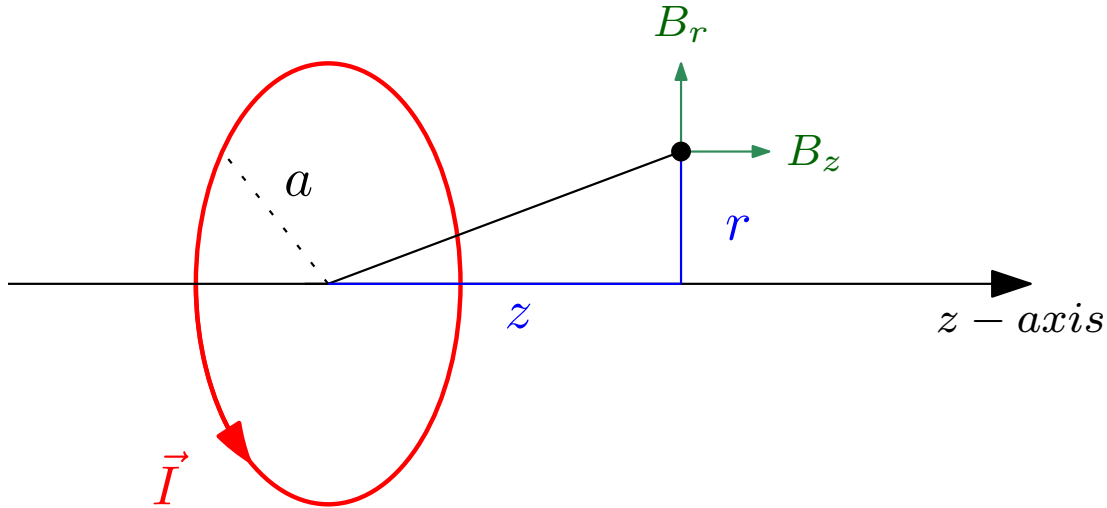


Figure 4.1: The current \vec{I} running through a circular loop with radius a creates a magnetic field \vec{B} .

4.2 Magnetic Field Calculation Methods

Knowledge of magnetic fields in the KATRIN experiment is vital for the success of the experiment and its complementing simulations. Not only is the particle tracking depending on field calculations but also electromagnetic design decisions are made based on field simulations. The field calculation methods for KATRIN were developed in [84] and implemented in the KASSIOPEIA framework in [85] as well as [86].

Although the energy analysis is in principle done by electrostatic fields, the magnetic fields play an important role not only by guiding the decay electrons through the spectrometer, but also in adiabatically transforming the transverse motion into a longitudinal one. In addition, they provide a background reduction by magnetic shielding of intruding electrons. For the calculation of axially symmetric fields, the Legendre Polynomial methods of calculating magnetic fields with elliptic integrals or zonal harmonic expansions provide accuracy and calculation speed. To handle non-axially symmetric fields, the field distribution of arbitrary current geometries can be calculated using the integrated Biot-Savart's law and the field of magnetised material can be approximated by a geometry of magnetic dipoles. Since these non-axially symmetric methods tend to grow slow with increasingly complex geometries, the Hermite Interpolation method can speed their calculation up with pre-generated field maps. Below, these magnetic field calculation methods used in KASSIOPEIA will be detailed. The drawings are taken from [85].

4.2.1 Elliptic Integrals

The main field generating components of KATRIN are superconducting magnets with a circular geometry. The LFCS air coils can also be described as such, depending on the detail of the simulation. Such a current loop with a rotational symmetry axis is shown in figure 4.1

Biot-Savarts law for a thin current path

$$d\vec{B} = \frac{\mu_0}{4\pi} \frac{I d\vec{l} \times \hat{r}}{r^2} \quad (4.1)$$

can be expressed with the complete elliptic integrals

$$\begin{aligned} K(k) &= \int_0^{\frac{\pi}{2}} \frac{d\varphi}{\sqrt{1 - k^2 \sin^2 \varphi}} \\ E(k) &= \int_0^{\frac{\pi}{2}} d\varphi \sqrt{1 - k^2 \sin^2 \varphi} \\ \Pi(c, k) &= \int_0^{\frac{\pi}{2}} \frac{d\varphi}{1 - c^2 \sin^2 \varphi \sqrt{1 - k^2 \sin^2 \varphi}} \end{aligned} \quad (4.2)$$

With these, the components of the magnetic field can be expressed [62] as:

$$\begin{aligned} B_r &= \frac{I}{c} \cdot \frac{2z}{r\sqrt{(a+r)^2 + z^2}} \left[-K(k) + \frac{a^2 + r^2 + z^2}{(a+r)^2 + z^2} E(k) \right] \\ B_\varphi &= 0 \\ B_z &= \frac{I}{c} \cdot \frac{2z}{r\sqrt{(a+r)^2 + z^2}} \left[K(k) + \frac{a^2 - r^2 - z^2}{(a+r)^2 + z^2} E(k) \right] \end{aligned} \quad (4.3)$$

with φ the azimuthal angle, r the radius and z the axial position of the location where the field is calculated. a is the radius of the coil, and I the current. c and k are parameters depending on a , r and z . A coil of finite length can be considered by using the third integral $\Pi(c, k)$. With these solutions, the magnetic field can be calculated anywhere, and the application of Carlson's elliptic integrals R_F , R_J and R_D [87] gives a fast numerical computational solution. Nonetheless, for coils with a finite thickness, another numerical integration over their radius is necessary which leaves room for improvements in calculation speed.

4.2.2 Zonal Harmonic Expansion

To speed up the calculation of magnetic fields using the elliptic integrals, the zonal harmonic expansion method can be used. The magnetic field at a point $\vec{p}(r, z)$ near the symmetry axis can be written in terms of a Legendre Polynomial expansion and its derivatives at a point on the symmetry axis. This on-axis point is called a source point. By preparing the source coefficients beforehand, this offers a fast field calculation with variable precision, depending on the order to which the Legendre Polynomials are expanded.

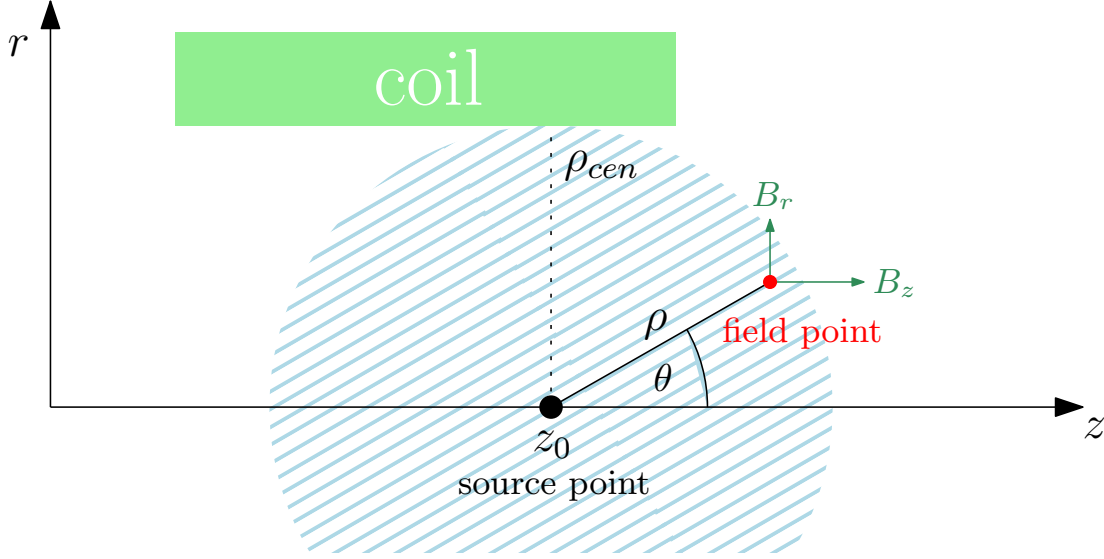


Figure 4.2: Convergence radius of the Central Zonal Harmonic Expansion: If the point where the field is calculated lies within a distance of $\rho < \rho_{\text{cen}}$ the central expansion 4.4 can be used.

If the distance from the source point to the point where the field is computed is smaller than the distance from the source point to the closest point of the coil volume as shown in figure 4.2, the central expansion

$$\begin{aligned}
 B_r &= -\sin \varphi \sum_{n=1}^{\infty} \frac{B_n^{\text{cen}}}{n+1} \left(\frac{\rho}{\rho_{\text{cen}}} \right)^n P'_n(\cos \Theta) \\
 B_\varphi &= 0 \\
 B_z &= \sum_{n=0}^{\infty} B_n^{\text{cen}} \left(\frac{\rho}{\rho_{\text{cen}}} \right)^n P_n(\cos \Theta)
 \end{aligned} \tag{4.4}$$

can be used to compute the magnetic field. $P_n(\cos \Theta)$ are the Legendre Polynomials and the central convergence radius ρ_{cen} is the smallest distance between source point and coil volume. 4.4 is only valid if $\rho < \rho_{\text{cen}}$.

To calculate the field further from the source point, the remote expansion has to be used. It is only valid if the point at which the field is to be calculated is further from the source point than the farthest point of the coil volume as depicted in figure 4.3. In this case, the field is given by

$$\begin{aligned}
 B_r &= \sin \varphi \sum_{n=2}^{\infty} \frac{B_n^{\text{rem}}}{n} \left(\frac{\rho_{\text{rem}}}{\rho} \right)^{n+1} P'_n(\cos \Theta) \\
 B_\varphi &= 0 \\
 B_z &= \sum_{n=2}^{\infty} B_n^{\text{rem}} \left(\frac{\rho_{\text{rem}}}{\rho} \right)^{n+1} P_n(\cos \Theta)
 \end{aligned} \tag{4.5}$$

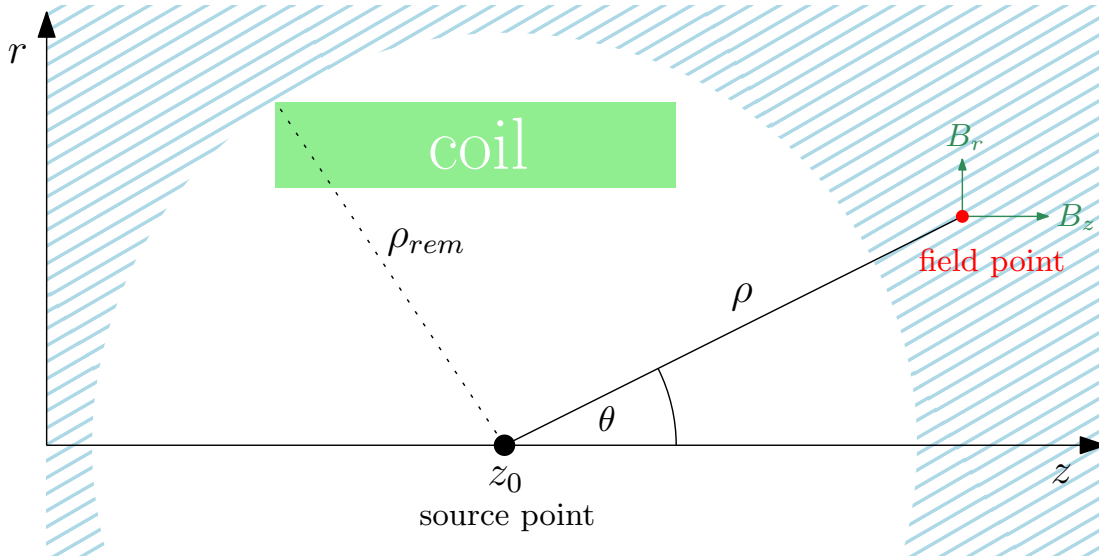


Figure 4.3: Convergence radius of the Remote Zonal Harmonic Expansion: If the point where the field is calculated lies within a distance of $\rho > \rho_{\text{rem}}$ the remote expansion 4.5 can be used.

with the remote expansion coefficients B_n^{rem} .

So with a single source point, the field can be calculated very quickly almost everywhere, except in the area near the coil itself. For multiple coils, ρ_{cen} is given by the distance to the closest coil and ρ_{rem} by the distance to the farthest coil as shown in figure 4.4. This enlarges the inaccessible region with increasing complexity of the system.

To remedy this problem, additional source points can be calculated. From these points, different convergence radii allow the calculation of fields at different regions. With conveniently placed source points, the magnetic field can be calculated almost anywhere in the setup, except for the region occupied by the coils themselves. Figure 4.5 shows the advantage gained by additional source points. Adding more source points also speeds up the calculation, since the polynomial expansion converges faster if $\frac{\rho}{\rho_{\text{cen}}}$ and $\frac{\rho_{\text{rem}}}{\rho}$ are smaller. Choosing the right source point gives a faster field calculation.

The Zonal Harmonic Expansion method allows for a fast and accurate calculation of magnetic fields, as sketched in figure 4.6. Even arrangements of coils with different symmetry axes can be calculated. Source points are calculated in their respective coordinate system and the magnetic field is subsequently transformed back to the reference system.

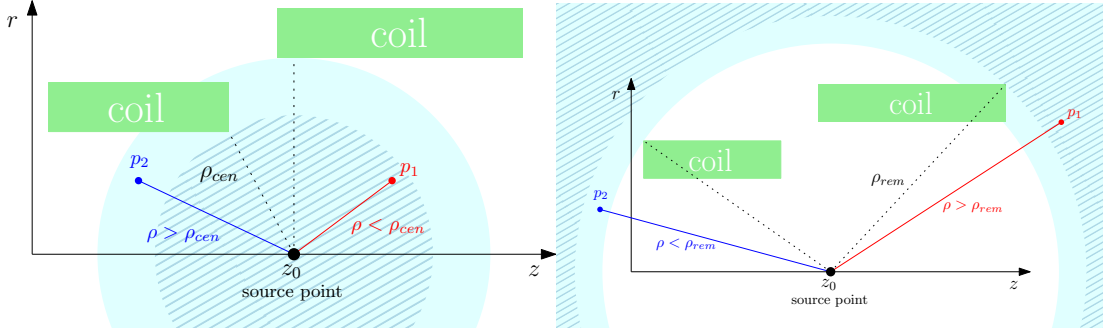


Figure 4.4: Convergence radii for multiple coils: The inaccessible region grows with more coils. The magnetic fields at points p_1 are computable, unlike the fields at points p_2 . **left:** The central convergence radius ρ_{cen} is defined by the closest coil. **right:** The remote convergence radius ρ_{rem} is defined by the farthest coil.

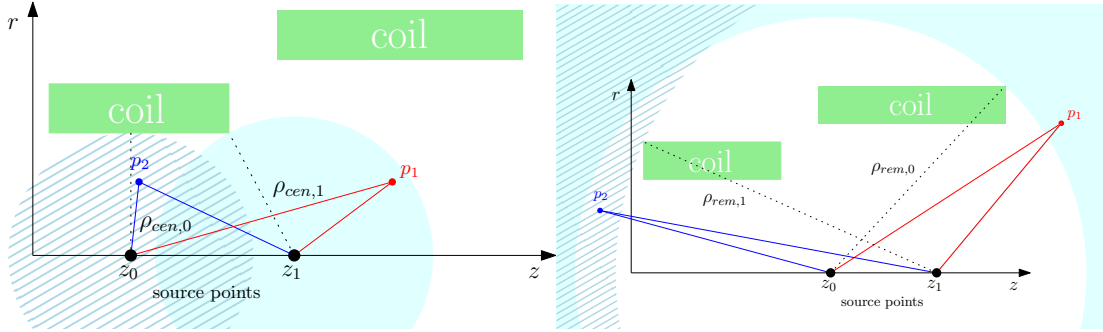


Figure 4.5: Convergence radii for multiple coils with additional source points. With conveniently placed additional source points, the magnetic field at location p_1 and p_2 can both be calculated. **left:** Central convergence radius ρ_{cen} . **right:** Remote convergence radius ρ_{rem} .

The drawback of the Zonal Harmonic Expansion is that the source coefficients B_n^{cen} and B_n^{rem} have to be calculated for each source point in preparation for the actual field calculation. They are given by two dimensional integrals over the coil geometry:

$$\begin{aligned}
 B_n^{cen} &= \int_{R_{min}}^{R_{max}} dR \int_{Z_{min}}^{Z_{max}} dZ \cdot b_n(R, Z) \\
 B_n^{rem} &= \int_{R_{min}}^{R_{max}} dR \int_{Z_{min}}^{Z_{max}} dZ \dot{b}_n^*(R, Z)
 \end{aligned} \tag{4.6}$$

with

$$\begin{aligned}
 b_n(R, Z) &= \frac{\mu_0 I}{2A\rho_{cen}} \left(1 - \left(\frac{Z - z_0}{\rho_{ZR}} \right)^2 \right) \left(\frac{\rho_{cen}}{\rho_{ZR}} \right)^{n+1} P'_{n+1} \left(\frac{Z - z_0}{\rho_{ZR}} \right) \\
 \dot{b}_n^*(R, Z) &= \frac{\mu_0 I}{2A\rho_{cen}} \left(1 - \left(\frac{Z - z_0}{\rho_{ZR}} \right)^2 \right) \left(\frac{\rho_{rem}}{\rho_{ZR}} \right)^n P'_{n-1} \left(\frac{Z - z_0}{\rho_{ZR}} \right)
 \end{aligned} \tag{4.7}$$

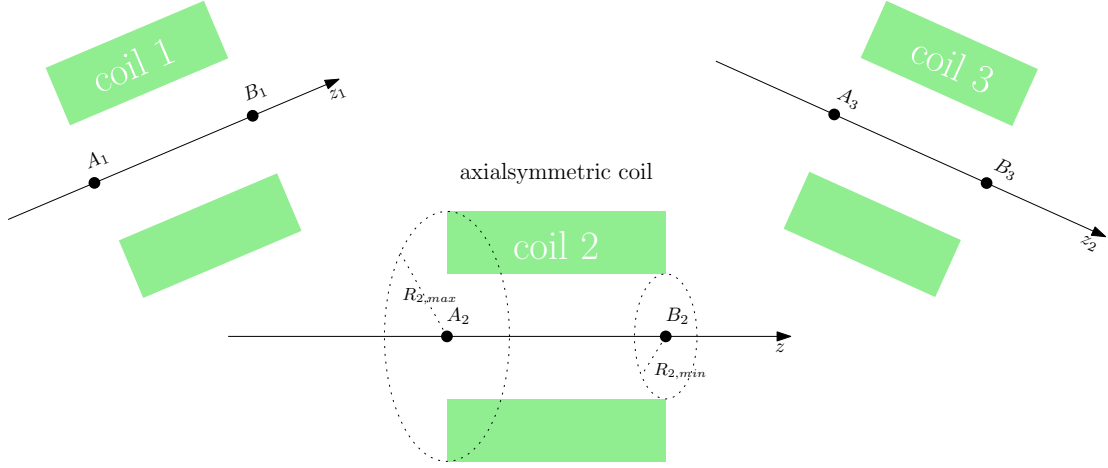


Figure 4.6: Source points of coils with different symmetry axes. The source points of different coils can be combined to calculate the field of an arbitrary coil setup.

Once computed, these source point files can be used to calculate the same magnetic field setup without the need for any further preparation [88].

4.2.3 Biot-Savart's Law

In addition to the axially symmetric superconduction coils, there are magnetic components in the KATRIN setup, that are oddly shaped, like the EMCS coils. This also includes the gravitational deformation of the LFCS, if such a level of detail is required in the simulation, as well as dipole coils in the DPS1-F, DPS1-R and the rear section. For the fields of such components, the integrated Biot-Savart method is needed.

The magnetic field of an arbitrarily shaped current-carrying component is described by Biot-Savart's law: The field of an infinitesimally small segment $d\vec{l}$ of an infinitely long conductor with current I is given by

$$d\vec{B} = \frac{\mu_0}{4\pi} \frac{I d\vec{l} \times \hat{r}}{r^2} \quad (4.8)$$

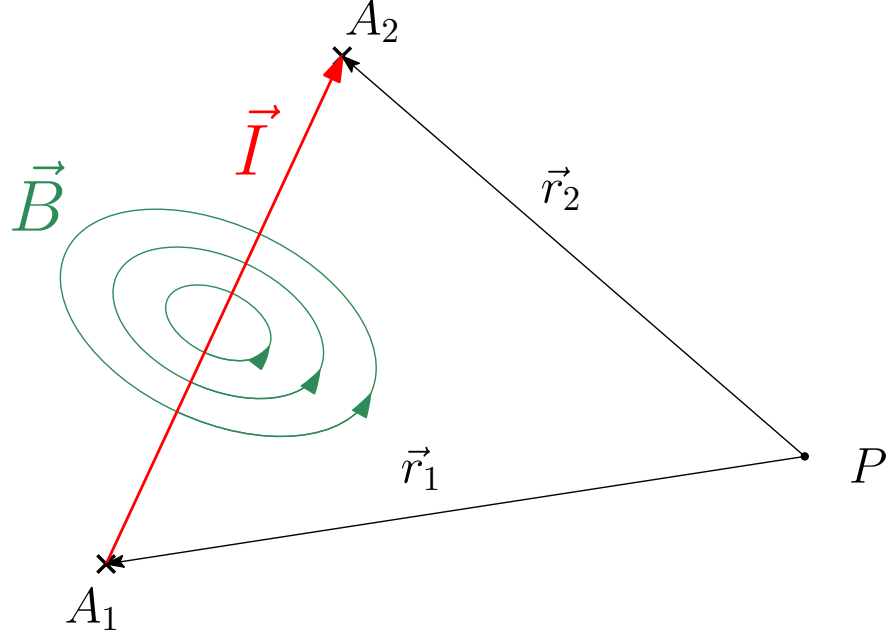
with \vec{r} being the position where the field is calculated. To get the field of a finite line segment, like in figure 4.7, 4.8 is integrated along $d\vec{l}$:

$$\vec{B}_i = \frac{\mu_0}{4\pi} d\vec{L} \times \vec{I} \quad (4.9)$$

with

$$d\vec{L} = \left(\frac{\hat{r}_1 + \hat{r}_2}{R + l} - \frac{\hat{r}_1 + \hat{r}_2}{R - l} \right), \quad R = |\vec{r}_1| + |\vec{r}_2|, \quad l = |\vec{r}_2 - \vec{r}_1|, \quad \text{and} \quad \hat{r}_i = \frac{\vec{r}_i}{|\vec{r}_i|} \quad (4.10)$$

Figure 4.7:
Integrated
Biot-Savart
field calculation: The line current segment $d\vec{L}$ is defined by a starting point A_1 , an end point A_2 and the current $|\vec{I}|$ flowing from A_1 to A_2 .



The magnetic field of the whole setup is then calculated by using a superposition of all line elements. With this method it is possible to compute the field of very complex current path arrangements by approximating it with a number of linear segments approximating the actual current setup with sufficient accuracy. The overall field is then the sum of the field of the individual components:

$$\vec{B}_{\text{tot}} = \sum_{i=1}^N \vec{B}_i \quad (4.11)$$

This kind of geometry approximation is susceptible to errors in setting up the line segments in a non-physical way. To check for this kind of errors, the validity of Maxwell's equations can be checked. For example the rotation of the magnetic field in vacuum $\vec{\nabla} \times \vec{B}_{\text{tot}} = 0$ should vanish. If it does not, the current loop is probably not closed and should be checked.

4.2.4 Magnetic Dipoles

Since the KATRIN experiment unfortunately is not situated in an ideal environment, not only the intended magnetic setup contributes to the magnetic field. The structural materials of the building in which the experiment is housed influence the field inside the main spectrometer by a small amount. These fields are highly inhomogeneous and are potentially hazardous to the electron guiding and magnetic shielding. To reduce this influence as far as possible, the basement of the KATRIN main spectrometer hall has been reinforced with stainless steel instead of the normal steel that is usually used in construction. The steel content of the walls has also been limited for each section [89] although only normal steel is used there. Nonetheless, a certain amount of magnetizable material remains in the vicinity of the main spectrometer. Since these steel bars

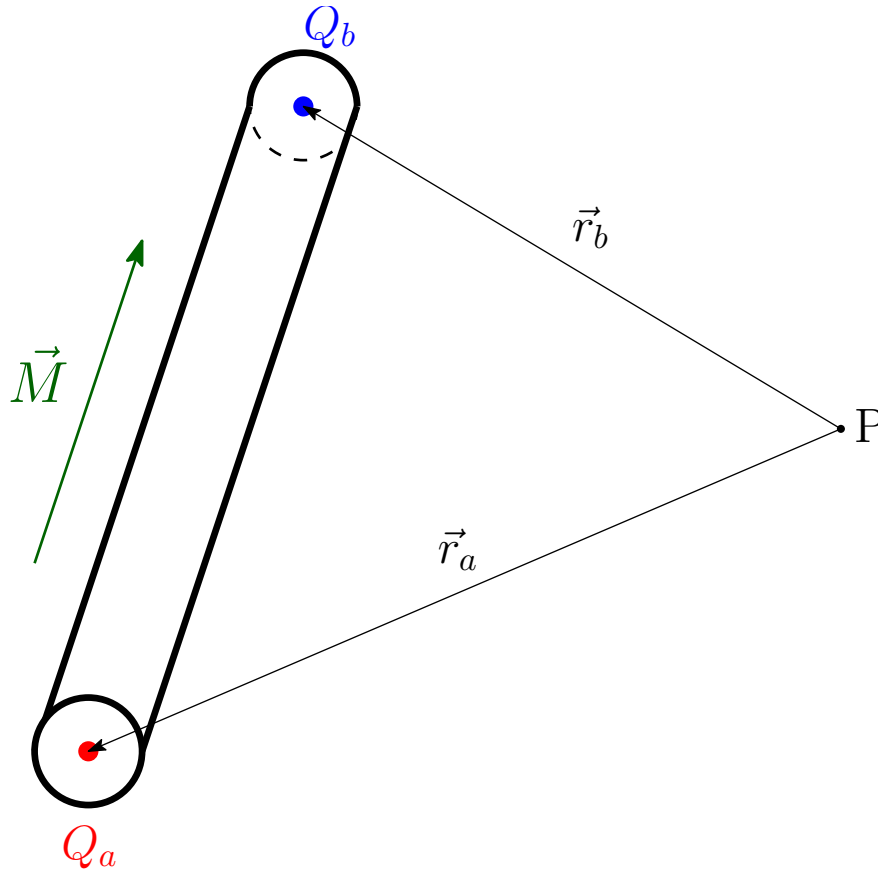


Figure 4.8:
Magnetic dipole field calculation model: Steel bars are modeled with two "magnetic monopoles" with opposite fictive "magnetic charges" at the end of the bar. The field is then calculated as a superposition of the field of both poles.

are usually lifted with magnetic cranes, they can be expected to have a remanent magnetization. During the construction of the hall, taking into account the magnetization of the structural material was no priority and no information about the magnetization strength or direction is available.

To get a handle on the field of these materials, a flexible model is needed to compute their effects. The straightforward approach would be using the equation for the field of a dipole with fixed magnetic moment:

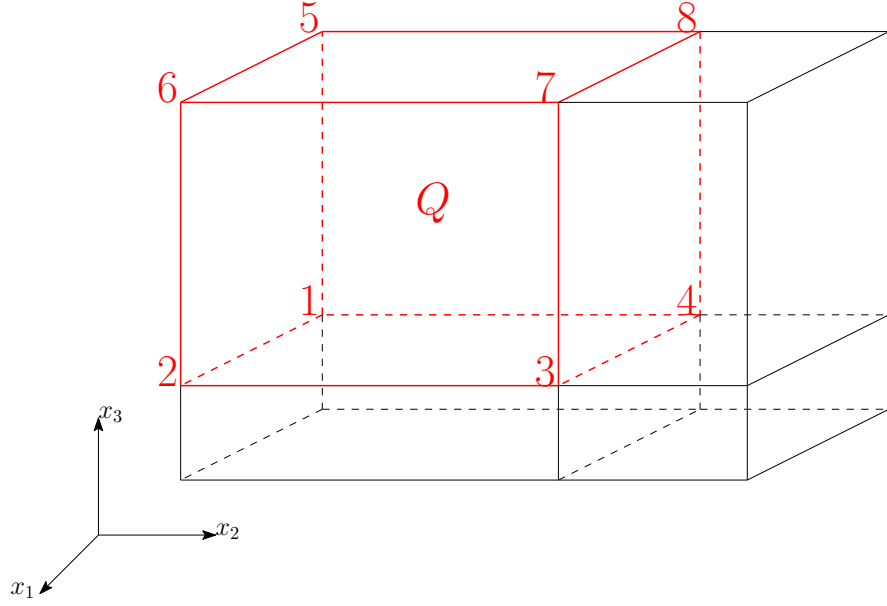
$$\vec{B} = \frac{\mu_0}{4\pi} \frac{3\vec{r}(\vec{m})\vec{r} - \vec{m}r^2}{r^5} \quad (4.12)$$

with $\vec{m} = V\vec{M}$. This formula is valid for small dipoles only. Fortunately, integrating 4.12 gives the formula for two magnetic dipoles with a magnetic "charge" placed at both ends of the bar. These can be spaced apart from each other to approximate the geometry of the steel bars. This model is sketched in figure 4.8.

The magnetic field of this dipole setup is calculated as a superposition of two coulomb fields:

$$\vec{B}_i(\vec{P}) = -Q \frac{\mu_0}{4\pi} \left(\frac{\vec{r}_a}{|\vec{r}_a|^3} - \frac{\vec{r}_b}{|\vec{r}_b|^3} \right) \quad (4.13)$$

Figure 4.9:
Cuboid of an interpolation grid. For the 3D Hermite interpolation, the field values and their derivatives at the corners of the cuboid are needed.



with $Q = \left| \vec{M} \right| \cdot \pi r_{\text{bar}}^2$ as a parameter. To get the total field for the structural materials, the sum over all dipole fields \vec{B}_i has to be taken. Placing a single "magnetic charge" would create an unphysical situation but as they are only placed in pairs, this cannot occur. Even with this flexible dipole model it is not a trivial task to create a model of the field of the magnetic materials. It involves fitting a dipole distribution to many measurements. This problematic will be discussed further in chapter 5.

4.2.5 3D Hermite Interpolation

Both the integrated Biot-Savart and the magnetic dipole model may involve summations over a large number of elements which introduces a significant increase in computation time. Interpolation methods offer a fast alternative with pre-computed grids. These grids are calculated once in advance and are used to evaluate the field via interpolation. Although the Hermite interpolation method uses not only the field values at the grid points but also their partial derivatives, a gain in accuracy more than makes up for the increased time needed to pre-calculate the grid. For non-axially symmetric fields this is a very convenient method to calculate fields in a fast and accurate manner.

To interpolate the field, a three dimensional grid consisting of cuboids, as shown in figure 4.9, is needed. Such a cuboid Q can be described as:

$$Q := \{(x_1, x_2, x_3) \in \mathbb{R}^3 \mid x_{ui} < x_i < x_{oi}; i = 1, 2, 3\} \quad (4.14)$$

With the coordinate transformation of the form

$$\begin{aligned} u_i &= \frac{x_i - x_{mi}}{a_i} \\ \text{with } x_{mi} &= \frac{x_{oi} + x_{ui}}{2} \\ \text{and } a_i &= \frac{x_{oi} - x_{ui}}{2} \end{aligned} \quad (4.15)$$

it is projected onto the unit cube E :

$$E := \{(u_1, u_2, u_3) \in \mathbb{R}^3 / -1 < u_i < 1; i = 1, 2, 3\} \quad (4.16)$$

The function $g(\vec{u})$ is defined on E . With $f(\vec{x}) = g(\vec{u}(\vec{x}))$, $g(\vec{u})$ can be interpolated within the unit cube E . To do this, the function values at the eight corner points \vec{u}_i as well as their first partial derivative are needed. For computation they are combined in the matrix \mathcal{G} with the function values in the 0th column and their derivatives in the subsequent columns:

$$\begin{aligned} \mathcal{G}_{i0} &:= g(\vec{u}_i), \quad (i = 1, \dots, 8) \\ \mathcal{G}_{ij} &:= \left\{ \frac{\partial g(\vec{u})}{\partial u_j} \right\}_{\vec{u}=\vec{u}_i}, \quad (i = 1, \dots, 8; j = 1, 2, 3) \end{aligned} \quad (4.17)$$

The interpolation polynomial is defined as

$$G(\vec{u}) = \sum_{i=1}^8 \sum_{j=0}^3 \mathcal{G}_{ij} \phi_{ij}(\vec{u}) \quad (4.18)$$

The coefficient polynomials ϕ_{ij} are chosen so that $G(\vec{u}_k) = \mathcal{G}_{k0}$ and $\left\{ \frac{\partial g \vec{u}_i}{\partial u_1} \right\}_{\vec{u}=\vec{u}_k} = \mathcal{G}_{k1}$. This puts the following constraints on ϕ_{ij} :

$$\phi_{ij}(\vec{u}_k) = \delta_{ik} \delta_{j0} \quad \text{and} \quad \left\{ \frac{\partial \phi_{ij}(\vec{u})}{\partial u_1} \right\}_{\vec{u}=\vec{u}_k} = \delta_{ik} \delta_{j1} \quad (4.19)$$

These are fulfilled if

$$\phi_{ij}(\vec{u}) := u_{ij} \prod_{k=1}^3 \varphi_{jk}(u_{ik} \cdot \vec{u}_k) \quad (4.20)$$

here, φ_{jk} is given by

$$\varphi_{jk}(t) := \frac{1}{4} [(2 + 3t - t^3) + (-3 - 4t + t^2 + 2t^3)\delta_{ik}] \quad \text{and} \quad u_{i0} := 1 \quad (4.21)$$

For the interpolation of $f(\vec{x})$ within the cuboid Q , three steps have to be taken:

- calculate $f(\vec{x})$ and its partial derivatives with respect to \vec{x} at the corner points of the cuboid
- transform these values into the unit cube E

$$\mathcal{G}_{ij} = \begin{cases} a_j \cdot \left\{ \frac{\partial f(\vec{x})}{\partial x_j} \right\}_{\vec{x}=\vec{x}_i} & \text{if } j > 0 \\ f(\vec{x}_i) & \text{if } j = 0 \end{cases} \quad (4.22)$$

- interpolate the function values and derivatives at any point in $\vec{x} \in Q$:

$$\frac{\partial f(\vec{x})}{\partial x_j} = a_j^{-1} \cdot \frac{\partial G(\vec{U}(\vec{x}))}{\partial u_j}, \quad j = 1, 2, 3, \quad f(\vec{x}) = G(\vec{U}(\vec{x})) \quad (4.23)$$

This interpolation method can of course also be used to calculate electric fields. The accuracy of the calculation depends on the grid spacing. The smaller the cuboids, the more accurate the interpolation gets. This does not influence the time needed to interpolate the field value, but it does influence the time needed to compute the interpolation grid.

With these field calculation methods at hand it is possible to simulate the magnetic fields in the KATRIN setup with very high precision in a reasonable time. This allows fast and accurate particle tracking simulations and electromagnetic design simulations.

5. Magnetic Materials in Measurement and Simulation

During the planning of the construction of the KATRIN experimental hall, it was predicted that magnetic materials used in reinforcing the walls and foundations would disturb the magnetic design of the experiment. This was considered by planning the structural layout of the building and stainless steel was used to reinforce the central part of the basement which is closest to the KATRIN main spectrometer. Since then, no further studies of this effect were done, until [76], the work leading up to the one in hand. There, it was observed, that the magnetic materials produce a measurable field in the central part of the main spectrometer. It also contains field surveys done in the KATRIN hall. In the work at hand, precise measurements inside the spectrometer volume were done during the air coil commissioning described in chapter 3 as well as studies on the time dependency and influences of superconducting magnets. An important part of this work was also the creation of a magnetic field model reflecting the field of the magnetic materials in the KASSIOPEIA simulations.

5.1 Experimental Observation

The first evidence of an inhomogeneous non-axially symmetric field produced by the magnetic materials was found in [76]. Figure 5.1 shows the experimental data taken near the analyzing plane on seven positions at approximately the same z-position. The model used to describe the data is composed of two dipoles at ± 10 m. The equation describing the absolute field strength is given by

$$B(x) = B_0 + \frac{D_1}{(10 \text{ m} + x)^3} + \frac{D_2}{(10 \text{ m} - x)^3} \quad (5.1)$$

This first observation triggered various measurement activities performed in [76], [77] and this work.

5.1.1 Field Survey in the KATRIN Hall

The magnetic background field in the KATRIN hall has been measured on various occasions. These include measurements near the walls in the basement and ground floor as well as on the pre-spectrometer platform and near the main spectrometer vessel. Figure 5.2 shows a comprehensive overview of all regions in which the field has been measured.

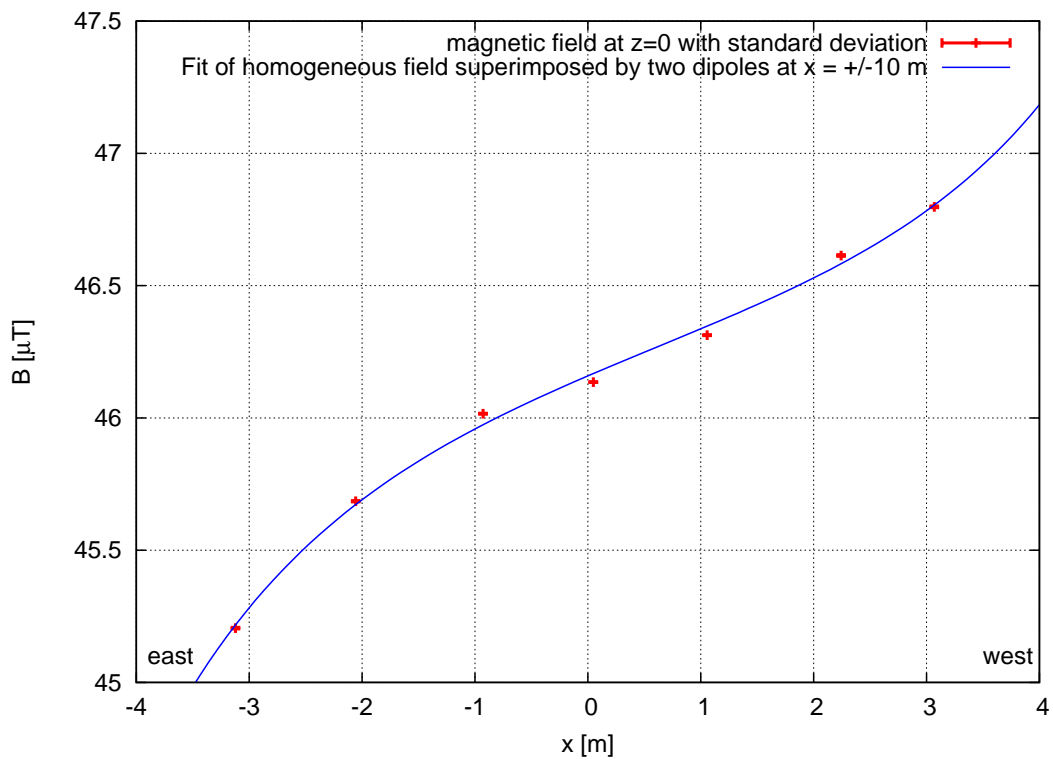


Figure 5.1: First evidence for a magnetic materials field: The absolute field strength varies over the x-axis in the central part of the main spectrometer. The crude field model fits the data very well, a clear indication that this field is in fact due to magnetic materials.

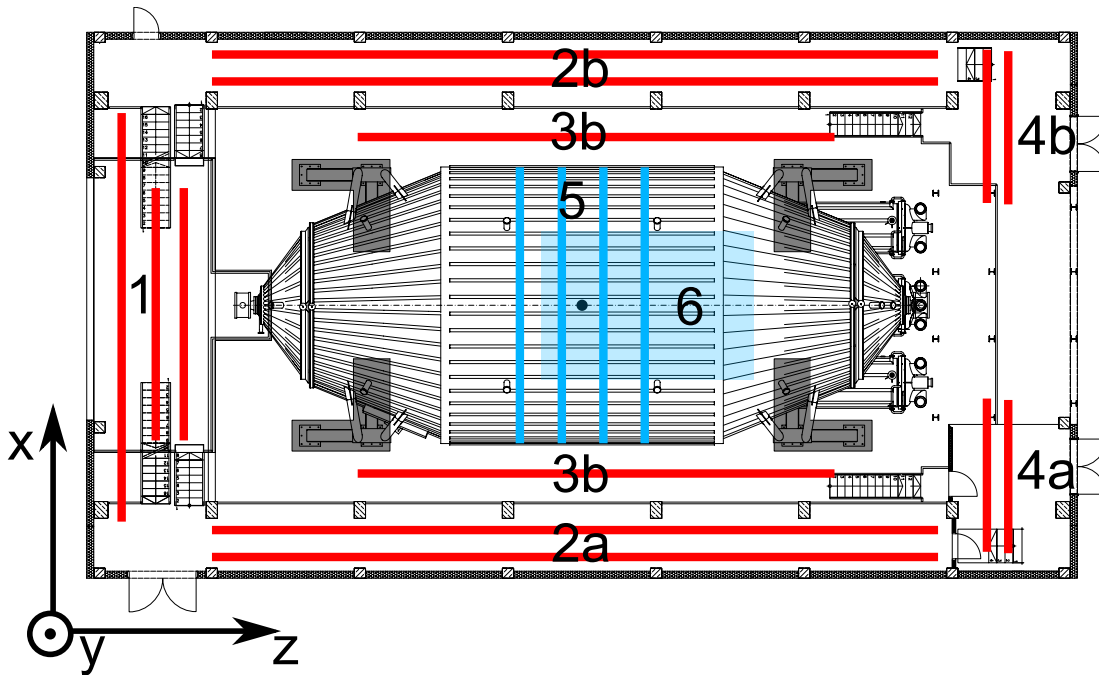


Figure 5.2: Magnetic field survey regions: (1) On and below the pre-spectrometer platform. (2) near the eastern and western walls in the basement and on the gallery. (3) In the basement near the main spectrometer. (4) in the basement below the detector platform. The blue regions (5) and (6) depict the measurement regions inside the main spectrometer. (5) On the rail system. (6) In the equatorial plane.

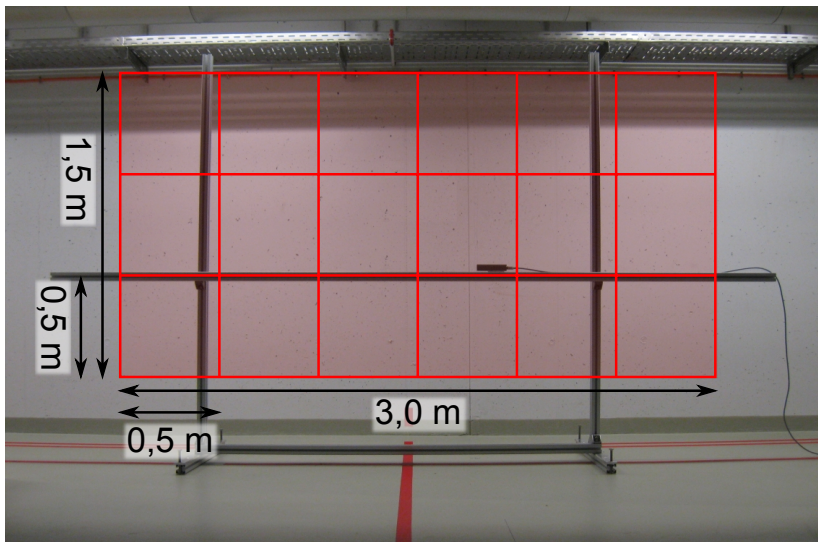


Figure 5.3: Holding structure and measurement grid during field surveys: The holding frame is made of aluminum, the height of the beam on which the magnetometer is fixed on a plastic sled is adjustable. With this setup, a grid of 0.5×0.5 m was measured along the lines shown in figure 5.2.

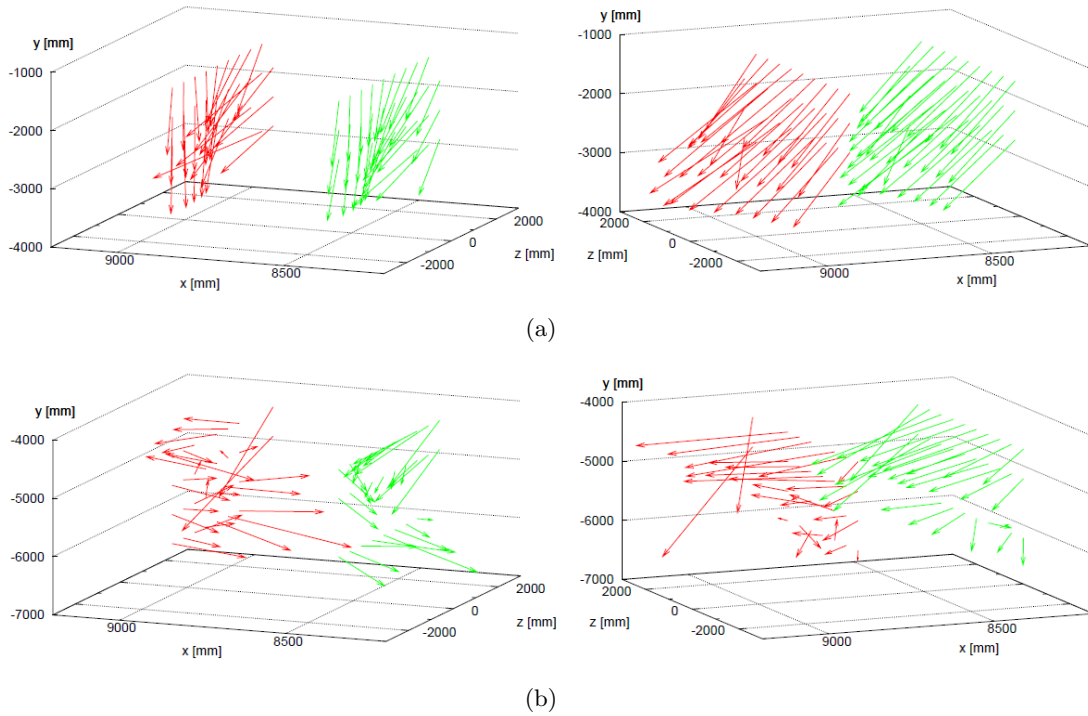


Figure 5.4: Exemplary regions from the magnetic field survey near the spectrometer hall walls. Shown are the field vectors of specific regions from two different viewing angles. The red field vectors are taken 0.5 m from the wall and the green ones 1 m. (a) Region on the ground floor from $z = -2$ m to $z = 2$ m (b) The same for the basement.

In all these places, the magnetic field was recorded with a fluxgate magnetometer using a variable aluminum holding structure shown in figure 5.3. Field values were taken every 0.5 m and in 4 different heights above the floor. Near the walls, the field proved to be highly inhomogeneous. The magnetic materials created a field stronger than the earth's magnetic field up to 0.5 m from the wall. Figure 5.4 shows a representative subset of the magnetic field survey near the wall for visualization. Since it is difficult to show 3D vector fields on a 2D medium, the illustrations contain the same data from two different points of view for a region in the basement and ground floor gallery (Region 2 of figure 5.2). As expected, the homogeneity improves the further from the wall the field is measured. The data in region 3 of 5.2 shows only minimal deviations from the earth's magnetic field in the low μT range. Also, the field inhomogeneity is stronger in the basement, as there is $20 \frac{\text{kg}}{\text{m}^2}$ of ferromagnetic material present in the walls there, opposed to $6 \frac{\text{kg}}{\text{m}^2}$ in the ground floor and above [89].

These field surveys confirmed the expectations of an inhomogeneous field produced by magnetized structural materials, that is present throughout the whole KATRIN experimental hall. Although the field was measured in over 2000 locations, it proved unfeasible to create a dependable field model from those, as the measurement regions were too clustered and too close to the walls and thus oversensitive to small scale effects. Nevertheless, it has been learned from these measurements, that although the near field

structure of the magnetic materials is very complex, the field further from the walls is only slightly influenced. So for a usable field survey, the measurements have to be further from the wall and closer to the main spectrometer [90].

5.1.2 Measurements Inside the Main Spectrometer

To create a robust and accurate model of the magnetic field produced by magnetic materials inside the main spectrometer, measurements near the field sources did not provide reasonable results because local effects dominated the measured magnetic fields. Measurements in the main spectrometer volume itself produced more useful results.

A direct measurement of magnetic field vectors in the central volume of the main spectrometer added directional information to the absolute field strength measurements in [76]. Then, vectorial field measurements near the hull of the vessel around the central volume were a good basis for creating a simulation model for the magnetic materials.

Magnetic Field Measurement in the Central Main Spectrometer Volume

During the commissioning of the air coil system described in section 3.4.1 magnetic fields without any currents in the air coil systems were recorded for many positions. This was necessary to get the pure air coil field but also was a means to its own end. The accurate directional information was a big improvement over the absolute field strength measurements that were possible with photogrammetric position measurements. Figure 5.5 shows the field vectors measured during the air coil commissioning in region (6) of figure 5.2. In this data set, the effective local earth's magnetic field, given by the mean of all measured vectors, has been subtracted. So here, only the inhomogeneous part of the field created by the magnetic materials is shown. This makes sense, since the homogeneous offsets can be compensated by the air coil systems. Only the remaining inhomogeneous part is of interest for the modeling of the magnetic materials field.

The absolute field strength decreases towards the center of the spectrometer and there seem to be some prominent magnetic materials in the upper left and to the right of the plot towards which the field vectors point. These would be sections of the wall armament which are more strongly magnetized, or in which the magnetizations do not cancel each other out as effectively as in other parts. This impression is strengthened by the field measurements on the electrode mounting rails discussed below. There are a few exceptionally large fields near the center surrounded by weaker field values. Small amounts of magnetized normal steel used in the intervention system are the most probably source of this disturbance. As these values are very close to the z-axis, the natural source of such a disturbance would be normal steel in the ball bearing used to turn the intervention system platform.

But aside from these exceptions, the field looks as it is expected and can stand as an example to compare the simulations against. Unfortunately, a quantitative comparison is difficult, as the magnetic materials field is time dependent as will be shown below, and thus measurements to which a simulation model is fitted are from a different situation than this measurement.

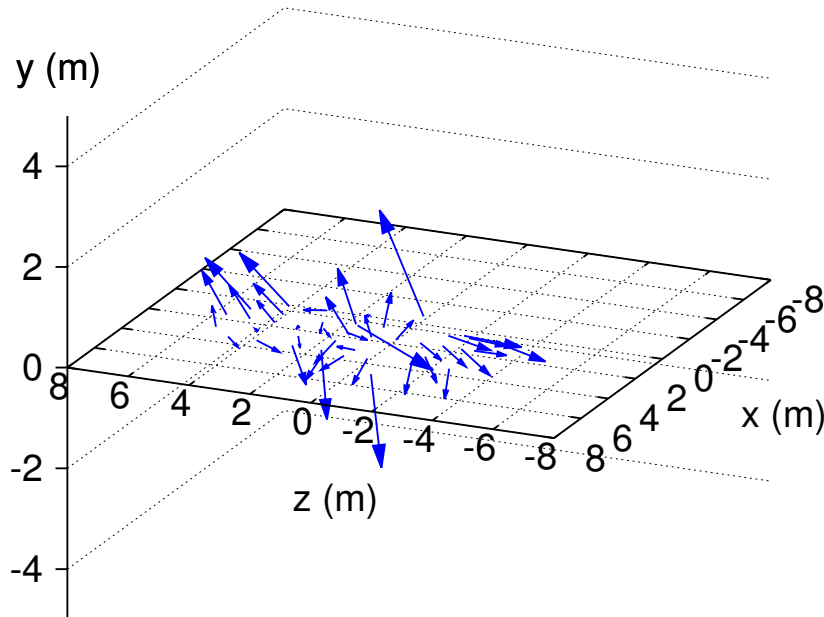


Figure 5.5: Field of the magnetic materials in the main spectrometer: Shown here are the field vectors measured in equatorial plane of the main spectrometer in region (6) of 5.2. The four exceptionally large field vectors near the z-axis are due to magnetic material used in the intervention system. 1 m is equivalent to $0.5 \mu\text{T}$.

Magnetic Field Measurements on the Electrode Holding Structure

Since the field values measured near the wall failed to produce a useful magnetic materials model, the next thing to try were field values further from the wall surrounding the region of interest.

The rail system intended for mounting the electrodes offered the possibility to mount a magnetometer with radial alignment. The mounting shown in figure 5.6 can be moved in azimuthal direction, allowing the field to be measured around the inner volume of the main spectrometer on 20 positions each on 4 rings. Information about the orientation of the magnetometer was obtained by using the radial alignment. This introduces an unknown error, since the mounting structure has a degree of slack and may be tilted on the rails. Another problem are the connections between two rail segments, where the mounting can be misaligned even larger due to missing guiding rails. Nevertheless, the field reconstruction was successful in most locations.

Figure 5.7 shows the reconstructed field of this measurement in relation to the magnetic field values taken in the central volume of the main spectrometer (figure 5.5). The measured field at the main spectrometer hull continues the trends observed in the magnetic field data in the central volume, including the behaviour of the field in the front right and back left parts of the spectrometer. From this measurements the expectations from [89] are confirmed: the influence is largest near the walls, smaller in the basement due to the use of low-magnetic stainless steel and smallest near the wooden ceiling.

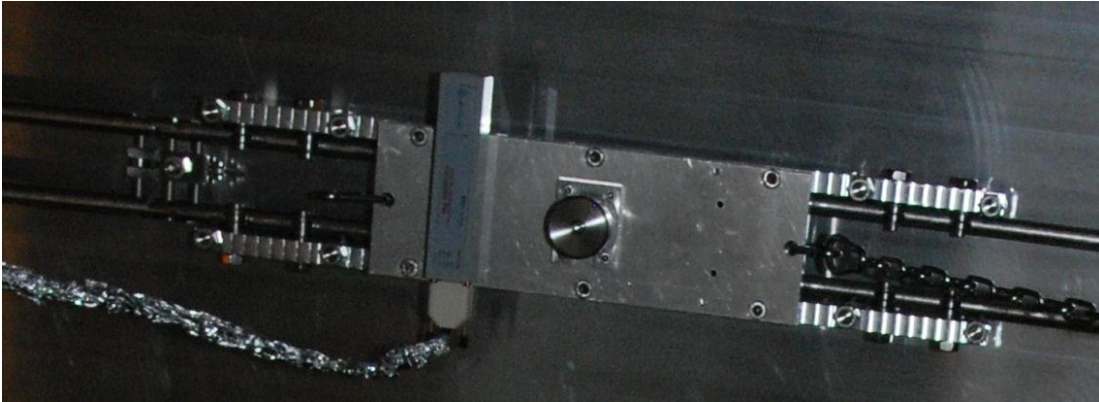


Figure 5.6: Mounting used to measure the magnetic fields around the main spectrometer: The magnetometers y-axis is radially aligned to the spectrometer, the z-axis points in azimuthal direction and the x-axis in axial direction. The positioning is done with photogrammetry.

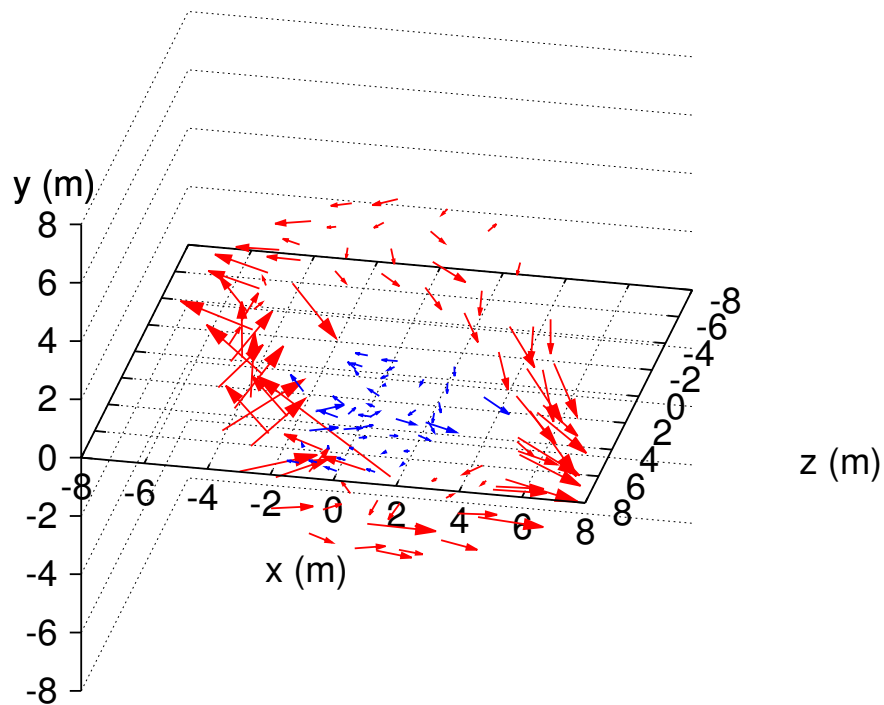


Figure 5.7: Field of the magnetic materials around the main spectrometer: The red field vectors are those measured in region (5) on the electrode rail system near the vessel hull. The blue field vectors are the same as in figure 5.5 in a different scale. In this plot, 1 m is equivalent to $1 \mu\text{T}$.

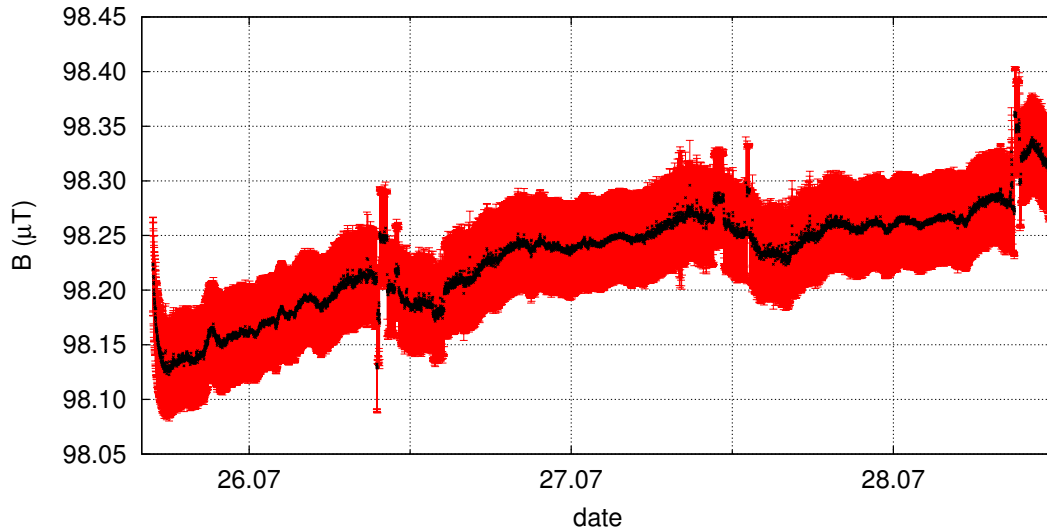


Figure 5.8: Magnetic field time development: The Black crosses are the mean measured field values, the statistical errors are drawn in red. The magnetic field below the detector platform varies over three days about 15 nT. This is well within the intrinsic variations of the earth’s magnetic field itself [91]. The jumps at about 11:00 are most probably man-made.

5.1.3 Time Dependency of the Magnetic Material’s Field

The measurements described in the previous sections show snapshots of the magnetic field. These measurements can be used to implement and refine a process to simulate the magnetic fields. But a time dependence of these fields means that older field values cannot be used to describe the current situations. The most prominent influence on the magnetization of the structural material are the superconducting magnets. To determine the magnitude of their influence, a magnetometer was fixed to the basement wall of the main spectrometer during magnet tests of the detector system and the DPS2-F. The magnetometer took data in 30 s intervals for several days. In these measurements a definite effect of the superconducting magnets was observed, but no otherwise unusual behaviour.

Daily Variations

When no active magnetic sources affect the structural material, the magnetic field at the wall shows variations in the 10 nT range. Figure 5.8 shows the absolute field strength in the basement of the main spectrometer hall directly below the detector platform after the detector magnet system test.

During this time, the magnetic field varied by 15 nT peak-to-peak, discarding the jumps at 11 o’clock which are most probably due to human manipulation of the magnetic conditions on the detector platform. Variations of this order of magnitude are not uncommon in the earth’s magnetic field. So there is no chance to observe a change in the magnetization of structural materials, since it would be covered by fluctuations in the earth’s magnetic field.

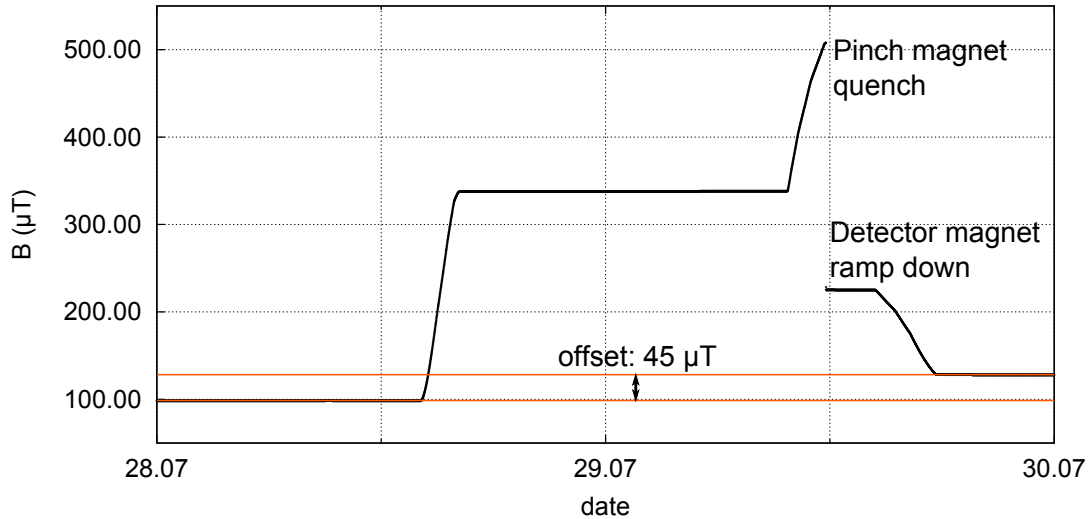


Figure 5.9: Magnetic field below the detector platform during the detector magnet system test. The error bars are too small to be visible and have been omitted. After the magnets have been warmed up again, the magnetization has changed such that the field at the measurement position has increased by $45 \mu\text{T}$.

Influence of Superconducting Magnets

The superconducting magnets on the other hand have a definite influence on the magnetization of the materials. Figure 5.9 shows the field in the basement beneath the detector platform during the test of the detector magnet system. While ramping both magnets simultaneously, the pinch magnet quenched and the detector magnet had also to be ramped down. But although the magnets were not at full field a definite change in the field offset by $45 \mu\text{T}$ has been observed. This is an increase in field strength by almost 50 % directly at the basement wall. With farther distance from this field source, the effect will be smaller. But since there are also superconducting magnets elsewhere in the KATRIN experiment the influence on the overall field of the magnetic materials after magnetic cycles will not be negligible. Figure 5.10 shows a similar measurement below the pre-spectrometer platform during and after a test of the DPS2-F magnets. As they are a few meters further from the measurement site, than the detector field measurement, the effect is smaller but clearly visible. The field after the magnet test behaves very similarly than in figure 5.8.

This set of measurements shows that in order to obtain a valid description of the magnetic materials, up-to-date magnetic field values are needed. So the magnetic materials model should be updated at least after each magnet operation.

5.2 Representation in Simulations

The magnetic field in the analyzing plane is of great importance to the analysis of KATRIN data. Since direct measurements of the magnetic field inside the main spectrometer are no longer possible, this field has to be calculated in a reliable way by

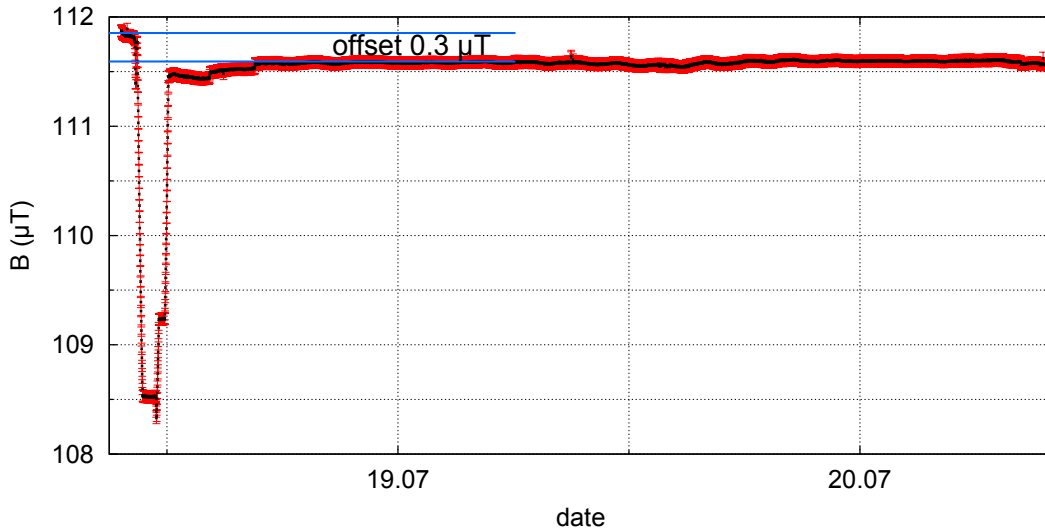


Figure 5.10: Magnetic field below the pre spectrometer platform during and after a DPS2-F magnet test. Again, black are the mean values, red the statistical errors. Due to the greater distance to the magnets, the offset change in the magnetic field is much smaller than in 5.9, about $0.3 \mu\text{T}$, but still at least one order of magnitude larger than the earth's magnetic field's variations.

simulations. The field of the superconducting magnets is easily computed and as shown above, the air coil systems are also very well understood. The remaining undetermined contribution to the magnetic field comes from the magnetic materials. Since the bulk of the steel reinforcement is far from the superconducting magnets, the induced magnetization of the material can be assumed to be negligible. The remanent magnetization can then be described by the magnetic dipole model detailed in 4.2.4. In the section at hand it will be shown how a complete model of the magnetic materials in the main spectrometer hall for field calculations inside the main spectrometer can be obtained from measurements outside the vacuum vessel.

5.2.1 Dipole Distribution Method

It is a reasonable assumption to place the magnetic dipoles in the simulation in the area where magnetic material is situated, in the walls and basement of the main spectrometer hall. The detailed distribution of the single steel bars is unknown and as it turns out, the quality of the magnetic materials model highly depends on the spacing between dipoles and to a lesser extent on the size of dipole length as will be shown below in more detail. To account for this dependency in the process of creating a dipole model, the geometry will be varied in dipole spacing as well as length. For example, the distance between the centers of neighbouring dipoles is varied from 5 to 2 m. These are distributed in a rectangular grid at the position of the eastern and western walls. At each grid point a dipole in z and one in y direction is placed. For each of these setups, the dipole length is varied from half the distance between dipole centers and $\frac{1}{10}$ th of that distance. Figure 5.11 shows such a parameter space.

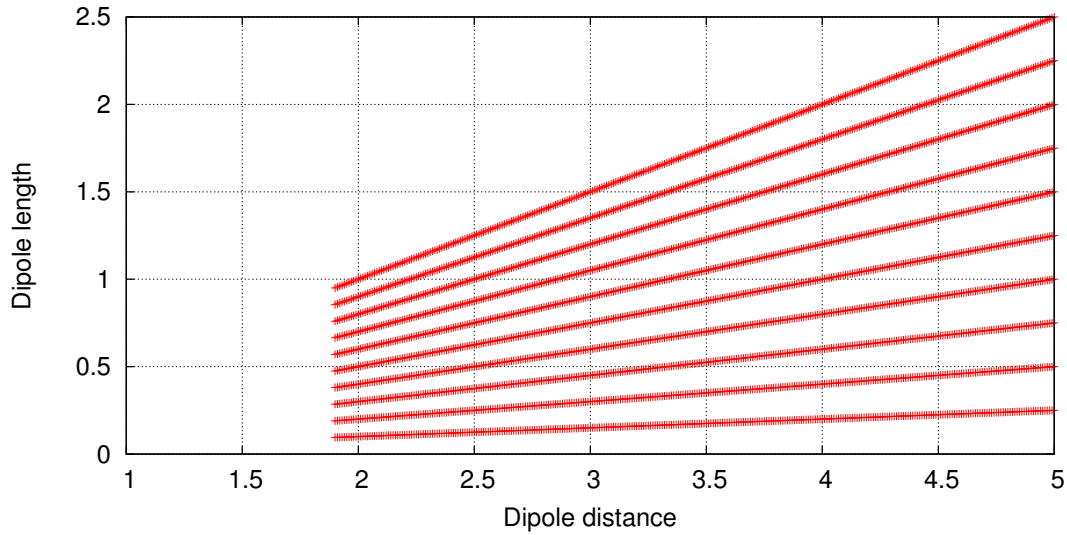


Figure 5.11: Variation of dipole geometry: The dipoles are distributed across the same area in different distances and length. This varies the number of dipoles as well as the overall structure.

For each of these models, the dipole strength will be fitted to best describe the measured magnetic field data. Then the resulting simulated field will be compared to measured field values. The dipole geometry giving the best results will then be saved to use in simulations. If the measured field points are spread across the area of interest this may also be the data used to fit the dipole strengths.

5.2.2 Fit to Measured Data

The fitting of the dipole strengths to the measured magnetic field values is done by a least squares fit algorithm. The equation for the magnetic field of a magnetic dipoles 4.13 for a dipole simulation is the sum over i dipoles with magnetization m_i . The dipoles are described by two monopoles as detailed in chapter 4.2.4:

$$B_{kj} = \sum_{i=1}^N \mu_0 \cdot r_b^2 \cdot \frac{m_i}{4} \cdot \left(-\frac{(\widehat{r_{i1} - x_k})_j}{(r_{i1} - x_k)_j^2} + \frac{(\widehat{r_{i2} - x_k})_j}{(r_{i2} - x_k)_j^2} \right) \quad (5.2)$$

with B_k the k-th Field component value

x is the position of the field value

r_b is the radius of a dipole bar

m_i the magnetization of the i-th dipole

r_{i1} and r_{i2} are the starting and ending point of the i-th dipole

j denotes whether it is a x-,y- or z- component

In the following, N will be the total number of dipoles and K the total number of measured field components.

From 5.2 an equation system for $B(m)$ can be written as follows:

$$B_k \approx \sum_{i=1}^N m_i \cdot c_{ki} \quad (5.3)$$

or

$$\vec{B} \approx c \cdot \vec{m} \quad (5.4)$$

to find the optimal values for the magnetizations the function

$$f(m_1, m_2, \dots, m_N) \approx \sum_{k=1}^K \left(B_k - \sum_{i=1}^N m_i \cdot c_{ki} \right)^2 \quad (5.5)$$

needs to be minimized. This means:

$$\begin{aligned} \partial_i f &= -2 \sum_{k=1}^K \left(B_k - \sum_{j=1}^N m_j \cdot c_{kj} \right) \cdot c_{ki} = 0 \\ \Rightarrow \sum_{k=1}^K \left(B_k \cdot c_{ki} - \sum_{j=1}^N m_j \cdot c_{kj} \cdot c_{ki} \right) &= 0 \quad \forall i \end{aligned} \quad (5.6)$$

from this the following linear equation system is formed

$$\vec{a} = A \cdot \vec{m} \quad (5.7)$$

with the i -dimensional vector a ,

$$a_i = \sum_{k=1}^K (B_k \cdot c_{ki}) \quad (5.8)$$

the quadratic $i \times i$ matrix A

$$A_{ij} = \sum_{k=1}^K (c_{ki} \cdot c_{kj}) \quad (5.9)$$

and the magnetization vector \vec{m} .

Solving this linear equation system yields the magnetization values which fit best the measured data in a given dipole geometry.

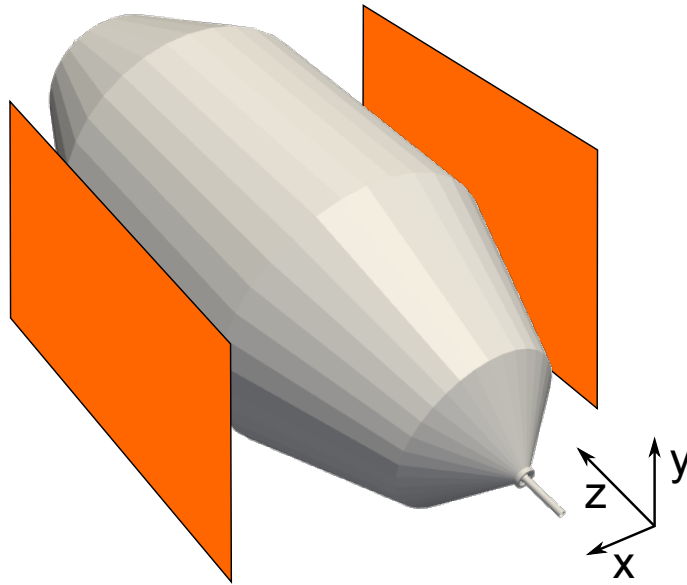


Figure 5.12: Regions for Dipole placement at the main spectrometer: For the fit test, dipoles were placed at $x = \pm 10$ m, $y = \pm 6$ m and $z = \pm 10$ m. These regions are marked in orange. There, different dipole geometries with varying distances between dipoles and dipole lengths were calculated.

5.2.3 Results

To judge the quality of the simulation, two methods have been implemented. The first is to set a tolerance limit on the absolute field strength ratio and the angular difference between measured and simulated values. Complementary to that the mean values of field strength ratio and angle difference can be recorded for each dipole distribution.

Optimal Dipole Parameters

For the first demonstration of the dipole distribution method, the magnetic field measurement on the electrode holding structure described in 5.1.2, figure 5.7 have been used. The dipole number is limited by the number of measured magnetic field values to keep the linear equation system 5.7 solvable. To the measured values, additional field values have been linearly interpolated to increase the number of available field values. This does introduce a degree of error, but as this serves only as a proof of principle this can be tolerated.

Dipoles in y and z direction were placed in the orange regions of figure 5.12 at $x = \pm 10$ m. The best dipole distribution has been chosen based on the limit method. The magnetic fields of this dipole distribution with the optimal distance and length was compared to the measured and interpolated fields. As limits 10 % on the absolute field difference and 15° for the angle were chosen. The dipole distribution in which the simulated field coincided with the measured field within these limits on the highest count of positions was then chosen as final result. As a check, the mean values of field ratio and angle difference were also recorded.

In this run, a total number of 272 magnetic field vectors were used to fit the dipole strengths and compare the magnetic field values. Figure 5.13 shows the number of

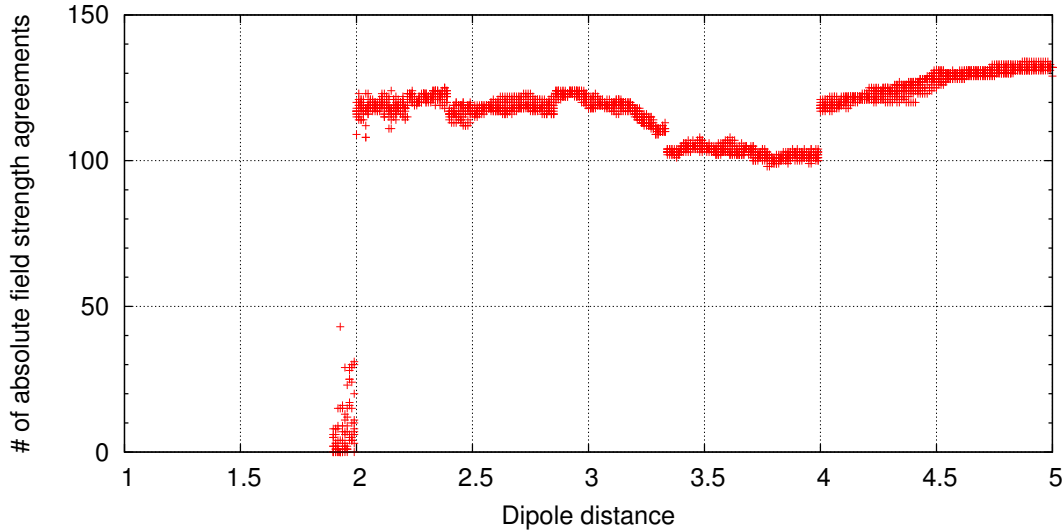


Figure 5.13: Field strength agreements for dipole simulations: The limit was set to 10 %, fields were compared at 272 points. For each distance between dipoles, the number of absolute magnetic field agreements of the ten different dipole lengths is marked. The maximal number of agreements was 134 at dipole distances from 4.90 m and dipole length of 1.96 m to 4.87 m distance and 1.704 m length.

field strength agreements depending on the distance between dipoles. At each dipole distance value, values for each of the 10 dipole lengths are marked. Here it becomes clear that the dipole length has no great influence on the quality of the model. In figure 5.14 the same data set is plotted with the number of angle agreements on the y-axis. Finally, figure 5.15 shows the number of points with simultaneous absolute field strength and angle difference agreement. Again, the dipole length makes only a minimal difference in the tested parameter space. In all cases, the fit breaks down below 2 m. In this parameter region the number of dipoles is too large for the equation system to be solvable. For the best dipole distribution parameters in this simulation a dipole distance of 3.14 m and a dipole length 0.628 m.

The mean values for this simulation show no clear minimum, as both mean absolute field ratio and mean angle difference slightly improve with smaller distances between dipoles up until the point where the fit breaks down. This excludes them for use a direct quality criterium. But combined with the number of field agreements this information is still valuable. For a field strength ratio between measurement and simulation of 1.2 about half the field strengths agree within 10 %. And for the angular mean of $22^\circ - 28^\circ$ more than half the angle differences are smaller than 15° . This means that a few larger ratio and angle differences are outweighed by the closer values. For the mean values, the best parameters were dipole distance 2.22 m and length 0.999 m with a mean angle of 22.6° and a mean ratio of 1.13.

Field of the Fitted Dipole Distribution

With the acquired dipole distribution, the magnetic field of the structural material near the KATRIN main spectrometer can be calculated. The direct comparison to the

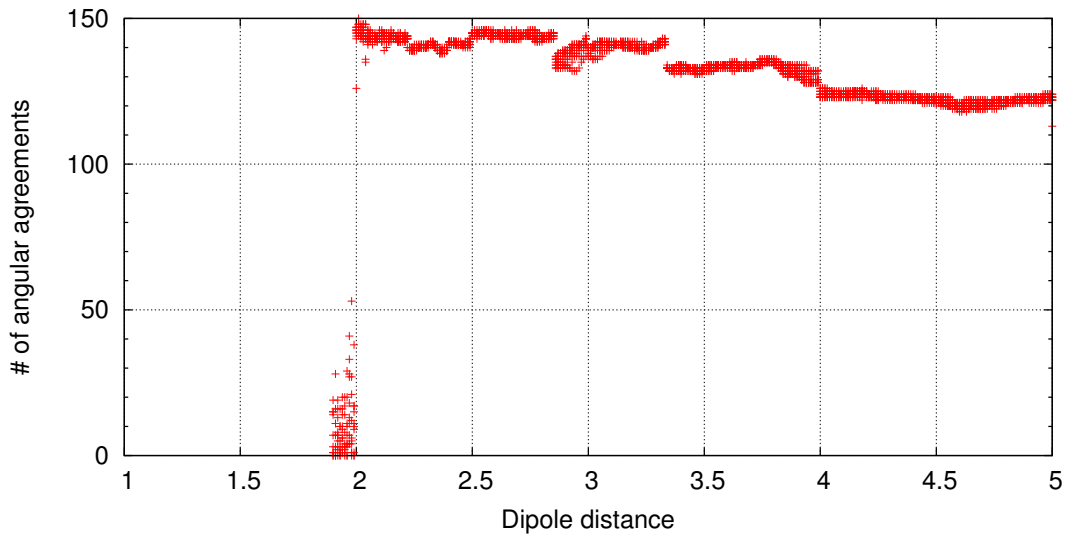


Figure 5.14: Angular agreements for dipole simulations: Same as figure 5.13 with the number of angular agreements on the y-axis. The maximal number of agreements was 150 at a dipole distance of 2.01 m and a dipole length of 0.9045 m.

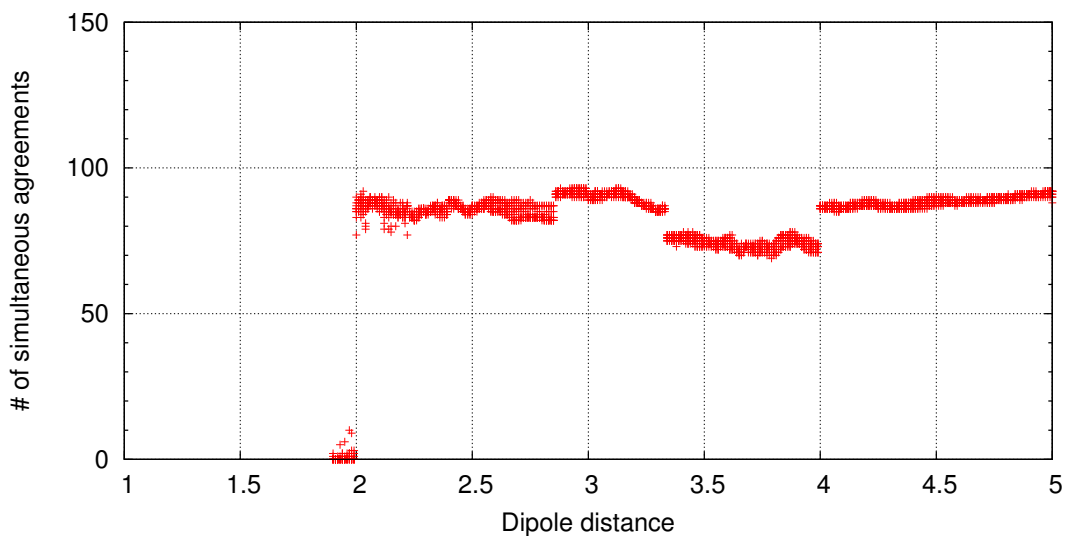


Figure 5.15: Simultaneous angular and field strength agreements for dipole simulations. The number of simultaneous agreements is dominated by the absolute field agreement but the large-distance parameters are suppressed by the angular requirements. The optimal parameters from this simulation are dipole distance 3.14 m and dipole length 0.628 m.

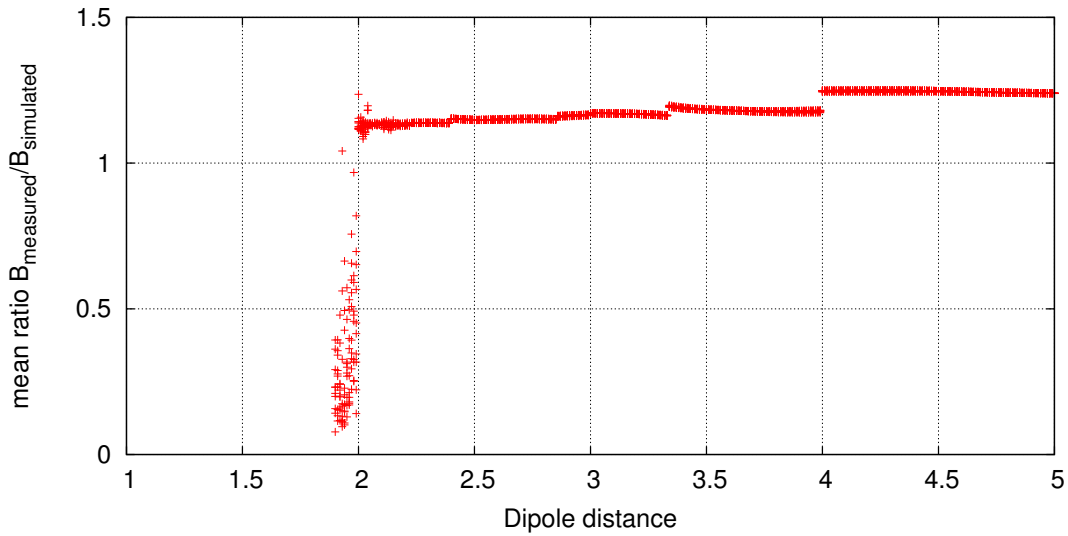


Figure 5.16: Mean ratio dependence of dipole strength fits: The mean ratio between measured and simulated field strength gets closer to 1 with lower dipole distances until the fit breaks down. Here, the data depends even less on the dipole length than in the limit method.

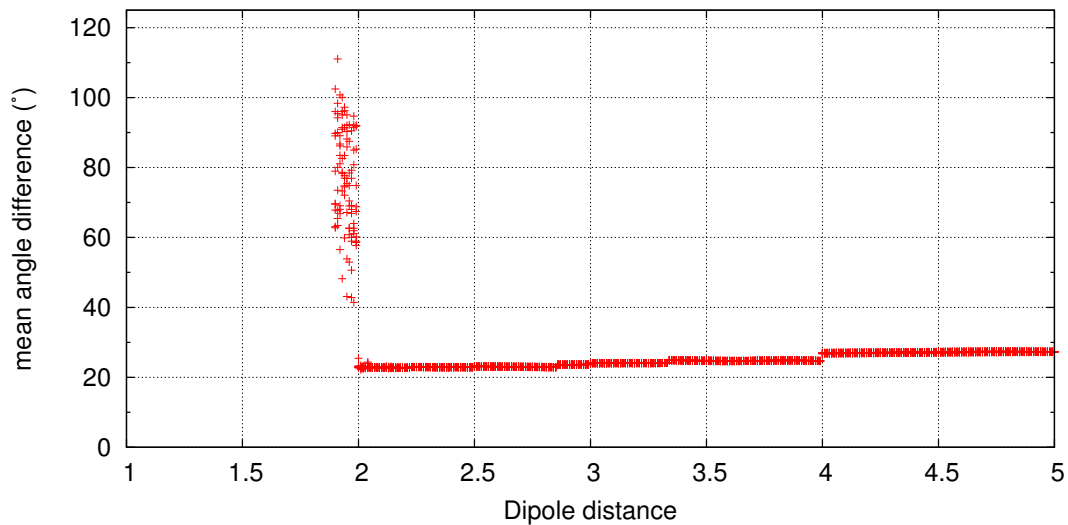


Figure 5.17: Mean angle difference dependence of dipole strength fits: Similar to the mean ratio, the mean angle difference is better with lower dipole distances. Again, the dipole length has little influence.

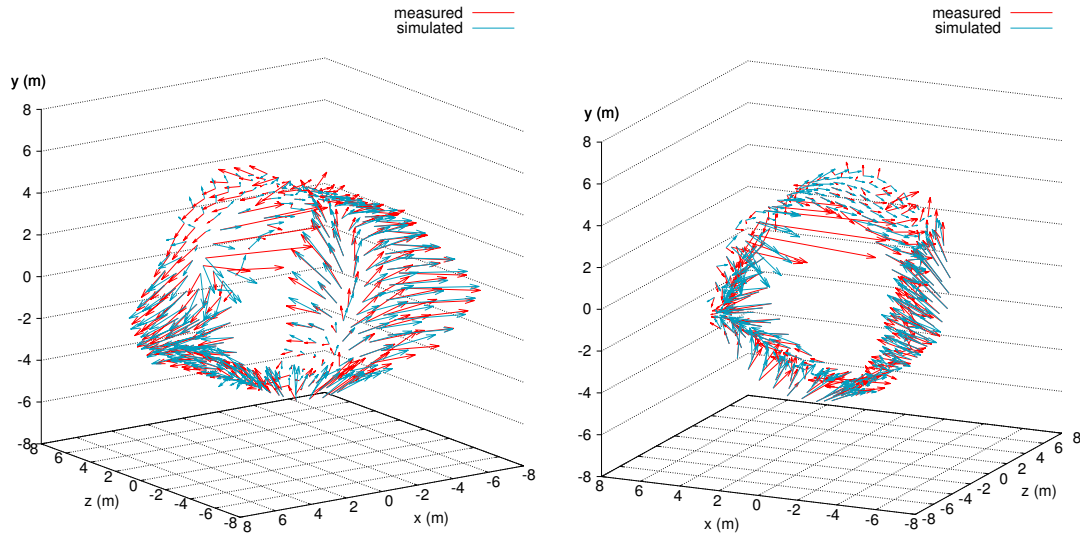


Figure 5.18: Comparison between measured and simulated field of magnetic materials. Shown here are the measured and interpolated field vectors in red and the simulated field vectors at the same positions in blue. Due to the limitations of a 2D medium, the same data is plotted from different viewing angles in the left and right part. Apart from the obvious measurement and interpolation errors in the top left part, the simulated values differ strongly only in the low field parts around $x = 0$. Otherwise, the simulated field is a good approximation of the real magnetic field situation.

measured values in figure 5.18 shows a very good agreement between the measured and simulated field structure. The largest deviations are measurement errors and interpolation artifacts in the upper left corner. In the regions around $z = 0$, farthest away from the magnetic materials, the field is lowest. There, even small absolute variations of the simulated fields cause large relative deviations from the measurement. This accounts for most of the angular differences above the set limit. For further insight into the absolute differences in the field, figure 5.19 shows the difference vectors between measured and simulated field. This data gives the definite confirmation that the magnetic field is well represented in regions where it is strong. Only low field regions which have little influence on the overall field are less well represented.

With the constructed field model at hand it is possible to calculate the magnetic field at any position. Figure 5.20 shows the absolute strength of the simulated magnetic materials field in the x - z -plane at $y = 0$. In the outer regions, the simulated field strength rises very rapidly. It is an experimentally verified fact that the actual magnetic field of the structural materials in the hall is only a few tens of μT . So outside a $10\text{ m} \times 10\text{ m} \times 10\text{ m}$ cube with its center at the origin, the magnetic materials field simulation is not applicable. Fortunately, the central part of the main spectrometer is enclosed in this cube. Figure 5.21 shows the absolute field strength for this region at $y = 0$. It shows no strong gradients inside the main spectrometer region. It can be noted that the unrealistic field characteristics appear only outside the volume which was enclosed by magnetic field measurements.

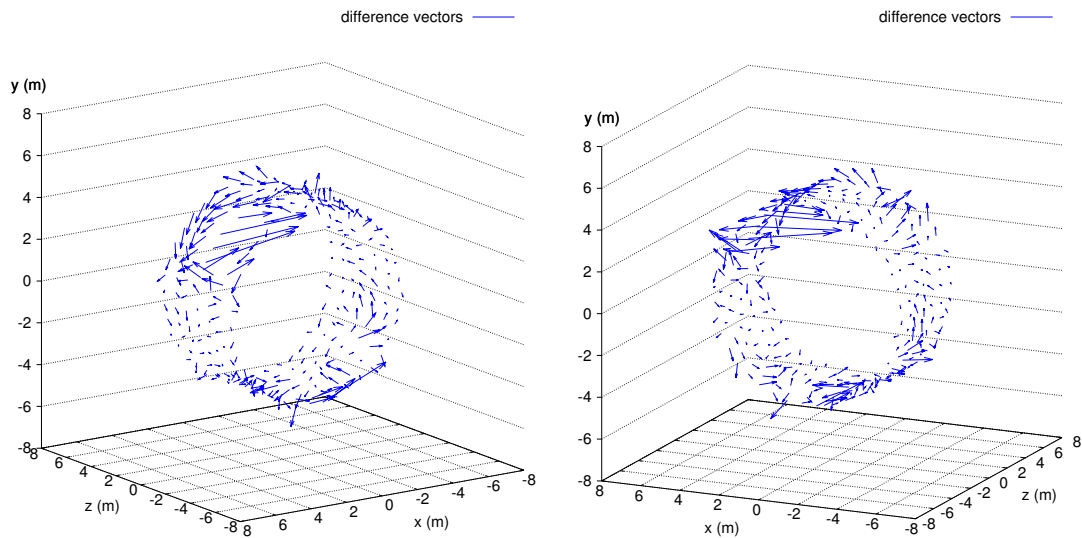
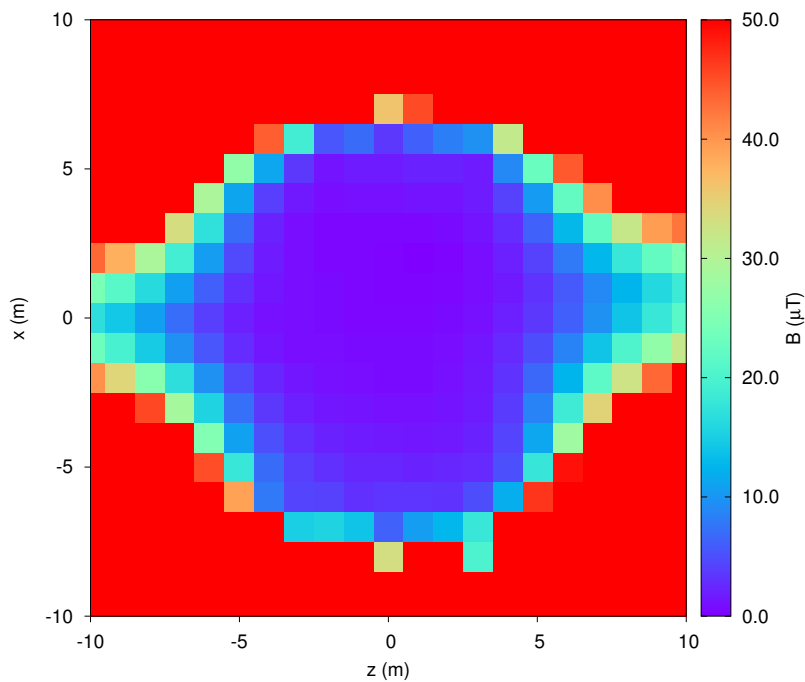


Figure 5.19: Difference vectors between measured and simulated field of magnetic materials. As in figure 5.18 the data is shown from two different angles. Disregarding the measurement errors, the largest difference occur in the region of low fields at the top and bottom, where the absolute fields are lowest.

Figure 5.20: Simulated magnetic materials field in the equatorial plane. The Field is shown in the area $-10 \text{ m} < x < 10 \text{ m}$, $-10 \text{ m} < z < 10 \text{ m}$. More than 5 m away from the center in each direction, the field becomes unphysically large. Within this region, the simulation is an adequate representation of the actual magnetic field.



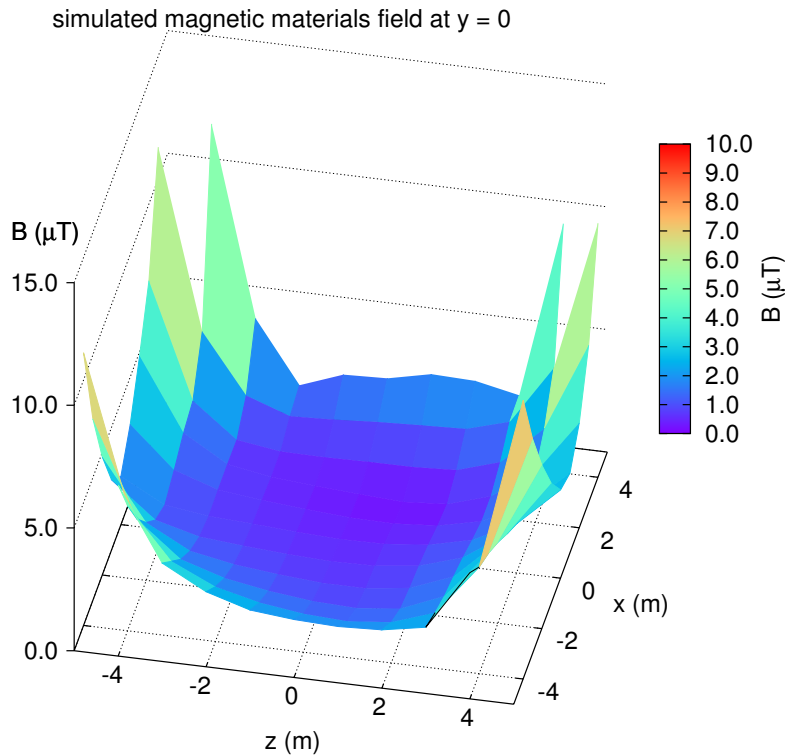


Figure 5.21: Simulated magnetic materials field in the central part of the equatorial plane. In this area, the field shows no strong gradients and a very good approximation of the actual magnetic field.

5.3 Summary

Concerning the magnetic field of structural materials, a large number of magnetic field measurements have been performed. The measurements near the walls close to the field sources show that the magnetic field there is highly inhomogeneous and has a complex structure. Further from these walls this field is smoother as more field sources contribute to the overall field. More than 1 m from the walls, this field is completely dominated by the earth's magnetic field and the magnetic materials impose only a small inhomogeneity.

Inside the main spectrometer, the field has also been measured with very good spatial and directional resolution. This measurement confirms that the earth's magnetic field is the dominant contribution. Subtracting the mean field vector from the measured magnetic field as an effective earth's magnetic field gives the field of the magnetic materials. This is sensible, since a homogeneous offset field can be compensated by the EMCS, whether it comes from the earth's magnetic field or the magnetic materials. The remaining inhomogeneous magnetic materials field is weakest in the center of the spectrometer, farthest from the magnetic materials, and converges to a few distinct points on the front right and back left of figure 5.18.

To represent the field of the magnetic materials in simulations, a variety of dipole distributions is created and the dipole strengths are fitted to measured data. The distribution with the best results can then be used e.g. in particle tracking simulations. With a data set created from measurements around the inside of the main spectrometer

vessel it was possible to successfully create a dipole distribution which represents the actual magnetic situation very well. This field model is valid in the volume enclosed by measurement points. For further field models, a magnetic monitoring system with the ability to measure a great number of magnetic field values around the volume of interest will be advantageous.

Lastly, the background field in the main spectrometer shows a time dependent behaviour. The earth's magnetic field varies due to secular variation on very long time scales, but is also varied by solar activity with a few 10s of nT on a scale of hours. Furthermore, magnetic materials are influenced by the strong superconducting magnets. Changing the magnetic configuration of the experimental setup will inevitably have an effect on the magnetization. After such a change in the magnetic setup, a new dipole field model will have to be created to describe the new situation accurately. To monitor the quality of the magnetic field model, a permanent magnetic monitoring system is currently under development and construction at the KATRIN main spectrometer. This system will observe the magnetic field at representative points around the main spectrometer. When this system detects a deviation between the field model and the actual magnetic field the simulation will be updated. This system will be discussed in chapter 7 along with a system to automatically collect magnetic field data for creating a dipole model.

6. Simulations of Transmission Properties and Background with Realistic Magnetic Fields

The magnetic field of the MAC-E filter setup in the KATRIN main spectrometer is designed to adiabatically guide signal electrons in a well defined way and shield against background. The discreteness and deformation of the air coil systems and the magnetized structural materials introduce deviations from this design reference. These deviations are measured, well understood and accounted for in field simulations. In this chapter, the effects of these realistic fields on particle trajectories will be discussed.

The altered magnetic field influences the transmission properties of the spectrometer. Since the electrostatic potential is homogeneous in the central volume of the spectrometer, the magnetic field is the determining factor for transmission as discussed in section 3.2. Section 6.1 describes Monte-Carlo simulations of electron transmission properties with ideal magnetic field, a realistic air coil system setup and magnetic materials.

In addition to altering the transmission properties of the spectrometer, the additional fields introduce a non-axially symmetric component in the magnetic field. Such a component might allow background electrons to enter the flux tube and will also effect the storage conditions for charged particles. These effects will be discussed in section 6.2.

6.1 Transmission Studies

In this section, the transmission properties of three different magnetic field setups will be discussed. The first setup is an ideal KATRIN main spectrometer setup as it is planned for the test measurements during the commissioning phase. In the second setup, the gravitational deformation of the LFCS and the discreteness of the LFCS is taken into account (see chapter 3). The last setup also includes the field of magnetic materials (see chapter 5). The differences in magnetic field will be discussed in the next section. Following that, the results of Monte-Carlo particle tracking simulations to examine the transmission function will be presented.

It is very important to know if the magnetic inhomogeneities have an adverse effect on the KATRIN setup, as countermeasures like de-magnetizing the main spectrometer hall are costly and time-consuming. But as the relative field deviations are small and well known, such drastic measures are probably not required.

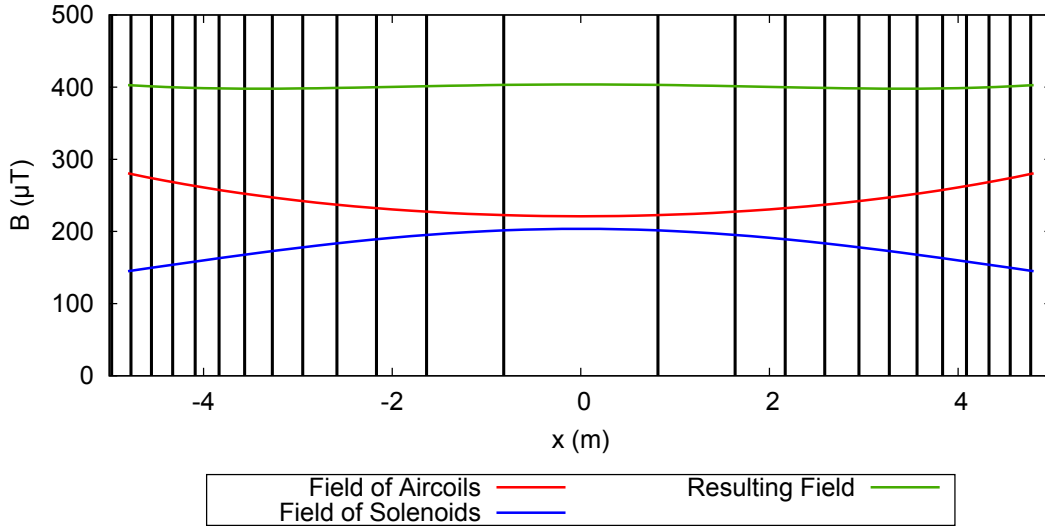


Figure 6.1: Magnetic field on the x-Axis in the Analyzing plane. The blue curve shows the field of the solenoids, the red curve shows the field of the aircoil system. The combined field is drawn in dark green. The vertical bars show the areas of the analyzing plane that are mapped on a pixel ring on the detector. This subdividing significantly reduces the already low magnetic field uncertainty in one pixel by a factor of more than 10 with respect to the uncertainty across the whole analyzing plane. This field is already calculated with the deformed air coil system.

6.1.1 Magnetic Field in the Analyzing Plane

The magnetic field in the analyzing plane is important for the transmission conditions. It has some intrinsic variations, but to minimize the field uncertainty for analysis, the detector is segmented. So each pixel has a much smaller ΔB than the overall analyzing plane. Figure 6.1 shows a cross section over the x-axis in the analyzing plane in magnetic field. The area mapped to the pixel rings are indicated by the black lines. The maximal ΔB in this optimized setup is $\approx 0.5 \mu\text{T}$.

Figure 6.2 shows the changes in magnetic field from the magnetic materials. The absolute field strength variation of the background field is a factor of 5 lower than the intrinsic inhomogeneities. The vectorially added magnetic field varies even less. But still there is a clear change in magnetic field and the radial symmetry is broken.

Information about the magnetic field in the whole analysis plane is also readily available. The field variations are at a μT level throughout the analyzing plane. Figure 6.3 shows the field variations introduced by the deformation of the air coil system and the magnetic materials in the x-y plane at $z = 0$. The realistic air coil system produces a constant offset, with respect to the ideal system, due to slightly different coil radii. Inhomogeneities occur mostly in the regions near the spectrometer hull. The magnetic materials produce a more inhomogeneous field with larger variations. At large radii the field exceeds $5 \mu\text{T}$ in some regions far from the analyzing plane, this is about 1 % of the total magnetic field. These altered magnetic fields produce different transmission properties as well as shielding and storage conditions than the ideal field setup.

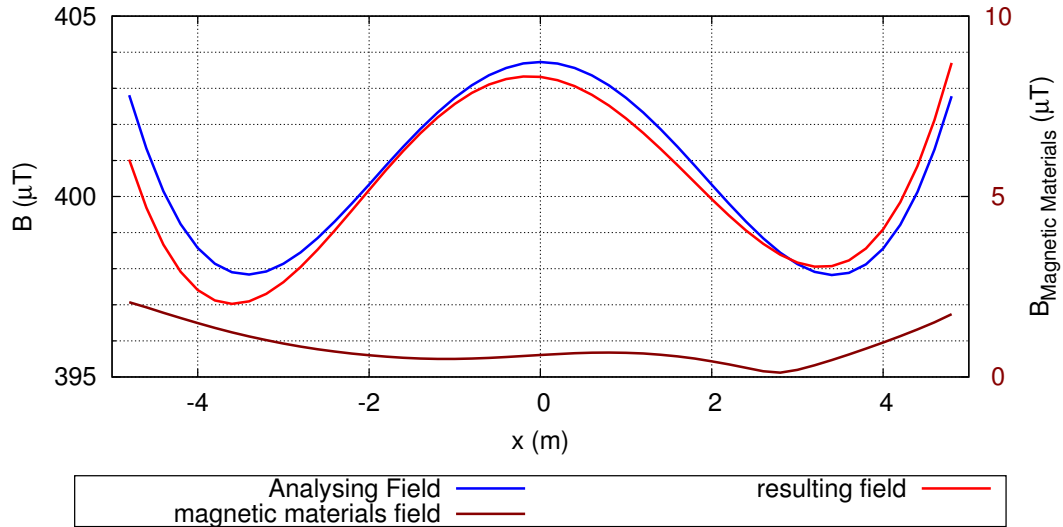


Figure 6.2: Magnetic field changes on the x-axis of the analyzing plane. The blue curve is the combined field of solenoids and realistic air coil system. The brown curve is the field of the magnetic materials. Its strength is shown on the axis to the right. The red curve is the resulting field. Note that both vertical axes have the same dynamic range of $10 \mu\text{T}$.

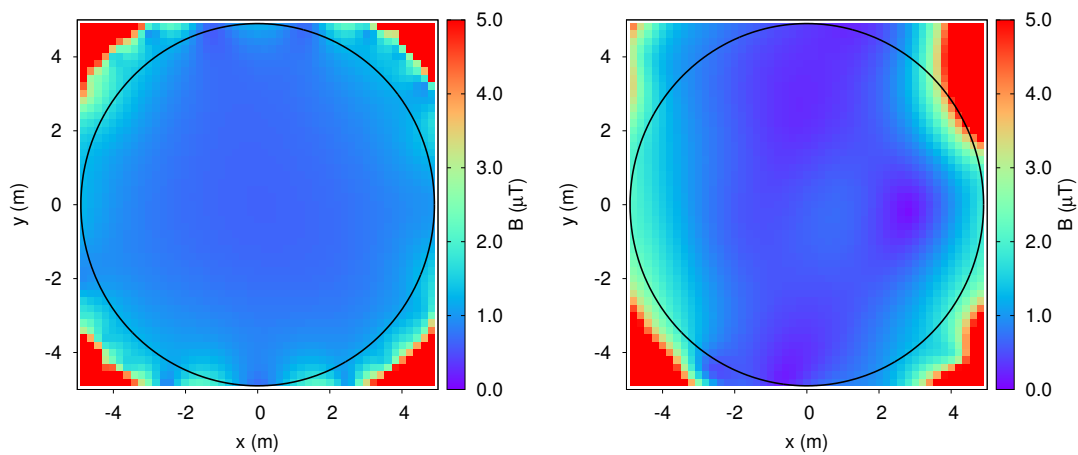


Figure 6.3: Magnetic field changes in the analyzing plane. **left:** Absolute value of the vectorial difference between ideal and realistic air coil fields. **right:** Field of the magnetic materials. The black circle shows the boundaries of the main spectrometer vessel.

6.1.2 Monte-Carlo Particle Tracking Simulations

Monte-Carlo simulations of particle propagations through the main spectrometer offer a very nice tool to investigate the effect of the magnetic field changes on transmission properties. For this particular problem, three different setups have been simulated:

- Setup 1: Solenoid field + ideal LFCS field + earth's magnetic field z-component
- Setup 2: Solenoid field + realistic LFCS and EMCS field + earth's magnetic field
- Setup 3: Solenoid field + realistic LFCS and EMCS field + earth's magnetic field + magnetic materials

The solenoid field has been calculated with the Legendre polynomial expansion. The exact calculation of the air coils with the Biot-Savart method would have taken very long and the time required for one simulation run would have exceeded one week. So to reduce computation time they were instead calculated with the Hermite-polynomial interpolation. The earth's magnetic field was handled by a constant offset and the magnetic materials field was calculated with the dipole method using the distribution derived in chapter 5. The electrostatic setup was the same in all cases.

The particles were started in the pre-spectrometer-side magnet of the main spectrometer with an angular distribution reflecting an isotropic angular distribution in the tritium source. Their starting energies were between 18586 eV and 18588 eV in 0.1 eV intervals. For each simulation run, 10000 electrons were created from the same random seed. This guarantees that different runs are directly comparable.

For each setup one simulation run was done with the electrons starting on-axis and on $x = \pm 2$ cm and $y = \pm 2$ cm.

To evaluate these simulations, the transmission function (2.17) needs to be modified. Since the particle tracking started in the pre-spectrometer magnet, the angular distribution is no longer isotropic and (2.17) becomes:

$$T(E_{\text{start}}, qU) = \frac{1 - \sqrt{1 - \frac{E_{\text{start}} + q(U_{\text{start}} - U_a) \frac{|\vec{B}_{\text{start}}|}{|\vec{B}_a|}}{E_{\text{start}}}}}{1 - \sqrt{1 - \frac{|\vec{B}_{\text{start}}|}{|\vec{B}_{\text{max}}|}}} \quad (6.1)$$

which is valid in $0 \leq q(U_{\text{start}} - U_a) \leq \frac{|\vec{B}_{\text{start}}|}{|\vec{B}_{\text{max}}|} \cdot E_{\text{start}}$. In each simulation, the magnetic field and electric potential at the starting point and the point of minimal longitudinal energy are extracted. From these parameters, the transmission function for each setup is calculated. As this is a basic counting data analysis, the error on each absolute number of transmitted electrons is the square root of the transmitted number. To compare with the transmission function, the absolute numbers are normalized to 1 by dividing through the maximum number of transmitted electrons. The relative errors are translated directly into the error of the transmission rate.

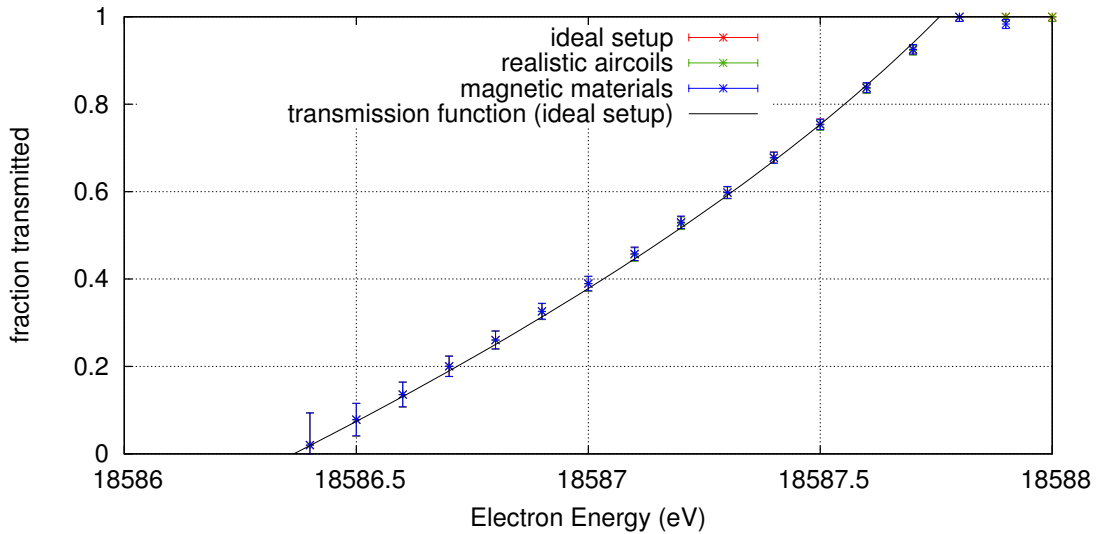


Figure 6.4: On-axis transmission simulation: For the central starting position, the different magnetic field setups make no statistically significant difference in the transmission rate. The calculated transmission function for the field parameters in the ideal setup simulation describes all setups.

Figure 6.4 shows the simulation results for the on-axis position. The electrons traversing the different magnetic field setups do not show any different behaviour. For this central starting point, the differences in magnetic field are small and the ideal transmission function describes all setups equally well.

Off-axis, the situation is similar. For example for the starting point at $x = -2$ cm and $y = 0$ cm. As figure 6.5 shows, the electron transmission rates in this starting point vary slightly but are not significantly different from each other. Although the transmission rates with the magnetic materials setup are systematically higher than in the ideal and realistic aircoil setup, the difference is not in a significant range. But since the transmission function with the ideal parameters is below the data points for most of the energy range, it describes the actual spectrometer situation with deformed air coils and magnetic materials worse than an updated function, although the difference is minimal and would not be visible in the plot at this size. The depiction is therefore omitted.

Instead, figure 6.6 shows the transmission rates and transmission functions for the different starting positions with the magnetic materials setup. There is a clear difference between the transmission properties on- and off-axis. This is not surprising, as figure 6.2 shows, the magnetic field depends on the radius, as well as the electric potential. It also shows that for the magnetic materials setup the field is no longer radially symmetric. This leads to different transmission properties at the same radius for different starting positions. In fact, the largest differences between the simulated setups are larger than the statistical errors. For better visualization, figure 6.7 shows a zoom-in of figure 6.6. In this depiction, the difference in transmission rates at the same starting radius is visible, as are the corresponding transmission functions. Since the KATRIN detector

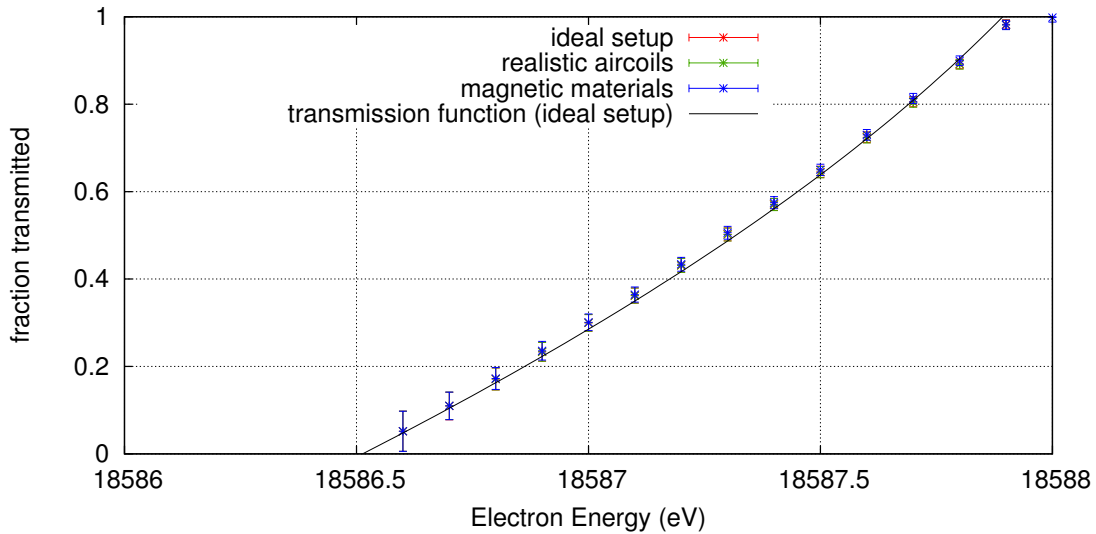


Figure 6.5: Off-axis transmission simulation: Electrons are starting at $x = \pm 2$ cm and $y = \pm 2$ cm in the pre-spectrometer magnet. The blue data of the magnetic materials setup show slightly larger transmission rates throughout the energy range. The plotted transmission function for the ideal setup therefore is a slightly worse description of the actual situation.

has several pixels at each radius, this information is of value for the analysis of actual data during commissioning of the main spectrometer and neutrino mass measurements with the KATRIN experiment.

6.2 Background Studies

Transmission is not the only spectrometer property influenced by the magnetic field. Electrons that are created at the spectrometer surface by cosmic muons or radioactivity in the environment are deflected back to the hull by the Lorentz-force. This mechanism requires an axially symmetric field and loses efficiency if this symmetry is disturbed. On the other hand, if a radioactive isotope decays in the spectrometer, it produces electrons in the inner volume that may be guided directly to the detector. Or worse, they may be trapped in the spectrometer by the magnetic mirrors at its entrance and exit and produce more secondary electrons by scattering with residual gas molecules. These are then guided to the detector and contribute to the background. The most prominent of these radioactive isotopes is ^{219}Ra emanating from the non-evaporating getter pumps [63].

6.2.1 Electron Drift Forces

The forces causing electrons to enter the flux tube that is imaged on the detector depend on the electric and magnetic fields. In the following, \mathcal{E} will be the electric field

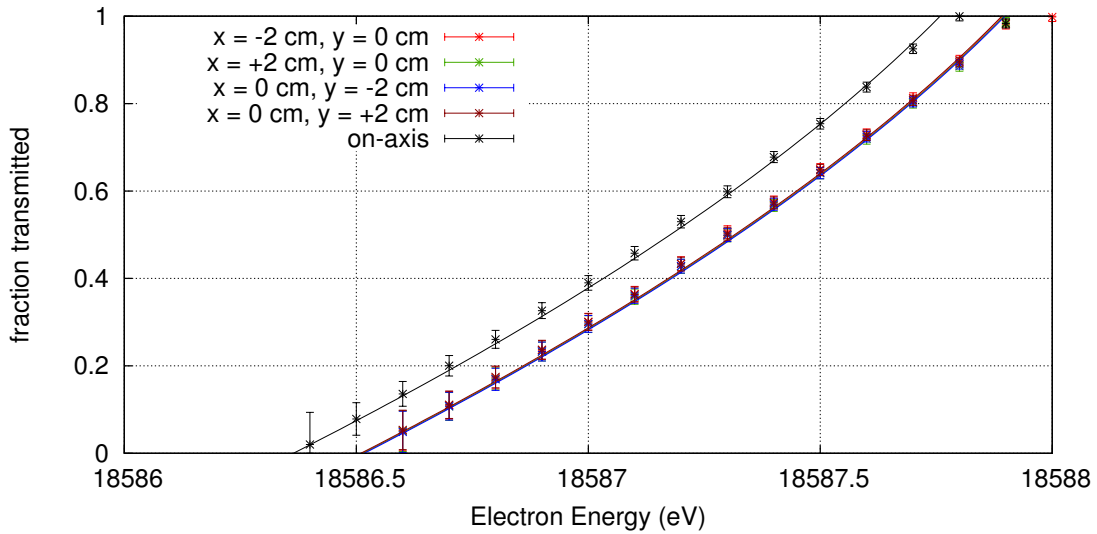


Figure 6.6: Transmission simulations with the magnetic materials setup: The transmission properties on-axis are clearly different from those off-axis, as the analyzing magnetic field is different. But also the different off-axis positions show varying transmission rates.

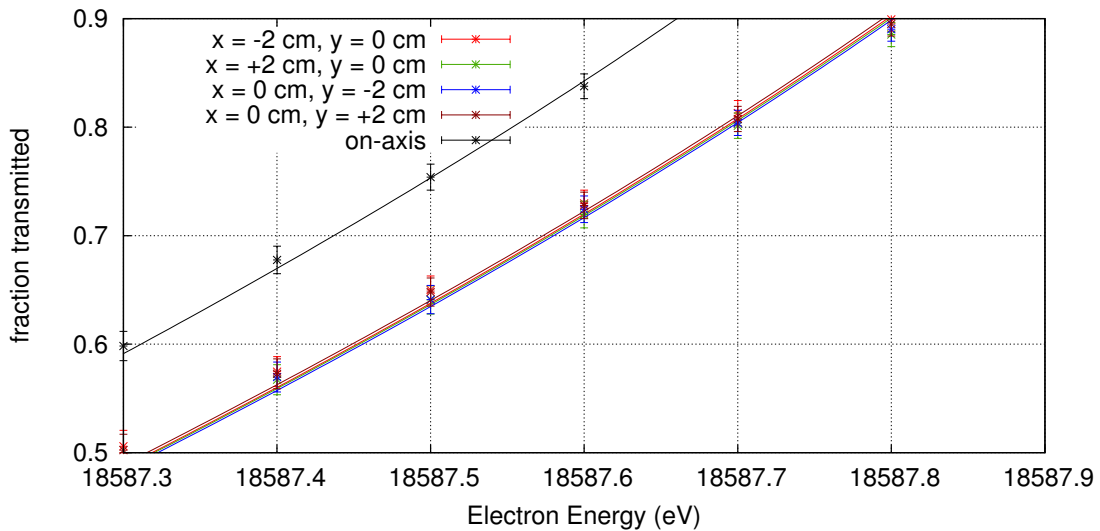


Figure 6.7: Zoom in on the transmission simulations data of the magnetic materials setup: The differences in transmission rate of the off-axis starting points are small but clearly discernible. The corresponding transmission functions also vary visibly.

to distinguish it from E , the energy of the electron given in eV. The first term is the $\vec{\mathcal{E}} \times \vec{B}$ drift:

$$\vec{v}_{\vec{\mathcal{E}} \times \vec{B}} = \frac{\vec{\mathcal{E}} \times \vec{B}}{|\vec{B}|^2} \quad (6.2)$$

This term leads to an electron drift, if the electric and magnetic fields are not parallel. The second term, the gradient- B drift, depends on the magnetic field and its gradient:

$$\vec{v}_{\nabla B} = \frac{E_{\perp} + 2E_{\parallel}}{|\vec{B}|^3} (\nabla B \times \vec{B}) \quad (6.3)$$

These drifts do not influence the signal electrons significantly, as those travel through the spectrometer too fast. But they can cause an electron to penetrate into the flux tube. On the up side, the same forces may be used to remove stored electrons by applying specific electromagnetic conditions for a short time. These active removal methods include an electric dipole, a magnetic pulse and stochastic heating by a high frequency voltage on the electrodes [63].

An important fact to note is that the gradient- B drift depends on the electron energy, unlike the $\vec{\mathcal{E}} \times \vec{B}$ drift. Since the gradient of the magnetic field does not necessarily have the same direction as the radial electric field component, these drifts can have different signs and cancel each other out. These cancellations are dependent on the electron energy, the magnetic field configuration and the position. For an extended discussion of the background theory, see [92].

Figure 6.8 sketches how (6.2) and (6.3) can cause electrons to enter the flux tube. An azimuthal magnetic field component causes a radial $\vec{\mathcal{E}} \times \vec{B}$ drift, and a gradient in the magnetic field in azimuthal direction results in a radial gradient- B drift.

6.2.2 Extent of Electron Drifts in the Simulated Setup

In the ideal setup, there are no azimuthal magnetic field components or gradients, so it will be omitted in this section. For this calculation, the same magnetic field setup has been used as for the transmission simulations, which is a two-minimum optimized field setup [75]. For a one-minimum setup the situation might be different. The comparison between the azimuthal magnetic field changes induced by the realistically modeled air coil systems and the field of the magnetic materials at $z = 0$ is shown in figure 6.9. The azimuthal field component is shown in the analyzing plane at $z = 0$. At large radii, individual wires of the earth's magnetic field compensation system introduce azimuthal field components. Otherwise there is only a dent in the LFCS in the upper left region disturbing the magnetic field. The magnetic materials on the other hand are highly inhomogeneous and introduce comparatively large azimuthal magnetic field components throughout the spectrometer volume. The azimuthal gradients shown in figure 6.10 are surprisingly similar for both additional fields in localization and strength.

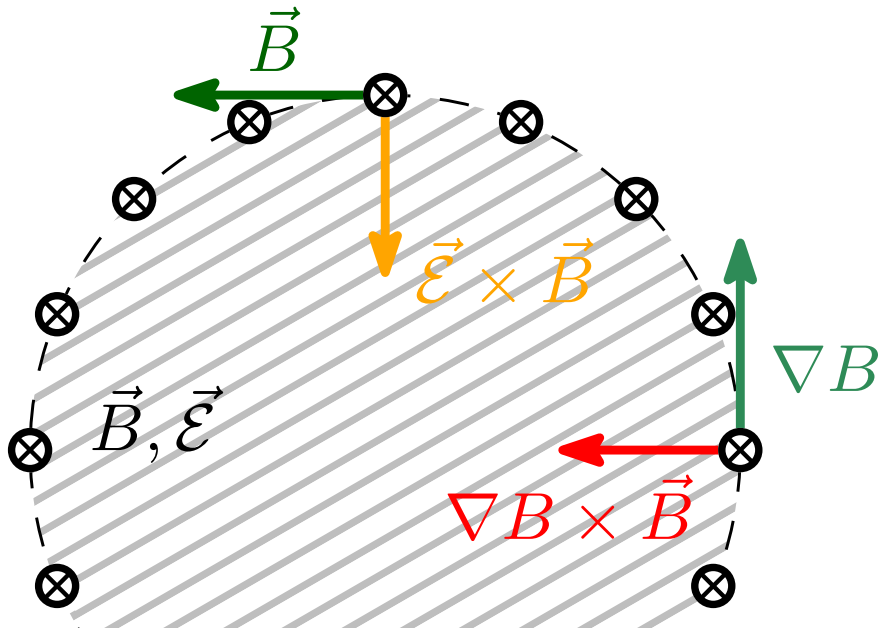


Figure 6.8: Radial drift velocities. The magnetic and electric field \vec{B} and \vec{E} of the MAC-E filter point into the drawing plane. Additional azimuthal magnetic fields cause a radial drift as well as azimuthal gradients in the magnetic field. (Figure from [85])

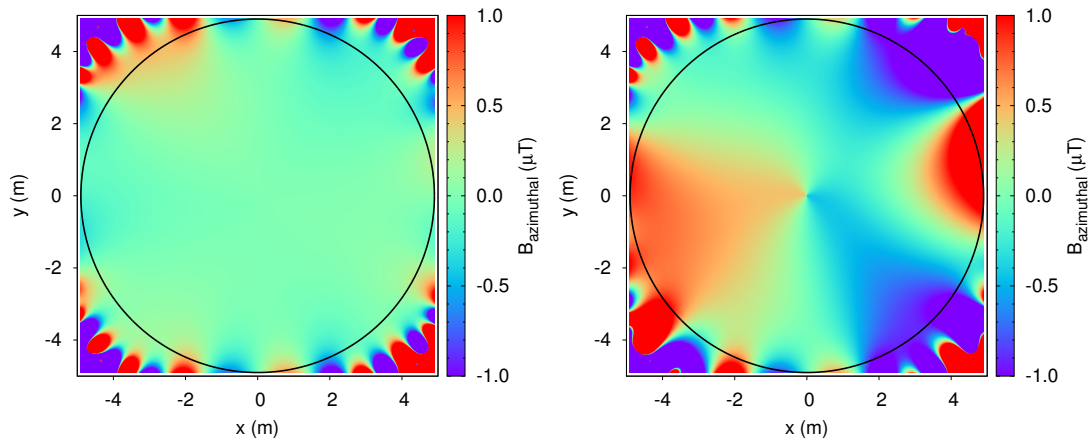


Figure 6.9: Azimuthal magnetic field components in the analyzing plane: The fields are shown at $z = 0$, in the analyzing plane. **Left:** The realistic air coil systems introduces azimuthal components to the magnetic field only in the outer radii, mostly due to the discreteness of the EMCS. Drift forces would not carry electrons far into the spectrometer. **Right:** The magnetic materials introduce azimuthal magnetic field throughout the analyzing plane. The black circle is the position of the spectrometer vessel.

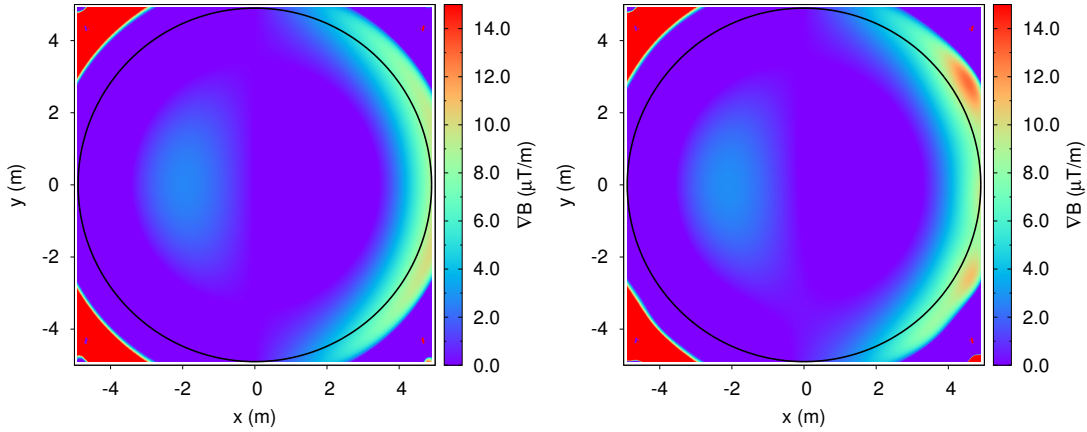


Figure 6.10: Azimuthal magnetic field gradients in the analyzing plane. Left: Air coil system. **Right:** Magnetic materials. Incidentally, both field disturbances produce similar azimuthal magnetic field gradients, although they are stronger in the case of the magnetic materials.

The drift velocities these magnetic fields produce are shown in figure 6.11. The radial drift velocities for the air coil system are largest at large radii, as expected from the azimuthal field. But there, the azimuthal drift velocities are also largest. For the air coil systems, the radial drift velocities are generally larger and also appear in larger regions of the analyzing plane as far inwards as the center, the azimuthal drift velocity distribution is similar.

To determine, whether an electron enters the flux tube, not only the radial drift velocity is of importance. Other field characteristics produce drift velocities in azimuthal direction. These cause charged particles to make a turn around the main spectrometer circumference. Along this way, they cannot penetrate deeper towards the spectrometer center before reaching regions where they drift outwards again. So for small radial drift velocities, the particles cannot enter the flux tube, although azimuthal magnetic fields and gradients are present. Only if the radial drift velocity is in the same order of magnitude as the azimuthal drift velocity there is a danger of increasing background. This is most probable to happen in the area of low azimuthal drift velocities, where the $\text{gradient}B$ and $\vec{\mathcal{E}} \times \vec{B}$ components cancel out.

The determining factor is the ratio between radial and azimuthal drift velocity shown in figure 6.12. For the considered setups, only small dangerous regions are present, and they are not near the vessel surface at $z = 0$. So an electron emitted from there could not drift far enough inwards to reach them. Even the magnetic materials do not increase the danger of guiding electrons into the spectrometer at the analyzing plane, although the regions of high $\frac{v_{\text{rad}}}{v_{\text{azi}}}$ are more pronounced in the case of the considered setup.

Further from the analyzing plane, e.g. at $z = 4$ m the situation is different, the fields have changed and the resulting drift velocities are shown in figure 6.13. The air coil system introduces no significant radial drift and the azimuthal drift is dominated by the

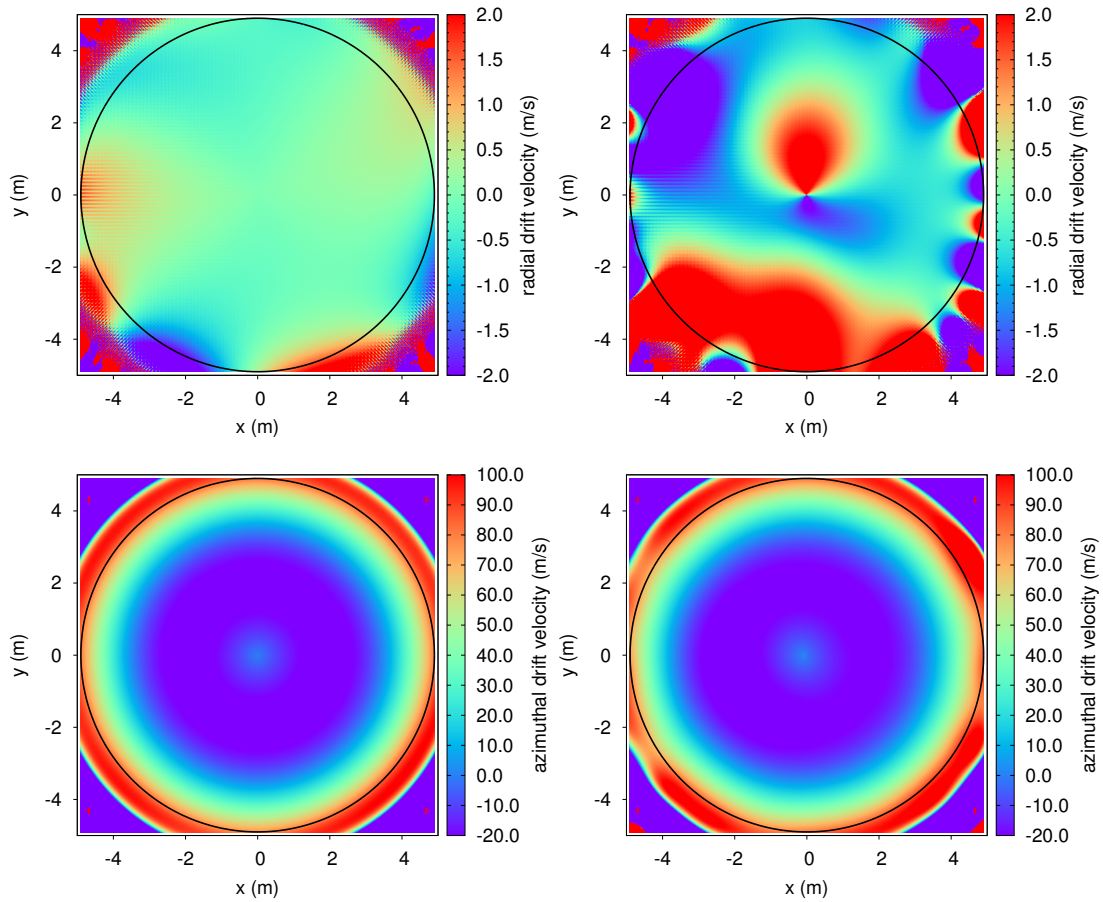


Figure 6.11: Radial and azimuthal drift velocities for 1 eV electrons in the analyzing plane at $z = 0$. **Top left:** Radial drift velocity for the air coil system. **Top right:** Radial drift velocity for the magnetic materials. **Bottom left:** Azimuthal drift velocity for the air coil system. **Bottom right:** Azimuthal drift velocity for the magnetic materials. Note the different velocity scales for radial and azimuthal drift.

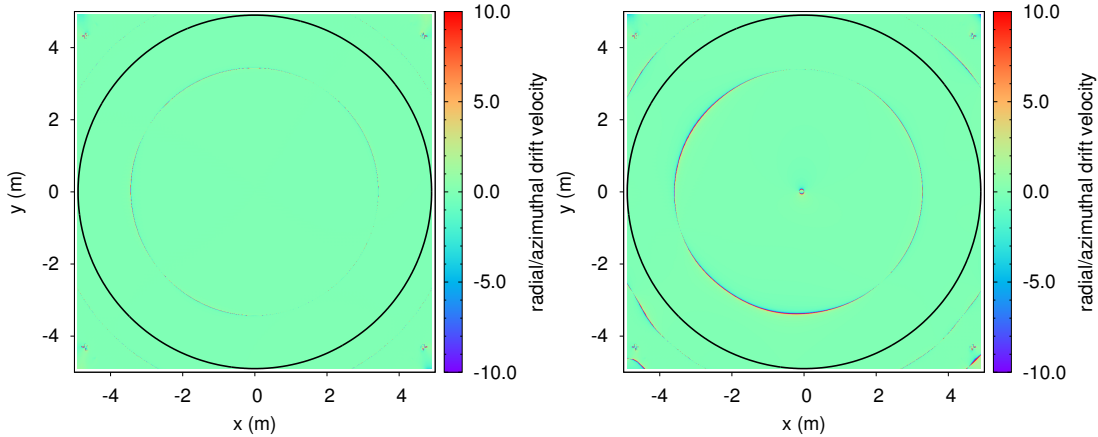


Figure 6.12: Ratio of radial to azimuthal drift velocity for 1 eV electrons in the analyzing plane. Left: Air coil system. Right: Magnetic materials. Both show dangerous regions in a ring at $r \approx 3$ m, but stronger in the case of the magnetic materials field.

axial magnetic field. The magnetic materials on the other hand produce large radial drifts and even have a noticeable influence on the azimuthal drift velocity.

As for the ratio of radial to azimuthal drift velocity, figure 6.14 compares the ratios for the air coil and for the magnetic materials setup. With the magnetic materials situation, there is a region of large radial drifts, which is almost nonexistent in the air coil case, dangerously close to the spectrometer wall. Here background electrons might very well penetrate into the flux tube. But since the large $\frac{v_{\text{rad}}}{v_{\text{azi}}}$ ratios are only at large radii, here electrons penetrate not far into the flux tube.

Since electrons also travel along the axial direction of the spectrometer between their reflection points, an unfortunate distribution of drift velocity regions could lead to a significant increase in background. Consider a setup, where electrons are guided into the edges of the flux tube at large z positions and drifted further in closer to the analyzing plane. Such a situation would be very disadvantageous.

6.3 Summary

The influences of the realistic air coil system and the magnetic materials disturb the magnetic field in the main spectrometer. With the methods detailed in previous chapters, these influences can be accurately quantified and reproduced in magnetic field simulations. Using these updated simulations, detailed particle tracking simulations have been performed to examine the influence of these field disturbances on the transmission properties of the main spectrometer. These simulations show that on-axis there is no discernible difference between the setups, but that the transmission rates differ with starting positions off-axis. A direct comparison between the simulations with the magnetic materials setup shows that this difference at a radius of $r = 2$ cm in the pre spectrometer magnet is at the 1 % level. The magnetic field data shown in figure 6.3 indicates that this difference grows stronger at larger radii. So neglecting the influences of the air coil system and the magnetic materials on the magnetic field in the

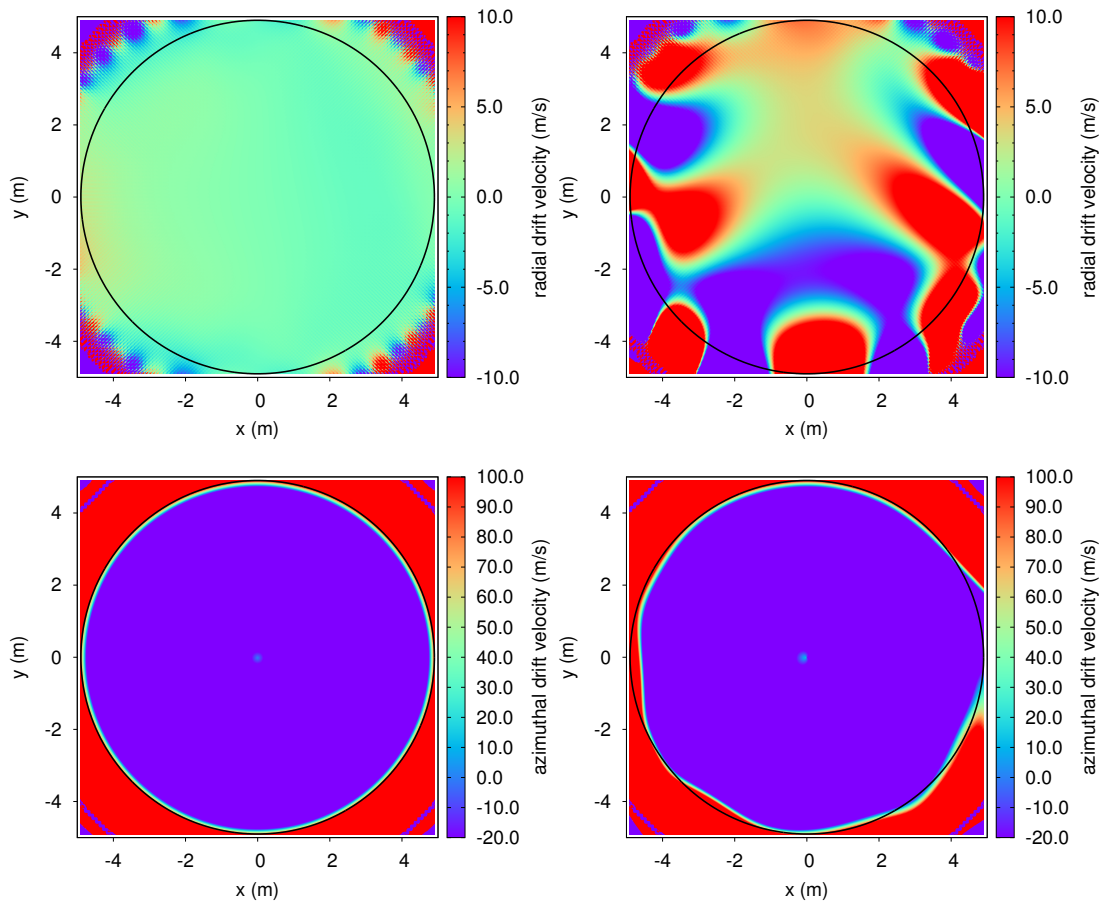


Figure 6.13: Radial and azimuthal drift velocities for 1 eV electrons at $z = 4$ m. Top left: Radial drift velocity for the air coil system. Top right: Radial drift velocity for the magnetic materials. Bottom left: Azimuthal drift velocity for the air coil system. Bottom right: Azimuthal drift velocity for the magnetic materials.

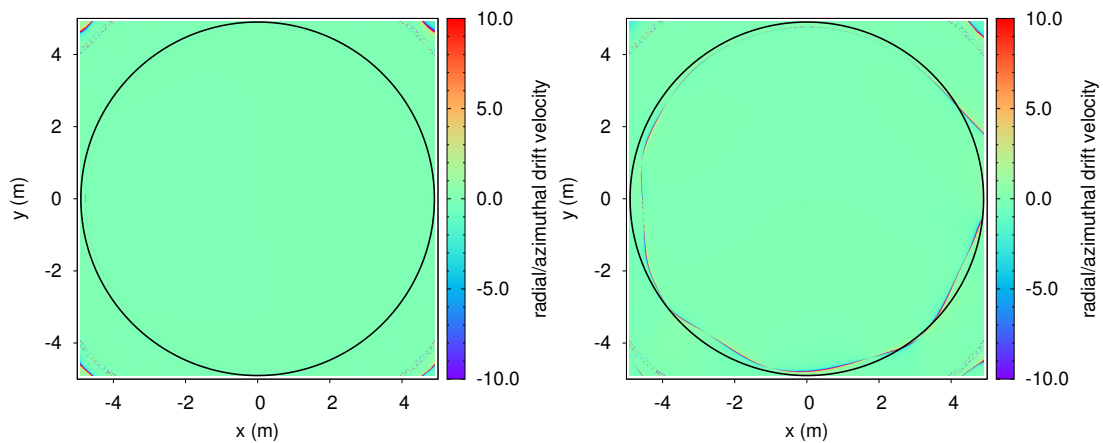


Figure 6.14: Ratio of radial to azimuthal drift velocity for 1 eV electrons at $z = 4$ m. Left: Air coil system. Right: Magnetic materials.

main spectrometer would lead to an error in the transmission function at the % level. Since updated and accurate field information is available, it is possible to accurately describe their influence on the transmission properties of the KATRIN main spectrometer. The only unknown quantities are the induced magnetizations of the magnetic material during run-time of the superconducting magnets. This can only be determined by measurements, for example with the monitoring system described in chapter 7.

In addition to the effect on the electron transmission in the main spectrometer, the magnetic field disturbances, especially azimuthal field components and gradients, alter the background reduction abilities of the setup. With the accurate field simulations, drift velocities can be calculated anywhere in the main spectrometer. The magnetic materials introduce significant changes in the axial symmetry of the magnetic field. In the analyzing plane, the azimuthal drift velocities near the spectrometer wall are much larger than the induced radial drift velocities, electrons are drifted around the spectrometer circumference and radial drifts cancel each other out. But regions of large radial drifts exist in the central region, and electrons guided into the flux tube at larger z positions might drift further inwards and significantly increase background. This is a subject which has to be considered very thoroughly when planning magnetic setups for the main spectrometer.

7. Precision Magnetic Monitoring System

The magnetic field in the main spectrometer is of great importance to the analysis of the MAC-E filter data. Knowledge of that field is essential to the KATRIN efforts. The simulations detailed in chapter 4 and 5 describe a given magnetic setup very accurately. But it has also been observed that the magnetic conditions in the main spectrometer are not constant. So a permanent monitoring of the magnetic field is necessary.

Since direct field measurements in the vacuum vessel are impossible, this monitoring system has to rely on simulations based on measurements outside the main spectrometer tank. There are two complementary approaches pursued at the KATRIN main spectrometer which will be discussed in the following sections.

7.1 Principles of Magnetic Monitoring at the KATRIN Main Spectrometer

The two monitoring approaches are based on different principles. Our collaborators at the University of Applied Sciences in Fulda are developing a **Mobile Sensor** system which will be able to determine the field in the spectrometer volume from measurements around the surface [93], [94].

At KIT, continuous measurements at specific points in space will be compared to field simulations including all magnetic field sources. This system has been developed in this work and in [77]. Technical realisation and commissioning of the system is ongoing in [95]. Both [77] and [95] are diploma theses supervised in the scope of this work.

7.1.1 MobS System

The MobS System is not part of this work and will only be briefly introduced here as it complements the continuous monitoring system.

In a current-free volume with static electric potential, like the KATRIN main spectrometer, the magnetic field is rotation-free.

$$\vec{\nabla} \times \vec{B} = 0 \tag{7.1}$$

For this field there exists a scalar function $V(\vec{x})$ with $\vec{\nabla} \times \vec{\nabla} \cdot V(\vec{x})$ so that

$$\vec{B} = \vec{\nabla} \cdot V(\vec{x}) \tag{7.2}$$

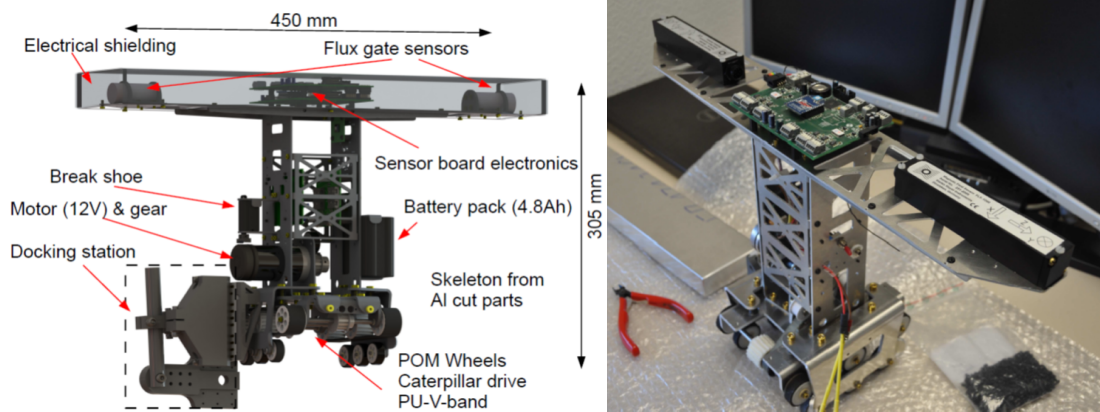


Figure 7.1: Mobile sensor unit. **left:** Technical drawing of the MobS unit with components. **right:** Photograph of a MobS Prototype. The magnetic field sensors and the electronics board are clearly visible on the top. They will be covered with the shell lying besides the unit for high voltage safety.

Since $\vec{\nabla} \cdot \vec{B} = 0$, $V(\vec{x})$ fulfills the Laplace equation

$$\vec{\nabla}^2 \cdot V(x, y, z) = 0 \quad (7.3)$$

Utilizing the finite difference method, the field inside a volume can be calculated, using the derivatives of $V(\vec{x})$ on the surface of the volume (von-Neumann boundary conditions). The derivatives of $V(\vec{x})$ are the field components B_x , B_y and B_z . The method has been shown to reproduce a simulated field with $< 2\%$ accuracy in all components [93].

The magnetic fields for the von-Neumann boundary conditions for the actual spectrometer field calculations will be measured by a set of mobile magnetic field sensor stations shown in figure 7.1. These stations will run on the inside of the LFCS holding structure. Each is equipped with two 3-axis fluxgate magnetometers half a meter apart and can measure the magnetic field on any position on the LFCS ring. A technical design summary is given in [94].

Besides the finite boundary calculations, the system offers a large number of precise magnetic field measurements around the volume of interest. These magnetic field measurements are ideally suited for the calculation of magnetic material models described in section 5.2.

The MobS system offers a model-independent magnetic field calculation inside the main spectrometer volume. Unfortunately it is not instantaneous with a measurement taking ~ 10 minutes or longer depending on the number of measurement points. So it can only be used in measurement pauses. It also records only a snapshot of the field at the time of magnetic field measurements. This is sufficient for analysis if the field does not change, but the MobS system cannot monitor the field at all times.

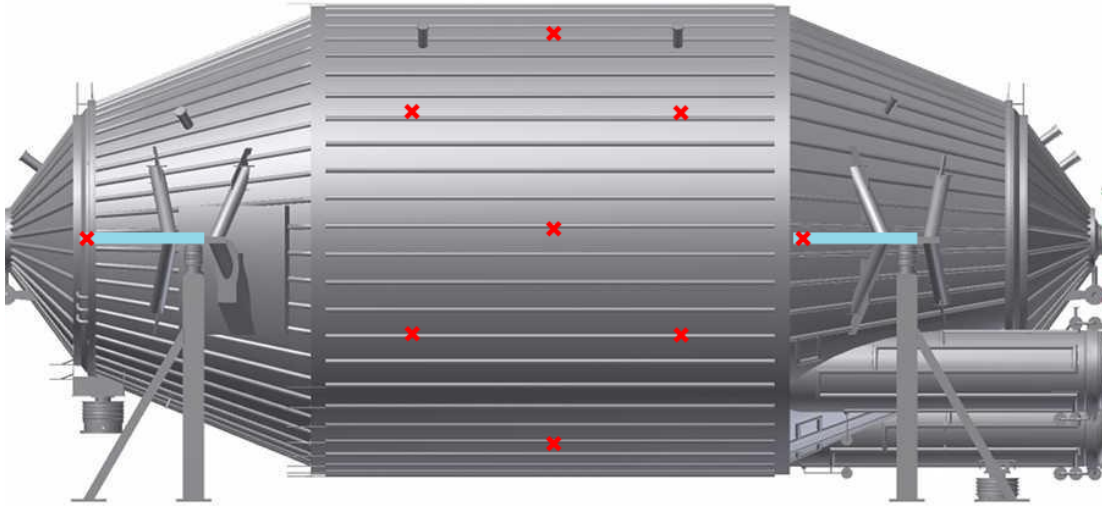


Figure 7.2: Positions of magnetic monitoring stations around the main spectrometer. The magnetometers are arranged in three rings, 6 sensor stations at the analysing plane, 4 each at $z = 2$ m. In addition there will be another 4 magnetometers around the main spectrometer fixed to the support structure.

7.1.2 Continuous Monitoring System

The magnetic field determination approach taken at KIT is based on carefully mapping all magnetic field sources and simulating their fields. This is no trivial task, but the magnetic fields of superconducting solenoids, air coil system and magnetic materials are well described and the resulting field can be calculated to ≤ 1 % accuracy with respect to actual measurements.

This allows for accurate field calculations anywhere in the main spectrometer region. But as the validity of the field is not guaranteed, it has to be cross checked by measurements. For this purpose, a system of 18 precise magnetometer stations covering the area of interest will be installed around the main spectrometer. They will constantly monitor the magnetic field and the simulations will be compared against these measurements. This way, it is assured, that the magnetic field sources are correctly represented in the field simulation. The uncontrollable time dependent contributions to the overall field are the earth's magnetic field and the magnetic materials. So if all sensor around the spectrometer show an equal offset from the simulations, the EMCS can be adjusted accordingly to compensate the altered field configuration. If on the other hand different magnetometer stations show different changes, a new magnetic materials model will have to be updated. Figure 7.2 shows, where the sensors will be placed. There will be one ring equipped with 6 sensor stations in the analysing plane and two rings with 4 sensor stations each 2m north and south of the analysing plane. In addition there will be one magnetometer on each of the pillars on which the main spectrometer rests. The holding structures have a small magnetic field. At more than 1 m distance, this field contributes less than 1 permille to the total field, therefore these sensors will be mounted 1.3 m away on beams.

With this setup, it is possible to provide users with accurate magnetic field simulations, for a specified time and setup, to use in analyses. This field information will be stored either as a field map or as a source file in the KATRIN database so that analysts consistently use the correct field.

The software components for this monitoring systems have been described earlier in this work: The field calculation methods, as well as the models for the air coil system and the magnetic materials. The hardware part of the monitoring system will be detailed in the next section.

7.2 Technical Design of the Continuous Monitoring Stations

The purpose of the sensor stations is to provide accurate vectorial magnetic field data with precise positioning and orientation information. The sensor stations have been carefully designed for a spatial positioning of 1 cm and an angular orientation of better than 0.1° . The magnetometers on the main spectrometer will be mounted on top of the thin aluminum shell covering the thermal insulation. This is a flexible surface which will change during bakeouts of the spectrometer and might not return to its original position. This would change the position and orientation of the magnetometers. To account for this, sensor stations have been designed which house equipment for determining position and orientation of the magnetometers. The station components will be detailed in section 7.2.1, the calibration procedure needed to achieve the angular resolution will be discussed in section 7.2.3.

7.2.1 Sensor Station Design

The magnetic field is measured by a 3-axis fluxgate magnetometer by Bartington Instruments with an accuracy of 10 – 20 nT for each component. The magnetometer also has a very stable offset and excellent linearity [96]. To get the magnetic field vector in the KATRIN reference frame, the position and orientation has to be measured as well.

To this end, the magnetometer is integrated into a sensor station which allows to determine these parameters. The position can easily be measured directly with survey equipment. For the orientation, a 2-axis inclinometer is installed as well as a laser setup. The inclinometer directly gives the tilt of the sensor station but cannot measure a rotation around the gravitational axis. To address this, a module of three lasers is also attached. With a known laser and magnetometer geometry this allows a redundant measurement of position and provides three-dimensional information about the orientation of the magnetometer.

The prototype station is shown in figure 7.3.

7.2.2 Inclinometer Test

The inclinometers in combination with the fluxgate magnetometers have been tested in [77]. Figure 7.4 shows the test setup with a Helmholtz-coil. In this measurement, the Helmholtz coil was adjusted to produce a magnetic field in vertical direction. The combined magnetometer and inclinometer setup was placed such that the sensor elements

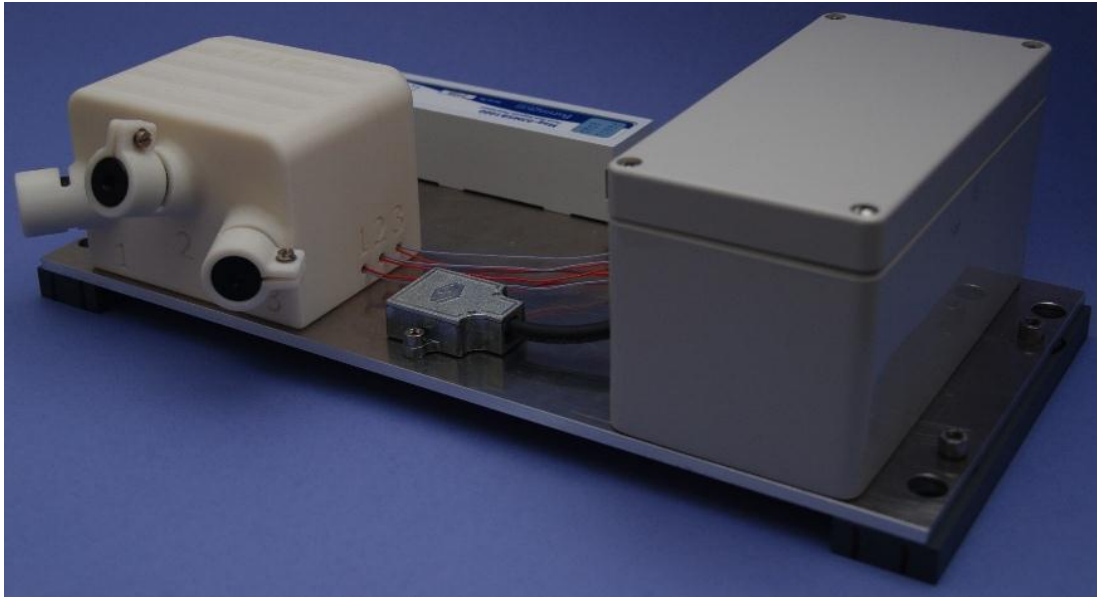


Figure 7.3: Prototype of the continuous magnetic field monitoring stations. The magnetometer in the back is supported by the laser box for position and orientation measurements (white) and the inclinometer for precise orientation (metallic). The grey box houses cable distributions and voltage distribution.

of the magnetometer were in the center of the Helmholtz-coils. Then the plate on which the sensors were mounted was tilted and the tilt was recorded with the inclinometer. Then the measured magnetic field vector was corrected by the measured tilt. With this procedure, all processed measured magnetic fields should be the same. Figure 7.5 shows the results: The absolute field strength varies in the sub-permille level and the angular deviations of the field are one order of magnitude smaller than the internal orthogonality of the magnetometer sensor elements.

The results from this test are very promising, the angular deviations are well below the orthogonality tolerance of the magnetometer. This kind of inclinometer provides orientation information about the sensor station which is only limited by the internal magnetometer construction.

7.2.3 Orientation and Positioning with a Laser System

The inclinometer setup offers very precise information about the tilt of the sensor station, but cannot determine the fully three-dimensional orientation of the magnetometer. To address this shortage, a module with three lasers is installed on each sensor station. Implementing and calibrating these laser modules is part of [95].

The lasers mark three non-orthogonal vectors \vec{l}_i which intersect the spectrometer hall walls in a few meters. The longer the distance between laser and wall the smaller the relative error from inaccuracies in the setup becomes. The module is constructed so that the \vec{l}_i intersect at the position \vec{L} which marks the position of the laser system.

Figure 7.4:
Setup of inclinometer test measurements.
 The test apparatus consists of a Helmholtz-coil pair, the combined magnetometer/inclinometer setup and wooden spacers. The angle was varied by placing spacers between the base aluminum plate and the plate holding the sensors.

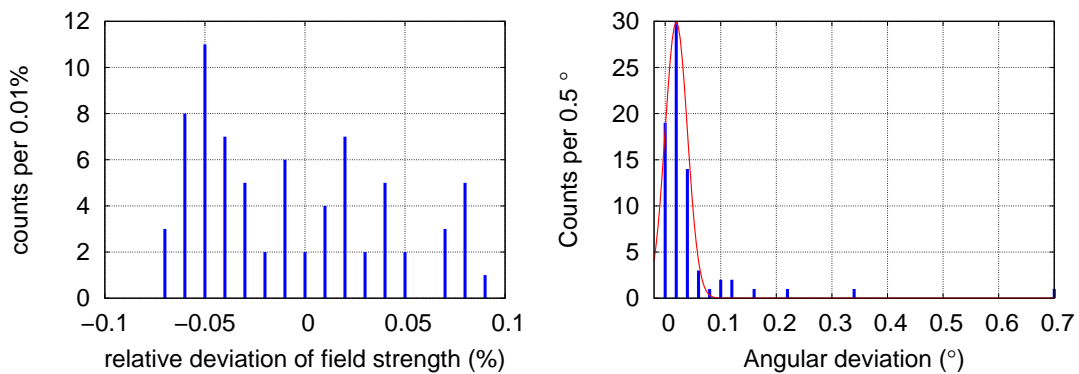
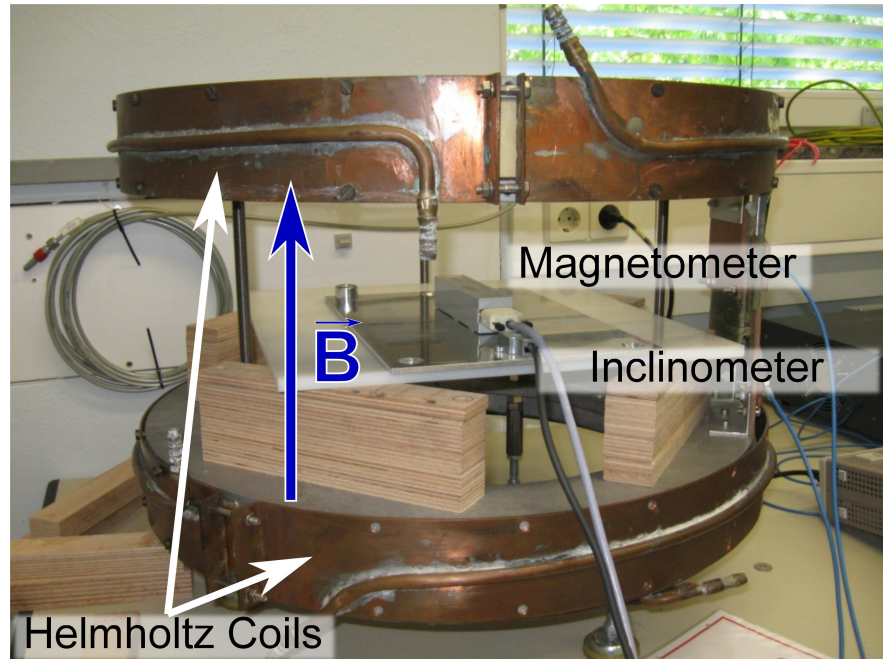


Figure 7.5: Data of inclinometer test. Shown here is a comparison between individual measurements of \vec{B}_n with the average field B_{average} . **left:** Absolute field strength variations. **right:** Angular deviations. The red gaussian has a mean of $\mu = 0.02^\circ$ and a width of $\sigma = 0.02^\circ$.

The i -th laser marks the point \vec{P}_i . With ϕ_{ij} the angle between two laser beams, \vec{L} must fulfill the equation system

$$\begin{aligned}\cos(\phi_{12}) &= \frac{(\vec{P}_1 - \vec{L}) \cdot (\vec{P}_2 - \vec{L})}{|\vec{P}_1 - \vec{L}| \cdot |\vec{P}_2 - \vec{L}|} \\ \cos(\phi_{13}) &= \frac{(\vec{P}_1 - \vec{L}) \cdot (\vec{P}_3 - \vec{L})}{|\vec{P}_1 - \vec{L}| \cdot |\vec{P}_3 - \vec{L}|} \\ \cos(\phi_{23}) &= \frac{(\vec{P}_2 - \vec{L}) \cdot (\vec{P}_3 - \vec{L})}{|\vec{P}_2 - \vec{L}| \cdot |\vec{P}_3 - \vec{L}|}\end{aligned}\quad (7.4)$$

The angles ϕ_{ij} have to be measured carefully for each laser module. With this calibration, \vec{L} can be found by minimizing

$$U(\vec{L}) = \sum_{i,j \in \{1,2,3\}, j>i} \left(\frac{(\vec{P}_i - \vec{L}) \cdot (\vec{P}_j - \vec{L})}{|\vec{P}_i - \vec{L}| \cdot |\vec{P}_j - \vec{L}|} - \cos(\phi_{ij}) \right)^2 \quad (7.5)$$

The minimization is done with a gradient descent algorithm. The numerical uncertainty in the result is much smaller than the estimated error in determining \vec{P}_i . Once the position of the magnetometer $\vec{M} = \sum_{i=1}^3 m_i \hat{l}_i$ in the laser coordinate system is calibrated, the position of the magnetometer in the KATRIN coordinate system is given by

$$\vec{M} = \vec{M}_l + \vec{L} \quad (7.6)$$

To determine the magnetometer axes relative to the KATRIN system, the magnetometer axes in the laser coordinate systems have to be calibrated:

$$\hat{m}_i = \sum_{j=1}^3 m_{ij} \hat{l}_j \quad (7.7)$$

The laser vectors in the KATRIN system are determined by:

$$\hat{l}_j = \frac{(\vec{P}_j - \vec{L})}{|\vec{P}_j - \vec{L}|} = \sum_{k \in \{x,y,z\}} l_{jk} \hat{k} \quad (7.8)$$

Combining (7.7) and (7.8) gives the magnetometer axes in the global KATRIN coordinate system as:

$$\hat{m}_i = \sum_{j=1}^3 \sum_{k \in \{x,y,z\}} m_{ij} l_{jk} \hat{k} \quad (7.9)$$

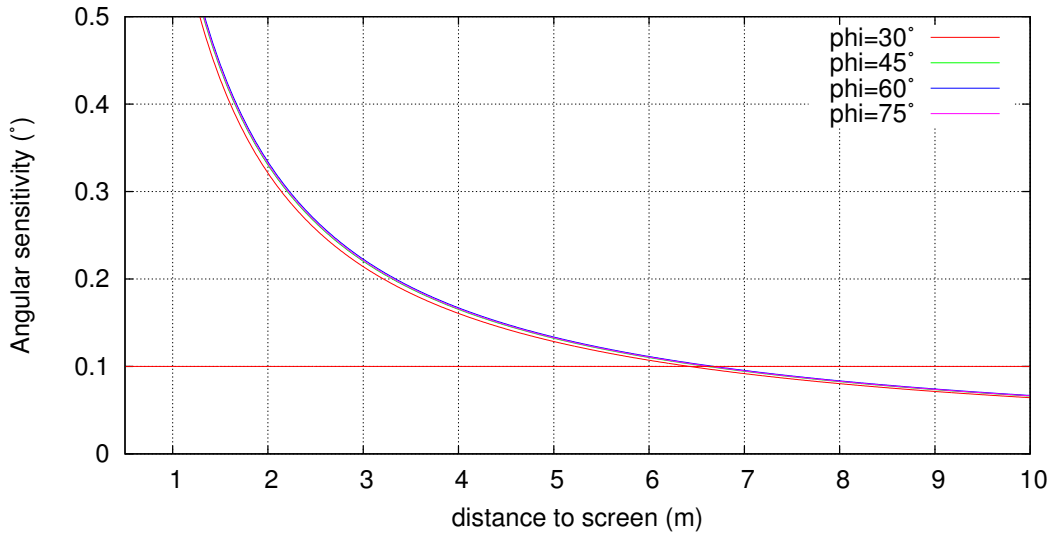


Figure 7.6: Angular sensitivity of the laser calibration setup: The plot shows the calculated angular resolution of the test setup depending on the distance d between laser module and screen. The different curves are for different angles between lasers. An acceptable resolution is reached at distances larger than 6.5 m

With this equation, the measured magnetic field vectors can be transformed into the KATRIN coordinate system.

For this process, it is very important that the angles ϕ_{ij} are well known. A calibration procedure is being developed to determine these angles. If the coordinate transformation is to work reliably, the angular resolution has to be significantly lower than the intrinsic magnetometer uncertainty. The calibration will be done by placing the laser module on a precise angle meter. In a distance d a screen will be placed. The whole setup will be leveled until the two laser points are projected on the same spot, and the angle is recorded. The accuracy of the procedure depends strongly on size of the apparatus. Figure 7.6 shows the reached sensitivity depending on the distance d .

Combining these devices on a sensor station allows the construction of a very accurate magnetic monitoring system. With this it will be possible to validate the field simulations which are used in the main spectrometer data analysis. The continuous magnetic monitoring system makes a valuable contribution to the overall KATRIN effort to determine the electron anti-neutrino mass. As of this writing, all components are on site and construction of the modules is ongoing.

8. Conclusions

From the postulation in 1930 and first direct observation of neutrinos in 1956, neutrino physics today has entered a new precision era. Three generations of neutrinos, complementing the three charged leptons, were directly observed and in the last decades detailed measurements of their properties were driven forward. From cosmological observations more and more precise mass limits have been derived. The solving of the solar neutrino problem has established neutrino oscillations and with it the proof that neutrinos must have a finite mass. Oscillation experiments with solar, atmospheric, reactor and collider neutrinos have determined the mixing angles between the neutrino flavours. Neutrinoless double- β -decay experiments are racing to determine whether the neutrino is a Majorana particle and differs from its antiparticle only by helicity. Direct measurements of the kinematics of β -decay have set more and more precise upper limits on the absolute neutrino mass, culminating in the efforts of the Mainz and Troitsk experiments.

The **K**arlsruhe **T**ritium **N**eutrino experiment KATRIN is a next generation neutrino mass experiment and will discover an electron anti-neutrino mass of down to 0.35 eV with 5σ significance or push down the upper mass limit to 0.2 eV at 90 % C.L. It uses the MAC-E Filter principle to analyze the energy spectrum of electrons from tritium decay. The MAC-E filter depends on the precise combination of electric and magnetic fields to guide and analyze the electrons. The KATRIN experiment is currently under construction at the KIT campus north with the main spectrometer commissioning phase beginning.

The commissioning of the LFCS and EMCS air coil systems at the KATRIN main spectrometer was a major success of this work. The accurate measurement of the air coil fields, their deviations from the ideal setup and their subsequent reproduction with the KASSIOPEIA simulation package was an important step in describing the main spectrometer accurately.

The observation of the magnetic materials posed a challenge to the magnetic field simulations. Measurements showed these fields to be highly inhomogeneous and time-dependent. But with measurements done around the main spectrometer and new approaches to the magnetic field simulations, a first realistic description of the magnetic materials field in the main spectrometer was achieved in this work.

To evaluate the impact of this new accuracy in determining magnetic fields at the main spectrometer, Monte-Carlo particle tracking simulations were done in the scope of this work. The simulations were set-up with realistic air coil and magnetic materials field. The data about the air coil systems, determined during their commissioning, was introduced in the first step. They were designed to optimally influence the magnetic

fields. The unforeseen gravitational deformation of the LFCS and the discreteness and changed setup of the EMCS did not effect the transmission properties of the main spectrometer in a detectable fashion. In a second step, the field of the magnetic materials was implemented. The changes in the transmission properties of the main spectrometer are minimal and statistically not significant in the majority of the inner spectrometer volume. But at large radii, there is a detectable discrepancy and slight adjustments to the transmission function are needed to describe the data accurately. These changes can be accounted for by the segmentation of the KATRIN focal plane detector, but only if the magnetic fields are accurately known. The description of this effect is a major contribution of this work to the KATRIN neutrino mass efforts.

The changed magnetic fields not only influence the transmission properties of the main spectrometer, but also the magnetic shielding effectiveness and storage conditions for trapped particles, the two main background sources from this component. The calculation of electron drift velocities in the main spectrometer were done for the first time with realistic magnetic fields in this work. In the analyzing plane, the flux tube is well shielded from electrons from the inner spectrometer surface, but at other positions the situation is different and particles might enter the flux tube and then be drifted further inwards near the analyzing plane. The influence of the magnetic materials might create dangerous conditions in which the background from the inner surface of the spectrometer is significantly increased. This topic has to be considered carefully in planning and analyzing spectrometer measurements.

In order to enable the KATRIN experiment to check the validity of the magnetic field simulations, a magnetic monitoring system at the main spectrometer has been designed in the scope of this work. Tests of individual hardware components were promising and construction of the sensor stations is ongoing. When finished, this system will allow precise, continuous monitoring of the magnetic field in the main spectrometer region. With this, the correct corresponding magnetic field simulation setup can be determined for each given time interval. As shown in the Monte-Carlo transmission simulations, this knowledge is important to any analysis of main spectrometer data during commissioning and later the measurement of neutrino mass data.

In conclusion, the efforts in this work have culminated in a successful comprehensive and detailed description of the magnetic fields in the KATRIN main spectrometer. This includes not only the superconducting solenoids and the air coil systems as the main field sources, but also the gravitational deformation of the LFCS, the adapted EMCS and the highly inhomogeneous field of the magnetic materials at the sub-percent level of the KATRIN analyzing field. It has also been shown that these detailed informations about the magnetic field serve to improve the understanding of the main spectrometer transmission properties to a very detailed level. This allows for a new level of detail in the energy analysis of electrons passing through the main spectrometer. Thus the information derived in this work is an important contribution to the effort of pushing the KATRIN sensitivity on the electron antineutrino mass to the utmost limit of MAC-E filter spectroscopy.

A. Components of the Continuous Magnetic Monitoring System

A.1 Magnetometer

The magnetic field sensors used in the monitoring stations are MAG-033MSB1000 three axis fluxgate magnetometers from Bartington Instruments. The fluxgate magnetometer uses two ferromagnetic cores which are magnetized into saturation by a coil driven with an alternating current. The winding is so that the cores are magnetized in opposite directions. A secondary pick-up coil measures an induced voltage, see figure A.1. In a field-free environment, the magnetization of both cores is symmetric, and there is no resulting current induced in the secondary coil. If however there is a magnetic field present, one of the cores is saturated earlier and the situation is no longer symmetric. The secondary coil then picks up a signal from the alternating fields of the ferromagnetic cores.

To achieve a high linearity in the sensor, a tertiary coil is installed around the whole setup which is driven by a direct current. This current is adjusted until the secondary coil no longer measures any signal, at this point the field produced by the tertiary coil is exactly opposite to the outer field which is to be measured. The current in the tertiary coil has a strictly linear relation to the field the coil produces. So this current can then be taken as a measure of the outer magnetic field. A setup of three perpendicular sensor elements can then measure the vectorial magnetic field.

Figure A.2 shows a technical drawing of the sensors used in the magnetic field monitoring system.

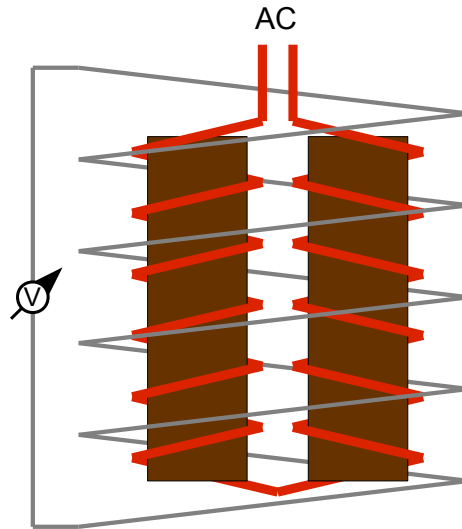


Figure A.1: Sketch of a fluxgate magnetometer: The ferromagnetic cores are drawn in brown, the magnetizing coils which are driven with an alternating current in red. The secondary coil which picks up the magnetic field signal is shown in grey.

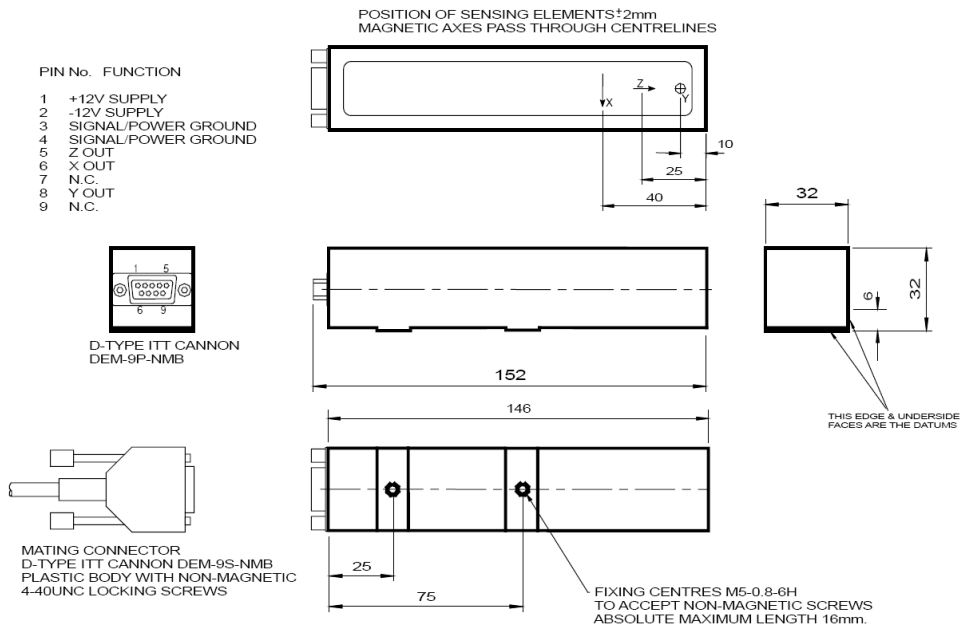


Figure A.2: Technical drawing of the Bartington Mas-03MS sensor. Picture taken from the technical sensor manual [96].

Table A.1: Mechanical, electrical and environmental specifications of the Bartington Mag-03MSB [96].

Parameter	Value
Enclosure	reinforced epoxy
Dimensions (mm)	$32 \times 32 \times 152$ length
Mounting	2 x M5 fixing holes
Connector	ITT Cannon DEM-9P-NMB
Mating connector	ITT Cannon DEM-9S-NMB
Operating temperature	$(-40 \dots + 70)^\circ\text{C}$
Weight	160g
Measuring range	$\pm 1000 \mu\text{T}$
Scaling	$10 \frac{\text{mV}}{\mu\text{T}}$
Scaling temperature coefficient	$200 \frac{\text{ppm}}{^\circ\text{C}}$
Offset error	$\pm 50 \text{ nT}$
Offset temperature coefficient	$\pm 0.6 \frac{\text{nT}}{^\circ\text{C}}$
Supply voltage	$\pm 12 \text{ V}$ to $\pm 17 \text{ V}$
Analog output	$\pm 10\text{V}$ swings to within 0.5V of supply voltage
Output impedance	$< 10 \Omega$
Linearity error	$< 0.0015\%$
Bandwidth	$0 \dots 3\text{kHz}$
Orthogonality error	$< 0.1^\circ$

A.2 Inclinometer

For determining the tilt of the sensor station, a SCA121T-D05 two axis inclinometer by VTI Technologies is used. It has two orthogonal measurement axes with a range of $\pm 90^\circ$. The measurement principle is based on the capacity dependence of a plate capacitor. Each sensor element has a fixed plate and a second plate on a flexible beam. The gravitational force pulls on the secondary plate until a force equilibrium between gravitational and elastic force is reached. Depending on the tilt of the sensor, the final distance between the two capacitor plates is different. So the capacity of the sensor depends on the gravitational acceleration of the secondary capacitor plate and the sensor transforms the tilt of the sensor into a measurable voltage. Figure A.3 shows the working principle.

The output voltage is proportional to the sine of the angle, since

$$d = d_0 - \sin(\alpha) \cdot \frac{m \cdot g}{D_{\text{elastic}}} \quad (\text{A.1})$$

and

$$C = \epsilon_0 \cdot \epsilon_r \cdot \frac{A}{d} \quad (\text{A.2})$$

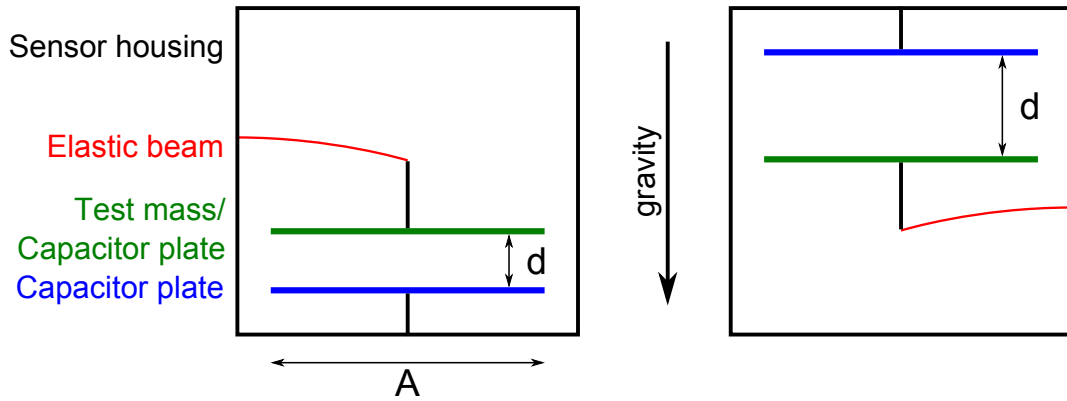


Figure A.3: Working principle of the inclinometers

As the output is ratiometric, the input voltage has also to be measured to get an accurate measurement of the angle.

Table A.2: Performance characteristics of the SCA121T-D05 inclinometer [97]

Parameter	Value
Measuring range	$\pm 90^\circ$
Supply Voltage	$(5 \pm 0.25)\text{V}$
Offset	$V_{dd}/2$
Offset calibration error	max. $\pm 1.5^\circ$
Sensitivity	$2\text{V} / g$ $35\text{mV}/^\circ$ (@Offset Pos.)
Sensitivity calibration error	$\pm 1.5\%$
Sensitivity temperature dependency ($(0 \dots 70)^\circ\text{C}$)	$-0.8 \dots 0.3\%$
Offset temperature dependency ($(0 \dots 70)^\circ\text{C}$)	$\pm 0.5^\circ$
Frequency response (-3dB)	$(8 \dots 28)\text{Hz}$
Cross-axis sensitivity	maximal 4%
Ratiometric error	$\pm 2\%$

Bibliography

- [1] W. Pauli. *Wolfgang Pauli, "Offener Brief an die Gruppe der Radioaktiven bei der Gauvereins-Tagung zu Tübingen"*. published in R.Kronig and V. Weisskopf (Eds.), Wolfgang Pauli, Collected scientific Papers, Vol.2, Interscience, New York (1964), 1930.
- [2] E. Fermi. *Versuch einer Theorie der β -Strahlen*. Z. Phys 88(1934) 161-171.
- [3] J. Chadwick. *Possible Existence of a Neutron*. Nature, Vol. 129, 312, 1932.
- [4] C. L. Cowan, Jr., F. Reines, F. B. Harrison, H. W. Kruse, und A. D. McGuire. *Detection of the Free Neutrino: A Confirmation*. *Science*, 124:103–104, July 1956.
- [5] J.M. Goulios K. Lederman L.M. Mistry N. Schwartz M. Danby, G. Gaillard und J. Steinberger. *Observation of High-Energy Neutrino Reactions and the Existence of Two Kinds of Neutrinos*. Phys. Rev. Lett. 9 (1962) 36.
- [6] B.M. Pontecorvo. ZhETF 37 (1959) 1751(English translation Sov. Phys. JETP 10 (1960) 1236).
- [7] D. Karlen. Particle Data Group, European Physical Journal C 15 (2000) 357.
- [8] K. Kodama et al. (DONUT Collaboration) (2001). *Observation of tau neutrino interactions*. Physics Letters B Vol. 504(3) 218-224 [http://dx.doi.org/10.1016/S0370-2693\(01\)00307-0](http://dx.doi.org/10.1016/S0370-2693(01)00307-0).
- [9] Y. Fukuda et al. *Evidence for oscillation of atmospheric neutrinos*. Phys. Rev. Lett. 81 (1998) 1562.
- [10] Werner Rodejohann James Barry und He Zhang. *Light sterile neutrinos: models and phenomenology*. JHEP07(2011)091.
- [11] Particle Data Group. *Neutrino Properties*. C. Amsler et al. (Particle Data Group), PL B667, 1 (2008) and 2009 partial update for the 2010 edition (url: <http://pdg.lbl.gov>).
- [12] C. Weinheimer et al. *High precision measurement of the tritium β spectrum near its endpoint and upper limit on the neutrino mass*. Phys. Lett. B460 (1999) 219.

- [13] V.M. Lobashev. *The search for the neutrino mass by direct method in the tritium beta-decay and perspectives of study it in the project KATRIN*. Nucl. Phys. A719 (2003) 153c.
- [14] A.I. Berlev E.V. Geraskin A.A. Golubev N.A. Likhovid V.M. Lobashev A.A. Nozik V.S. Pantuev V.I. Parfenov A.K. Skasyrskaya F.V. Tkachov S.V. Zadorozhny V.N. Aseev, A.I. Belev. *An upper limit on electron antineutrino mass from Troitsk experiment*. Phys. Rev. D84 (2011) 112003.
- [15] KATRIN Kollaboration. *KATRIN Design Report 2004*. Wissenschaftliche Berichte FZKA 7090.
- [16] M. Plümacher W. Buchmüller, P. Di Bari. *Leptogenesis for Pedestrians*. Ann. Phys. 315 (2005) 305 [hep-ph/0401240].
- [17] M. Grossi M. Khlopov D. Fargion, R. Konoplich. *Galactic Gamma halo by heavy neutrino annihilations ?* arXiv:astro-ph/9809260v2 19 Oct 1999.
- [18] Ya. B. Gerstein, S.S. Zeldovich. Pis'ma ZhETF, 4 (1966) 174 (English translation: JETP Letters 4 (1966) 120).
- [19] et al. Bennett, C. L. *First Year Wilkinson Microwave Anisotropy Probe (WMAP1) Observations: Preliminary Maps and Basic Results*. The Astrophysical Journal Volume 583, 2003.
- [20] A.D. Dolgov. *Neutrinos in cosmology*. Phys.Rept. 370 (2002) 333-535; arXiv:hep-ph/0202122v2.
- [21] Gary Steigman. *Big Bang Nucleosynthesis: Probing the First 20 Minutes*. arXiv:astro-ph/0307244v1 11 Jul 2003.
- [22] Ya. B. Shandarin, S.F Zeldovich. *The large-scale structure of the universe: Turbulence, intermittency, structures in a self-gravitating medium*. Rev. Mod. Phys. 61 (1989) 46.
- [23] M. Tegmark et al. *The 3D power spectrum of galaxies from the Sloan Digital Sky Survey*. Astrophys. J. 606 (2004) 702.
- [24] W. Hu et al. *Weighing neutrinos with galaxy surveys*. Phys. Rev. Lett. 80 (1998) 5255.
- [25] D.G. York et al. *The Sloan Digital Sky Survey: Technical Summary*. Astronomical J., 120 (2000) 1579.
- [26] M. Colless et al. *The 2dF Galaxy Redshift Survey: spectra and redshifts*. Mon. Not. R. Astron. Soc. 328 (2001) 1039.
- [27] M. Tegmark et al. *Cosmological parameters from SDSS and WMAP*. Phys. Rev. D69 (2004) 103501.
- [28] John Bahcall. *Homepage of John Bahcall*. <http://www.sns.ias.edu/~jnb/>.

- [29] GNO collaboration. *GNO solar neutrino observations: results for GNO*. Phys. Lett. B490 (2000) 16-26.
- [30] *SAGE the Russian-American Gallium solar neutrino Experiment*. <http://ewi.npl.washington.edu/sage>.
- [31] K.S. Hirata et al. *Observation in the Kamiokande-II detector of the neutrino burst from supernova SN1987A*. Phys. Rev. D38 (1988) 448.
- [32] SNO Collaboraction. *Measurement of the rate of $\nu_e + d \rightarrow p + p + e^-$ interactions produced by ^8Be Solar Neutrinos at the Sudbury Neutrino Observatory*. Phys. Rev. Lett. 87 (2001) 071301.
- [33] B. Aharmin et al. *Determination of the ν_e and total B8 solar neutrino fluxes using the Sudbury Neutrino Observatory Phase I data set*. Phys. Rev. C, vol. 75, p.045502, Apr 2007.
- [34] J. Beringer et al. (Particle Data Group). *2012 Review of Particle Physics*. Phys. Rev. D86, 010001 (2012).
- [35] Super-Kamiokande Collaboration. *Measurement of atmospheric neutrino oscillation parameters by Super-Kamiokande I*. Phys. Rev. D71 112005 (2005).
- [36] KASCADE-Grande collaboration. *The KASCADE-Grande Experiment*. Nucl.Instr. and Meth. A620 (2010) 202-215.
- [37] Auger collaboration. *Auger Project Design Report*. http://www.auger.org/technical_info/design_report.html.
- [38] D.G. Michael et al. (2006). *Observation of muon neutrino disappearance with the MINOS detectors in the NuMI neutrino beam*. Physical Review Letters 97 (19): 191801. arXiv:hep-ex/0607088.
- [39] T2K Collaboration (2011). *The T2K Experiment*. arXiv:1106.1238.
- [40] M. Güler et al. *An appearance experiment to search for $\nu_\mu\nu_\tau$ oscillations in the CNGS beam : experimental proposal*. CERN-SPSC-2000-028 ; LNGS-2000-25 ; SPSC-P-318.
- [41] CHOOZ collaboration. *Initial Results from the CHOOZ Long Baseline Reactor Neutrino Oscillation Experiment*. arXiv:hep-ex/9711002v1.
- [42] Y. et al. [Double Chooz Collaboration] Abe. Indication of reactor anti-electron-neutrino disappearance in the double chooz experiment. *Phys. Rev. Lett.*, 108:131801, Mar 2012.
- [43] J. K. et al. [RENO Collaboration] Ahn. Observation of reactor electron antineutrinos disappearance in the reno experiment. *Phys. Rev. Lett.*, 108:191802, May 2012.
- [44] F.P. An et al. [Daya Bay Collaboration]. Observation of electron-antineutrino disappearance at daya bay. *Phys. Rev. Lett.*, 108:171803, Apr 2012.

- [45] P. Machado, H. Minakata, H. Nunokawa, and R. Funchal. Combining accelerator and reactor measurements of θ_{13} : the first result. *Journal of High Energy Physics*, 2012:1–13, 2012. 10.1007/JHEP05(2012)023.
- [46] Boris Kayser & Stephen Parke. *The Neutrinos*. <http://lbne.fnal.gov/pdfs/Neutrino-overview-Kayser-Parke.pdf>.
- [47] A.A. Elliott, S.R. Hahn und M.K. Moe. *Direct evidence for two-neutrino double-beta decay in ^{82}Se* . Phys. Rev. Lett. 59, 2020 - 2023 (1987).
- [48] TU Dortmund Tobias Koettig. *Website of the Cobra experiment*. http://www.cobra-experiment.org/double_beta_decay/.
- [49] J. Sedgbeer R. Beuselinck und Y. Shitov. *The SuperNEMO Experiment*. <http://www.imperial.ac.uk/research/hep/research/supernemo.htm>.
- [50] H. V. Klapdor-Kleingrothaus et al. *Latest results from the HEIDELBERG-MOSCOW double beta decay experiment*. Eur. Phys. J. A 12 (2001) 147 - 154.
- [51] H.V. Klapdor-Kleingrothaus et al. *Search for neutrinoless double beta decay with enriched ^{76}Ge in Gran Sasso 1990-2003*. Phys. Lett. B 586 (2004) 198 - 212.
- [52] S. Schönert et al. *The GERmanium Detector Array (GERDA) for the search of neutrinoless $\beta\beta$ decays of ^{76}Ge at LNGS*. Nucl. Phys. B (Proc. Suppl.) 145 (2005) 242.
- [53] M. Pedretti et al. *Cuore Experiment: The search for neutrinoless double beta decay*. Int. J. Mod. Phys. A23 (2008) 3395.
- [54] D. Akimov et al. *EXO: an advanced Enriched Xenon double-beta decay Observatory*. Nucl. Phys. B (Proc. Suppl.) 138 (2005) 224.
- [55] D. G. et al. Phillips. *The Majorana experiment: an ultra-low background search for neutrinoless double-beta decay*. arXiv:1111.5578.
- [56] C. Weinheimer. *Laboratory Limits on Neutrino Mass*. G. Altarelli and K. Winters (Eds.), Neutrino Mass, Springer 2003.
- [57] F. Gatti et al. *MARE Microcalorimeter Arrays for a Rhenium Experiment*. <http://mare.dfm.uninsubria.it>, 2006.
- [58] M. Sisti et al. *New limits from the Milano neutrino mass experiment with thermal microcalorimeters*. Nucl. Instr. and Meth. in Phys. A520 (2004) 125.
- [59] C. Kraus et al. *Final results from phase II of the Mainz neutrino mass search in tritium β decay*. Eur. Phys. J. C40 (2005) 447.
- [60] D. A. Robertson, R.G.H. Knapp. Ann. Rev. Nucl. Part.Sci. 38 (1988) 185.
- [61] G. Beamson H Q Porter und D W Turner. *The collimating and magnifying properties of a superconducting field photoelectron spectrometer*. J. Phys. E: Sci. Instrum., Vol. 13, 1980.

- [62] John David Jackson. Dt. Übers. Kurt Müller. Bearb. Christopher Witte. *Klassische Elektrodynamik*. Berlin [u.a.] : de Gruyter, 2006.
- [63] Susanne Mertens. *Study of Background Processes in the Electrostatic Spectrometers of the KATRIN Experiment*. PHD Thesis, KIT.
- [64] S. Fischer et al. *Monitoring of Tritium Purity During Long-Term Circulation in the KATRIN Test Experiment LOOPINO Using Laser Raman Spectroscopy*. Fusion Science and Technology Vol. 60(3) pp. 925-930 Oct. 2011.
- [65] Markus Hötzel. *Simulation and Analysis of Source Related Effects for KATRIN*. PHD thesis, KIT.
- [66] M. Babutzka et al. *Monitoring of the operating parameters of the KATRIN Windowless Gaseous Tritium Source*. 2012 New J. Phys. 14 103046 doi:10.1088/1367-2630/14/10/103046.
- [67] S. Grohmann. *Stability analyses of the beam tube cooling system in the KATRIN source cryostat*. <http://dx.doi.org/10.1016/j.cryogenics.2009.06.001>, 2009.
- [68] H. Schoen S. Grohmann, T. Bode und M. Suesser. *Precise temperature measurement at 30 K in the KATRIN source cryostat*. Cryogenics, vol. 51, no. 8, pp. 438-445, 2011.
- [69] A. Poon et al. *Rear Section Design Document - Outline of Questions*. Proposal, http://fuzzy.fzk.de/bscw/bscw.cgi/d479671/RearSectionDesignQuestions_v1.pdf, 2008.
- [70] A. Windberger. *Berechnungen und Simulationen zum Verhalten von Ionen in der differenziellen Pumpstrecke des KATRIN-Experiments*. Diploma thesis, KIT 2010.
- [71] S. Lukic S. Nagy S. Stahl M. Ubieto-Díaz, D. Rodríguez und K. Blaum. *A broadband FT-ICR Penning trap system for KATRIN*. International Journal of Mass Spectrometry, vol. 288, no. 1-3, pp. 1-5, 2009.
- [72] J. Kaspar et al. *Effect of energy scale imperfections on results of neutrino mass measurements from β -decay*. Nucl. Instr. and Meth. A 527 (2004) 423.
- [73] T. Thümmler. *Präzisionsüberwachung und Kalibration der Hochspannung für das KATRIN-Experiment*. Doktorarbeit, Universität Münster.
- [74] A. Osipowicz F. Glück. *Air coil design at main spectrometer*. Talk at the 14th KATRIN Collaboration Meeting, fuzzy.fzk.de/bscw/bscw.cgi/d443733/95-TRP-4440-D1-FGlueck-AOsipowicz.ppt.
- [75] F. Glueck et al. *Design Document Air Coil System and Magnetic Field Sensor System Version 1*. <http://fuzzy.fzk.de/bscw/bscw.cgi/d530439/Air%20Coil%20System%20and%20Magnetic%20Field%20Sensor%20System.pdf>.

- [76] Jan Reich. *Magnetfeldmessungen und Designarbeiten für das EMCS Luftspulensystem am KATRIN Hauptspektrometer*. Diploma Thesis, Universität Karlsruhe.
- [77] Jan Hergenhan. *Das KATRIN Luftspulensystem: Messungen des Feldverlaufs und Überwachung mit einem Sensorsystem*. Diploma Thesis, KIT.
- [78] J.E. Everett und J.E. Osameikhian. *Spherical coils for uniform magnetic fields*. J.Sci. Instrum., 43, 470 (1966).
- [79] J.W. Clark. *A New Method for Obtaining a Uniform Magnetic Field*. Rev. Sci. Instrum., 9, 320 (1938).
- [80] M. Juretzko. *Kurzbericht Magnetometereinmessung*. Personal Communication.
- [81] Delta Elektronika. *Stromversorgung SM 3000 - Serie*. technical manual.
- [82] Wolfgang Käfer. *Investigation of the KATRIN sensitivity*. PHD thesis, KIT.
- [83] Pascal Renschler. *KESS - A new Monte Carlo simulation code for low-energy electron interactions in silicon detectors*. PHD thesis, KIT.
- [84] F. Glück. *C-programs for electromagnetic design*. <https://fuzzy.fzk.de/bscw/bscw.cgi/34401>.
- [85] Benjamin Leiber. *Non-axially symmetric field and trajectory calculations for the KATRIN-experiment*. Diploma thesis, KIT.
- [86] *Tools for Electromagnetic Field Simulation in the KATRIN Experiment*. Master of Science thesis by Thomas Joseph Corona, Massachusetts Institute of Technology, Feb 2009.
- [87] W. T. Vetterling W. H. Press, S. A. Teukolsky und B. P. Flannery. *Numerical Recipes*. 3rd ed. Cambridge University Press.
- [88] F. Glück. *AXISYMMETRIC MAGNETIC FIELD CALCULATION WITH ZONAL HARMONIC EXPANSION*. PIER B vol. 32 (2011), pp. 351.
- [89] F. Glück. *Steel in the KATRIN buildings and the magnetic field in the main spectrometer*. internal report.
- [90] F. Floether. *Magnetic Dipole Models of the Magnetic Materials Field inside the KATRIN Spectrometers - Part III Long Vacation Project*. fuzzy.fzk.de/bscw/bscw.cgi/d666171/Magnetic%20Dipole%20Models.doc.
- [91] *Geomagnetic Observatory Online Archive*. <ftp://ftp.nmh.ac.uk/>.
- [92] F. Glueck. *Background theory: electron motion from spectrometer electrodes to the detector*. Internal KATRIN report, BSCW: http://fuzzy.fzk.de/bscw/bscw.cgi/d174403/background_theory_Glueck.pdf.
- [93] A. Unru B. Zipfel A. Osipowicz, U. Rausch. *A scheme for the determination of the magnetic field in the KATRIN main spectrometer*. arXiv:1209.5184.

-
- [94] J. Letnev P. Marte A. Müller A. Spengler A. Unru A. Osipowicz, W. Seller. *A mobile Magnetic Sensor Unit for the KATRIN Main Spectrometer*. 2012 JINST 7 T06002, arXiv:1207.3926.
- [95] Marco Antoni. Ongoing diploma thesis, KIT.
- [96] Bartington Instruments. Operation Manual for Mag-03 Three-Axis Magnetic Field Sensors.
- [97] VTI Technologies. *SCA121T Dual Axis Inclinator Modules*. Data Sheet.

Acknowledgements

Finally I would like to thank all those who supported me during the process of creating this thesis. Special thanks I would like to give to

- Prof. Guido Drexlin for giving me the opportunity of working at this project for the KATRIN experiment and his support during my time at the KIT.
- Prof. Thomas Müller for agreeing to be the second reviewer of this thesis.
- Dr Ferenc Glück for his very helpful input and advice throughout my time at KATRIN and for creating the foundations of the KATRIN emd calculations.
- All my colleagues at the IKP for helpful discussions in technical and physical topics. Special thanks here go to Nancy Wandkowsky, Stefan Groh and Benjamin Leiber.
- The engineering and technical staff at IKP for their support in hardware works and measurements inside the main spectrometer. I would explicitly like to thank Klaus Mehret and Holger Frenzel for their great help and patience.
- For the technical support during planning and construction of the magnetic monitoring system I would like to thank Dr Sascha Wüstling and Armen Beglarian from the IPE and Holger Krause from the IKP.
- My diploma students Jan Hergenhan and Marco Antoni for their great supporting work.
- For proofreading this thesis I would like to thank Ferenc Glück, Stefan Groh and Nancy Wandkowsky.
- The PhD and diploma students at IKP for the great work atmosphere.
- Stefan Görhardt for always being concerned cheering me up.
- Markus Hötzel for his patient advice on the PhD application process.
- Also I would like to thank all other people who helped me make it through my time as a PhD student even if they are not named here.